Investigating the Role of Iron Sulfide on the Long-Term Stability of Reduced Uranium under Oxic Groundwater Conditions

by

Yuqiang Bi

A dissertation submitted in partial fulfillment
of the requirements for the degree of
Doctor of Philosophy
(Environmental Engineering)
in the University of Michigan
2014

Doctoral Committee:

Professor Kim F. Hayes, Chair
Professor Udo Becker
Professor Jim Davis, Lawrence Berkeley National Laboratory
Professor Avery Demond
Assistant Professor Brian R. Ellis

This dissertation is dedicated to my grandparents,

毕邵学 和 庄淑芳

Without whose love and inspiration I would not have gotten here.

Acknowledgments

I would like to thank my advisor, Prof. Kim Hayes for his support and invaluable advice throughout my Ph.D. career. I have learned a lot from him, by his example, much about scientific curiosity and discipline. He has always been willing to discuss experimental results and provide ideas to test my theories. I would also like to thank my dissertation committee members: Drs. Avery Demond, Udo Becker, Jim Davis, and Brian Ellis for their perspectives, suggestions, and critical comments.

Many people have helped me pull together this dissertation and I would like to extend my heartfelt gratitude for their generosity. Dr. Owen Duckworth at NC State University encouraged me to pursue my Ph.D. at Michigan and remains a great role model for me. At Michigan, Dr. Sung Pil Hyun guided me through XAS data collection and analysis. Julian Carpenter and his talent in mechanical design and fabrication made the lab operation efficient and fun. Thomas Yavaraski offered the best support on instrumental analysis with his patience, skill, and talent. The summer undergraduate researcher, Victor Lê, contributed to sample collection and data analysis in the flow-through study. In the final weeks of this research, Sandra Fernando helped me with XPS data interpretation; Junnan Zhao assisted me with TEM images acquisition.

Thanks to my fellow students Tara Clancy, Xunchang Fei, Qiang Dai, Derya Ayral, Sherri Cook, Nadine Katlaz, and Antone Jain for lots of support and encouragement. Special thanks to our wonderful staff of CEE: Rick Burch for parts fabrication, Nancy Osugi for financial support, Jessica Taylor for graduate advisory, and Angela Jeon for student service.

This dissertation research is not possible without the funding from the U.S. DOE through grant # DE-FG02-09ER64803. Many thanks to the Rackham graduate school for the financial opportunities along the years to support travelling and research. I am also grateful for the funding support from several GSI appointments which have provided me with great teaching experiences.

Finally, I express my deepest gratitude to my parents for raising me and educate me, although far and away. They act as my financial safety net, and always provide an emotional support and inspiration. Most importantly, I would like to express my love to Yuan, my best friend and loudest cheerleader on my way to the doctorate, who always believes in me and helps me through difficult times.

Table of Contents

List of Tables

List of Figures

List of Appendices

List of Abbreviations

CMBR – Completely mixed batch reactor

CSTR – Continuously stirred tank reactor

EDS – Energy dispersive X-ray analysis

EPA – Environmental protection agency

EXAFS – Extended X-ray absorption fine structure spectroscopy

ICP-MS – Inductively coupled plasma-mass spectrometry

NABIR – Natural and Accelerated Bioremediation Research

NEA – Nuclear Energy Agency

PNNL – Pacific Northwest National Laboratory

SSRL – Stanford Synchrotron Radiation Lightsource

SEM – Scanning electron microscopy

SRB – Sulfate reducing bacteria

TEM – Transmission electron microscopy

XANES – X-ray absorption near-edge structure spectroscopy

XAS – X-ray absorption spectroscopy

XPS – X-ray photoelectron spectroscopy

XRD – X-ray diffraction

Abstract

The historical accumulation and improper disposal of radioactive waste from extensive extraction and processing activities have caused widespread uranium contamination of groundwater and soils in the United States. Because uranium is a toxic heavy metal and radiological hazard, its migration poses serious human health and ecological risk. While successful remediation has been practiced at selected uranium contaminated sites, recent concerns have been raised over maintaining the long-term immobilization of reduced uranium solids in the subsurface when oxidants re-enters the reducing zones. Previous studies reported that iron sulfide minerals formed during bioreduction may retard UO_2 reoxidation by consuming dissolved oxygen, yet limited mechanistic information is available detailing the thermodynamic and kinetic constraints that control UO_2 oxidative dissolution in the presence of iron sulfide in groundwater.

This research aims at understanding the abiotic role of iron sulfide in affecting the stability of uraninite ($UO_{2(s)}$) under oxic groundwater conditions. Synthetic nano-particulate mackinawite (FeS) and uraninite solids were prepared to simulate reduced precipitates in groundwater systems dominated by sulfate reducing conditions. Completely mixed batch and flow-through reactor experiments were conducted to investigate UO_2 oxidative dissolution rate in artificial groundwater as a function of pH, FeS content, and carbonate and oxygen concentrations. FeS and UO_2 oxidation products were characterized by X-ray diffraction (XRD), X-ray absorption spectroscopy (XAS), X-ray photoelectron spectroscopy (XPS), and transmission electron microscopy (TEM) to examine reaction pathways and rate-controlling

mechanisms during oxidation. FeS reaction products, i.e., Fe(III) hydroxides, aqueous Fe(II), and elemental sulfur, were also isolated and examined for their influence on UO_2 oxidation.

This research demonstrates that FeS serves as an effective oxygen scavenger and inhibits UO_2 oxidative dissolution by keeping dissolved oxygen (DO) levels low. The dissolution rate of UO_2 in the presence of FeS is over one order of magnitude lower than those in the absence of FeS under otherwise comparable oxic conditions. The preferential reaction of FeS with oxygen leads to surface-oxidation limited dissolution of UO_2, which is facilitated by a fast detachment of ternary Ca-U(VI)-CO_3 complexes. When FeS content significantly diminishes, increasing DO concentration may passivate UO_2 surface by forming a less reactive U(VI) layer. However, dissolved calcium and carbonate species can limit the formation of passivation layer and enhance the overall UO_2 dissolution rate by promoting U(VI) detachment rate from surface. When groundwater composition exceeds the solubility of uranyl minerals, a secondary phase may be generated to further limit the dissolution rate of UO_2 after FeS depletion.

By focusing on the mineral-water interfacial reactions, this dissertation has developed mechanistic models for illustrating uranium transformation during anoxic-oxic transitions in the presence of iron sulfide. The results of this research contribute to the understanding of uranium fate and transport during periods of persistent oxygen intrusion in heterogeneous groundwater systems.

Chapter 1

Introduction

1.1 Motivation

Since the 20th century, the concerted effort to discover and exploit uranium (U) resources for the development and production of nuclear weaponry and nuclear energy has contributed to massive uranium mining activities (Abdelouas, 2006). Historically, abandoned waste accumulation and improper disposal of the radioactive materials from intensive uranium mining and milling have resulted in contamination to the local environment (Gavrilescu et al., 2009). Available research on DOE uranium research and production facilities indicates elevated uranium concentrations in subsurface environments and the migration of uranium to surrounding areas (Riley et al., 1992). Over 6.4×10^{9} m^3 of contaminated groundwater and 40×10^{6} m^3 of contaminated soils in the US alone requires more than $15 billion (in 1998 dollars) to clean up (DOE, 1997; DOE, 1998; National Research, 1999). The contamination of groundwater by uranium poses a direct threat to water supplies, while soil contamination poses an equally important threat on land use, food supply, and water quality.

Uranium in drinking water is covered under the Safe Drinking Water Act. The EPA established the maximum contaminant level (MCL) for uranium of 30 $\mu g\cdot L^{-1}$ in drinking water (EPA, 2000). California has already adopted an MCL of 20 $pCi\cdot L^{-1}$ (~25 $\mu g\cdot L^{-1}$) based

on renal toxicity (OEHHA, 2001). Despite the huge cost and regulatory effort, the progress on groundwater and soil remediation has been slow, partly attributed to the technical limitations and poor understanding of the geochemical setting of the contaminated sites as well as the reaction kinetics and equilibrium.

The environmental risks associated with U contamination are strongly governed by redox conditions and solid-phase U solubility. Uranium (VI) is the dominant oxidation state under oxic conditions. This form is soluble and forms stable complexes with carbonate and calcium in groundwater (Guillaumont et al., 2003; Dong and Brooks, 2006; Stewart et al., 2010). Conversely, the reduction of U(VI) under anaerobic conditions leads to the formation of sparingly soluble U(IV) solid phases, such as uraninite (UO_2), thus limiting dissolved U concentration and U mobility. Popular bioremediation strategies utilize respiratory microorganisms to immobilize U in the subsurface by enzymatically reducing U as the terminal electron acceptor (Lovley et al., 1991; Lovley and Phillips, 1992). The reduction of U can also occur abiotically by reduced species, such as surface adsorbed Fe(II) (Liger et al., 1999) and sulfide minerals (Wersin et al., 1994; Hua et al., 2006). Recent studies further suggest that monomeric U(IV) species may form during microbial U(VI) reduction in association with phosphate or carbonate as sorbed complexes on soils and sediments (Bernier-Latmani et al., 2010; Fletcher et al., 2010; Boyanov et al., 2011), before converting to more stable U(IV) precipitates. However, the biostimulation strategy is not trouble free, with concerns raised over the long-term stability of bioreduced and immobilized uranium. The nanometer-sized uraninite produced during active bioreduction may be susceptible to reoxidation by various environmental agents such as oxygen (Zhou and Gu, 2005; Moon et al., 2007; Komlos et al., 2008; Moon et al., 2009), nitrate (Finneran et al., 2002; Senko et al.,

2002), Fe(III) (hydr)oxides (Sani et al., 2005; Wan et al., 2005; Ginder-Vogel et al., 2010), and manganese oxide (Fredrickson et al., 2002; Wang et al., 2013). For example, dissolved oxygen (DO) is one of the strongest and most abundant oxidants of U(IV), and has been shown to oxidize UO_2 within several hours to days in batch or sediment column experiments (Casas et al., 1994; Moon et al., 2007).

The long-term stability of reduced U(IV) solids may be achieved when dissolution and/or reoxidation of UO_2 are sufficiently slow in the subsurface. Maintaining the reducing conditions can be crucial to minimizing UO_2 dissolution rates and limiting U mobility during occasional or low levels of oxidant intrusion. Naturally occurring aqueous sulfide and sulfide minerals formed under sulfate reducing conditions (SRCs) may serve as electron sources for maintaining reducing conditions and continued U immobilization (Wersin et al., 1994; Suzuki et al., 2005; Hua et al., 2006). Past field studies have attributed the resistance of U(IV) phases to oxidative dissolution to the presence of sulfide minerals, despite seasonal exposure to air in natural near-surface sediments (Suzuki et al., 2005; Qafoku et al., 2009).

Under low temperature SRCs, a variety of iron sulfide minerals may form, including mackinawite (FeS), greigite (Fe_3S_4), or pyrite (FeS_2) (Rickard, 1969b; Rickard and Morse, 2005). In general, mackinawite is thought to be the first crystalline phase to form and most common iron sulfide in anoxic sediments (Rickard, 1995). Being thermodynamically unstable, mackinawite ultimately transforms into more stable phases, such as greigite and pyrite under suboxic conditions (Berner, 1981). Under reducing conditions, however, mackinawite may persist for significantly long periods of time (Abdelouas et al., 2000; Benning et al., 2000).

Mackinawite has attracted recent interest for contaminant attenuation due to its reactivity in the reductive transformation of pollutants (Elsner et al., 2004) and its retention of heavy metals via sorption and isomorphous substitution (Coles et al., 2000). Previous studies have demonstrated the impact of mackinawite in arsenic (Jeong et al., 2010a; Han et al., 2011) and mercury (Jeong et al., 2010b) immobilization, and in the degradation of organic pollutants (Butler and Hayes, 2001; Hyun and Hayes, 2009). Recent research further recognized mackinawite as an important component in radionuclide remediation systems (Abdelouas et al., 1999a). Laboratory studies have demonstrated that mackinawite (FeS) produced by sulfate reducing bacteria (SRB) can retard UO_2 reoxidation and possibly provide long-term protection against oxygen intrusion (Abdelouas et al., 1998; Abdelouas et al., 1999a; Moon et al., 2009). The abiotic reduction of U(VI) by mackinawite surfaces with the production of U(IV) solid phases has also been observed (Hua and Deng, 2008; Hyun et al., 2012). Given the intimate association of mackinawite with U(IV) in bioreduced systems (Bargar et al., 2013), a reliable and comprehensive assessment of long-term stability of U should include the interactions of UO_2 with iron sulfides under redox sensitive conditions. If mackinawite can effectively scavenge oxidants and counter the redox change while being readily generated by SRB, the success of U remediation for long-term stability may be possible, without the need for continuous chemical input and the associated energy requirements for maintaining an active system. In this dissertation, mackinawite is of major interest in its role of affecting the stability of reduced uranium under oxic groundwater conditions.

While scavenging oxidants such oxygen, mackinawite undergoes oxidation-induced transformation, generating dissolved Fe(II) and various Fe(III) solid phases and sulfur

products, depending on geochemical conditions (Burton et al., 2009; Chirita, 2009; Jeong et al., 2010a; Bi et al., 2013). The exhaustion of mackinawite in an event of drastic oxidant intrusion can result in exposure of reduced U(IV) solids to various oxidants which are capable of remobilizing U. Even before mackinawite is completely depleted, the co-existence of mackinawite and its oxidation products may have implications for uranium stabilization. The oxidation products may interact with the uranium for as long as oxic condition persists and the oxidation reaction of mackinawite produces them. Therefore, the impact of FeS oxidation products on the fate and transport of U should be carefully investigated for better assessing the role of sulfide minerals in post-biostimulation scenarios.

Evaluating the role of mackinawite on the long-term stability of reduced uranium presents challenges, requiring an examination of an assortment of redox reactions in a heterogeneous system at a molecular level, which are clearly under documented in the current literature. In addition, there is also an underlying complexity stemming from the diverse geochemical conditions (e.g., pH, pCO_2, and pCa) found at U-contaminated sites, which influence chemical speciation and reaction pathways. Addressing these knowledge gaps requires further investigation of the reaction mechanisms as well as associated thermodynamic and kinetic constraints. By focusing this dissertation on redox processes occurring at solution-mineral interfaces, it is possible to identify key abiotic steps of oxidative mobilization processes controlling uranium retention in the subsurface where iron sulfide is produced and consumed during oscillation of redox conditions.

1.2 Research Scope and Objectives

The main objectives of the research presented in this dissertation are:

1. To identify and quantify dominant geochemical mechanisms that inhibit reduced uranium from oxidative mobilization in the presence of mackinawite under oxic conditions;
2. To determine the influence of a range of groundwater conditions on the ability of mackinawite to inhibit reoxidation and remobilization of reduced uranium;
3. To examine the impact of post oxidation products of mackinawite on reduced uranium stability and mobility.

The central hypotheses of this work are (1) nanocrystalline mackinawite mineral scavenges dissolved oxygen in groundwater to inhibit the oxidative dissolution of uraninite; (2) the oxidation processes of mackinawite are controlled by geochemical conditions that also affect the dissolution rate of uraninite; and (3) oxidation products of mackinawite also influence uraninite oxidation when oxic condition prevails.

The motivation and objectives of the study are described in this chapter (Introduction), followed by Chapter 2 (Background), which includes a synopsis of research and discusses the complexity of uranium speciation and transformation, and the behavior of mackinawite in the environment. Chapter 3 (Materials and Methods) provides the general experimental protocols used in this dissertation and the preparation methods of synthetic mackinawite, uraninite, and ferrihydrite particles. Chapters 4, 5, and 6 seek to quantify the impact of mackinawite on the stability and lability of reduced uranium solid phases under oxic groundwater conditions. Chapter 4 first identifies the dominant redox reactions and major oxidation products of UO_2 in the absence and presence of FeS at pH 7 in a continuously mixed batch reactor, and

proposes a mechanistic model for inhibited oxidative dissolution of UO_2 by FeS. Chapter 5 elucidates the kinetics of UO_2 oxidative dissolution in the presence of FeS using CSTRs at various geochemical conditions, including pH, DO concentration, and FeS content. Chapter 6 explores the impact of FeS oxidation products in promoting UO_2 dissolution during the suboxic-oxic transition. Finally, Chapter 7 (Conclusions and Future Work) provides a summary of the major findings, contributions, and recommendations for future work.

Chapter 3 – Materials and Methods

Synthetic mackinawite and uraninite were selected as the model compounds in this dissertation for examining the role of iron sulfide in controlling uranium oxidation under oxic conditions. Chapter 3 introduces experimental methods for preparing these nanocrystalline materials as well as reactor systems for studying the reaction mechanisms and kinetics. The characterization of synthetic FeS and UO_2 are also presented in this chapter to provide a basis for understanding the oxidation reactions that are reported in the following chapters. The chemical and physical properties of abiotic FeS and UO_2 with respect to mineralogy, crystallography, particle size, and surface area are provided at the end of this chapter.

Chapter 4 – Oxidative dissolution of UO_2 in a simulated groundwater containing synthetic nanocrystalline mackinawite

Although recent studies show that FeS produced in the subsurface by biostimulation of SRB can retard UO_2 oxidation, the abiotic mechanism of U(IV) oxidation is not well understood and is often difficult to isolate in field studies or column studies where microorganisms are active and biogenic oxidation processes may be occurring

simultaneously. In Chapter 4, the oxidative dissolution of synthetic UO_2 by dissolved oxygen was examined in absence and presence of FeS under abiotic simulated groundwater conditions. The solid and solution phase reaction products were characterized by microscopic and spectroscopic techniques. FeS inhibited UO_2 dissolution by effectively scavenging oxygen and keeping DO levels low. During the inhibition period, oxidation of structural Fe(II) and S(-II) of FeS were found to control the DO levels, leading to the formation of iron oxyhydroxides and elemental sulfur, respectively, as verified by X-ray diffraction (XRD), Mössbauer, and X-ray absorption spectroscopy (XAS). After FeS depletion, UO_2 oxidative dissolution occurred at a higher rate than in the control experiment where FeS was absent, presumably a result of higher DO concentration. XAS analysis confirmed that soluble U(VI)-carbonato complexes were adsorbed by iron hydroxides (i.e., nanogoethite and lepidocrocite) formed from FeS oxidation, which provided a mechanism for U(VI) retention.

Chapter 5 – Nano-FeS impedes UO_2 dissolution rate under varied oxic conditions

Long-term stability of reduced U(IV) solids may be achieved when dissolution and/or reoxidation of UO_2 are sufficiently slow during occasional or low levels of oxidant intrusion. Although effective oxygen scavenging by FeS has been shown to slow UO_2 oxidation, the kinetics of U(IV) dissolution in FeS-containing systems remain poorly understood. In Chapter 5, the impact of FeS on rate of UO_2 oxidative dissolution in artificial oxic groundwater was examined using continuously stirred tank reactors (CSTRs). The dissolution kinetics of UO_2 dissolution was examined in the presence and absence of FeS under various pH, DO and FeS concentrations. With spectroscopic characterization of solid phase reaction products, a conceptual mechanistic reaction model was developed for

inhibited oxidative dissolution of UO_2 by FeS. The UO_2 dissolution rates in the presence of FeS are over one order of magnitude lower than those in the absence of FeS under otherwise comparable oxic conditions due to effective scavenging of DO by FeS. Although the removal of DO was significant in the presence of sufficient FeS, low DO concentration remained during the inhibition period, resulting in a rate-limiting step of surface-oxidation. The duration for inhibiting UO_2 from rapid reoxidation, and maintaining an oxygen-limited rate control, was found to be directly governed by the amount of FeS in the system.

Chapter 6 – Surface passivation limited UO_2 oxidative dissolution upon FeS depletion

Once iron sulfides are depleted from subsurface, the stability of reduced uranium may be limited during the oxidative stage of redox cycles. When oxidized, remobilized U(VI) in the groundwater can again pose human/ecosystem health risks. The iron oxidation products of FeS, such as goethite and lepidocrocite, may also impact dissolution processes of UO_2 as potential oxidants. In Chapter 6, the kinetics of UO_2 oxidative dissolution by DO was investigated after oxygen breakthrough in CSTR systems. FeS and its reaction products, i.e., Fe(III) oxides and aqueous Fe(II), were carefully examined for their influence on UO_2 dissolution during the anoxic-oxic transition. The dynamics of UO_2 surface reactions were investigated using XAS, transmission electron microscopy (TEM), and X-ray photoelectron spectroscopy (XPS). At low FeS concentration, until DO breakthrough, the UO_2 surfaces remained reduced without passivation at pH = 7. The clean U(IV) surface then was rapidly oxidized by DO upon breakthrough through a rate-limiting surface detachment of $Ca\text{-}CO_3\text{-}UO_2$ complexes. In comparison, passivation layers develop at pH 6 and pH 8 as a result of diminishing FeS reducing capacity, which contribute to slower dissolution rate relative to pH

= 7 after oxygen breakthrough. This chapter illustrates the importance of passivation layer that forms at different pH with low concentration of FeS in controlling the relative uranium dissolution rate at anoxic-oxic transition.

Chapter 7 - Conclusions and recommendations

The final chapter in this dissertation summarizes the research presented in Chapters 4-6. This dissertation examines the potential of FeS to inhibit the reoxidation of solid phase U(IV) by identifying the reaction mechanisms with the aid of modern microscopic and spectroscopic characterization tools. These findings increase our understanding of the role of iron sulfides in U redox transformations and offer insights to enhance reduced U stability against reoxidation and remobilization at sites which have undergone biostimulation under sulfate reducing conditions.

Chapter 2

Background

Uranium reduction by reduced iron minerals is considered an important abiotic pathway for uranium immobilization under iron or sulfate reducing conditions. By reducing soluble U(VI) species to highly insoluble U(IV) solid phases like UO_2(s), U may remain immobilized in the solid form as long as reducing conditions prevail. Under sulfate reducing conditions, reduced iron sulfide phases will form if iron is present. If present in significant quantities, these iron sulfides may provide enough buffering against U(IV) re-oxidation when periodic oxic conditions return. To date, limited mechanistic information is available detailing the role of iron sulfide minerals as oxidant scavengers in prolonging reduced U(IV) stability during anoxic-oxic transition. This chapter provides a literature review on iron sulfide and uranium aqueous chemistry, uranium groundwater contamination and bioremediation strategies, the interactions of reduced uranium with iron sulfides, adsorption of uranium by iron minerals, and the oxidation and reduction processes controlling U mobility in groundwater. The chapter concludes with a summary of knowledge gaps and research hypotheses that are investigated in the following chapters. The intention of this chapter is to offer a synopsis of the state of knowledge to date, which provides a general background for establishing the context of this dissertation research.

2.1 Formation of Iron Sulfides

Iron sulfide minerals are common in anoxic sediments and saline environments. They primarily result from the microbial activities of sulfate-reducing bacteria (SRB), which can generate millimolar levels of aqueous sulfide as a metabolic by-product by utilizing sulfate as a terminal electron acceptor (Goldhaber and Kaplan, 1974). When aqueous sulfide reacts with aqueous Fe(II) and amorphous Fe solids, iron sulfide minerals can readily form (Berner, 1970; Canfield and Berner, 1987; Canfield, 1989). Since Issatchenko (1912) first reported bacterially generated iron sulfides within the cells of SRB, many follow-on studies have shown SRB are commonly associated with iron sulfides (Rickard, 1969b; Lovley et al., 1993). Although iron concentration usually is not a limiting factor in the formation of iron sulfides in many natural systems, Fe(III) reduction to soluble Fe(II) by iron reducing bacteria and archaea may be needed to facilitate the process in suboxic and anoxic environments. Typical sources of iron are condensed phases, including Fe(III) oxyhydroxides (ferrihydrite, goethite, lepidocrocite) and Fe oxides (hematite, magnetite). The production of iron sulfides, therefore, should be regarded as arising from a complex microbial community undergoing iron or sulfate reduction in close proximity.

Depending on biogeochemical conditions, a variety of iron sulfide minerals may form such as mackinawite ($FeS_{0.9}$; hereafter referred as FeS), greigite (Fe_3S_4), pyrrhotite ($Fe_{1-x}S$), or pyrite (FeS_2). Amorphous FeS is often thought to be the initial precipitate formed in anoxic sedimentary environments (Berner, 1967), which crystallizes to the more stable mackinawite within days (Rickard, 1995; Wilkin and Barnes, 1996). Due to thermodynamic instability, mackinawite is sensitive to oxidation and can transform into more stable phases, such as greigite and pyrite under suboxic conditions at low temperatures (Berner, 1981). In

some anoxic sediments, metastable mackinawite and greigite may comprise the major faction of acid-volatile sulfides (AVS) (Rickard and Morse, 2005). Both minerals may exist for geologically significant time periods (Abdelouas et al., 2000; Benning et al., 2000), even though the mechanism is incompletely understood. Canfield et al. (1998) implies that the local microbial ecology has a critical effect on the persistence of metastable minerals, such as mackinawite.

In the laboratory, three synthesis methods have been commonly used to produce mackinawite model compounds for the investigation of chemical properties and reactivity. By reacting aqueous sulfide with either (1) metallic iron (Berner, 1964) or (2) ferrous iron solution (Rickard, 1969a; Butler and Hayes, 1998), black mackinawite readily precipitates in the solution. Biogenic mackinawite can be produced by (3) SRB, such as *Desulfovibrio vulgaris,* which respire sulfate and gain energy from organic and inorganic electron donors (Herbert et al., 1998). While crystalline mackinawite is usually generated by sulfide reacting with metallic iron (Lennie and Vaughan, 1996), poorly crystalline phases are typically observed using the other two methods (Herbert et al., 1998; Jeong et al., 2008). The amorphous mackinawite produced in the laboratory has been found to be similar to its natural counterpart in lake sediments (Spadini et al., 2003).

2.2 Properties of Mackinawite

Belonging to *P4/nmm* space group, mackinawite has a tetragonal layered structure. Each Fe atom is coordinated by four sulfur atoms, resulting in layers of edge-sharing tetrahedrons (Figure 2.1). Likely due to the short Fe-Fe distance (0.26 nm) within mackinawite layers, Fe *d*-orbital may be delocalized extensively in the basal plane, giving

rise to its metallic conducting property (Vaughan and Ridout, 1971). As a result, the delocalized *d* electrons in the conduction band contribute to the effectiveness of FeS-mediated reductive transformation of contaminants found in many natural and engineered systems.

Mackinawite is often present in disordered or nano-sized forms which are characterized by small particle size and large surface area (Wolthers et al., 2003). The reported particle size of nanocrystalline mackinawite ranges from 3 ~ 75 nm in diagonal length and 2 ~ 15 nm in thickness (Ohfuji and Rickard, 2006; Jeong et al., 2008). The large variation in measured particles sizes may result from the different preparation methods and the inherent limit in the analytical techniques. For example, particle aggregation inevitably occurs during the drying of mackinawite suspension when preparing TEM specimen, causing overestimation of the particle size (Jeong et al., 2008). Therefore, the specific surface area (SSA) can vary by over two orders of magnitude, from 10 to 380 $m^2 \cdot g^{-1}$ (Ohfuji and Rickard, 2006). As an alternative method, crystallite size derived from X-ray powder diffraction (XRPD) and Scherrer equation may be used for estimating SSA of mackinawite particles. Jeong et al (2008) reported a SSA of ~220 $m^2 \cdot g^{-1}$ for a synthetic nanocrystalline mackinawite, which was prepared using the same method as in this dissertation.

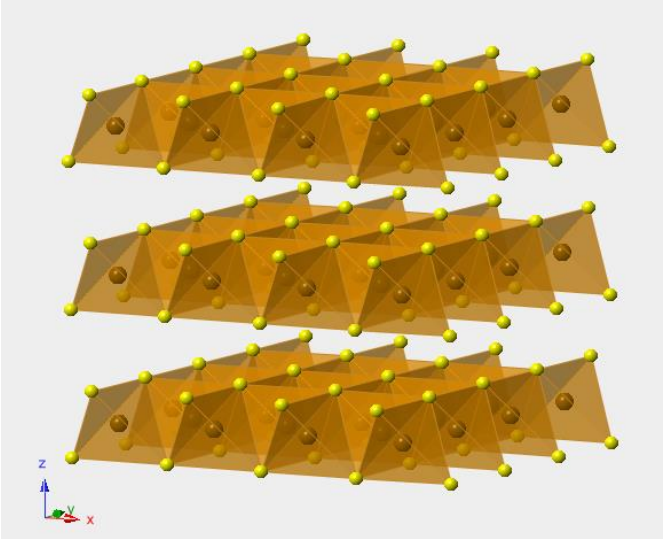

Figure 2.1 Schematic diagram of mackinawite structure viewed from above the (001) plane, (generated by CrystalMaker®). The distance between layers along 001 direction is ~0.5 nm. Brown: iron atoms; yellow: sulfur atoms.

The reactive sites on the surfaces of nanocrystalline mackinawite determine the surface charge in aqueous solution. Hydrated FeS surface consists of hydroxyl and sulfhydryl functional groups as a result of hydrolysis of the partially coordinated surface iron and sulfur atoms on the edges of FeS crystals. Depending on solution pH, both functional groups exist in either protonated or deprotonated forms: $\equiv FeOH_2^+$ and $\equiv FeSH^0$ below pH_{pzc}; $\equiv FeOH^0$ and $\equiv FeS^-$ above pH_{pzc} (the pH of zero surface charge). Wolthers et al. (2005) proposed two reactive sulfur sites as mono-coordinated ($\equiv FeSH^0$) and tri-coordinated ($\equiv Fe_3SH^0$) on FeS surface, which comprise a total site density of 4 sites·nm^{-2}. While the pH_{pzc} of crystalline FeS was previously determined to be 2.9 by potentiometric titration (Widler and Seward, 2002), a more recent study on nanocrystalline FeS yielded a pH_{pzc} of ~7.5 (Wolthers et al., 2005). Apparently the small particle size of nano-FeS causes significant changes in surface properties from its crystalline counterpart, which may further influence surface-mediated reactions in the environment.

2.3 Mackinawite as a Reductant and Sequestration Agent

Mackinawite has attracted interest in contaminant attenuation due to its reactivity toward reductive transforming of pollutants (Elsner et al., 2004) and its retention of heavy metals via adsorption and isomorphous substitution (e.g., Pb and Cd) (Coles et al., 2000). Recent work demonstrated the influence of mackinawite in the immobilization of arsenic (Jeong et al., 2010a; Han et al., 2011) and mercury (Jeong et al., 2010b) and the degradation of chlorinated organic pollutants (Butler and Hayes, 2001; Hyun and Hayes, 2009). Mackinawite is also recognized as an important ingredient and source of sulfide in many toxic metal and radionuclide remediation systems including uranium-contaminated sites (Abdelouas et al., 1999a; Coles et al., 2000).

Suzuki et al. (2005) attributed the stability of U(IV) to the presence of organic matter and sulfide minerals in the field despite seasonal exposure to air in natural near-surface sediments. In several studies, Abdelouas et al. (1998; 1999a; 2000) showed that mackinawite produced by biostimulation under sulfate reducing conditions retarded UO_2 reoxidation. More than 90% of supplied oxygen in oxygen-saturated groundwater was consumed by mackinawite, accompanied by a constant, but low, uranium concentration in column effluent (Abdelouas et al., 2000), suggesting mackinawite may inhibit uranium oxidative mobilization. At a Rifle site amended by acetate (Colorado), Bargar et al. (2013) recently identified the close association of reduced uranium with an iron sulfide coating and indicated an abiotic reduction pathway for U(VI) in parallel to a biotic U reduction pathway by sulfate reducing bacteria.

A few laboratory experiments have investigated the abiotic role of mackinawite in aqueous U(VI) reduction under sulfate reducing conditions. Adsorption of U(VI) by synthetic

nanocrystalline mackinawite particles subsequently generated U(IV) precipitates on FeS surfaces (Hua and Deng, 2008; Hyun et al., 2012). Sediment column studies conducted by Moon et al. (2009) demonstrated that the biogenic iron sulfide precipitates were able to buffer oxygen induced U(IV) oxidation. Under anoxic conditions, the interactions of U with reduced sulfide minerals in groundwater seemed to be particularly important in controlling the mobility and bioavailability of U (Gallegos et al., 2013).

Because mackinawite is a metastable phase with high redox reactivity, it undergoes rapid oxidation-induced transformation when exposed to various oxidants, such as oxygen (Schippers and Jorgensen, 2002; Chirita et al., 2008; Bi et al., 2013), nitrate (Aller and Rude, 1988), and manganese oxides (Schippers and Jorgensen, 2002; Rickard and Morse, 2005), with half-lives ranging from minutes to a few hours under atmospheric oxygen (Rickard and Morse, 2005; Burton et al., 2009; Jeong et al., 2010a). Oxidation of mackinawite by air leads to the formation of greigite, elemental sulfur, and iron (hydr)oxides after 7 days of exposure (Boursiquot et al., 2001). After 6 months, greigite itself is entirely converted into sulfur and iron hydroxides, which are the ultimate oxidation products. In aqueous solution, mackinawite oxidation by dissolved oxygen was observed to occur much faster with a half-life ranging from minutes to a few hours in an oxygen-saturated solution (Rickard and Morse, 2005; Burton et al., 2009; Jeong et al., 2010a). Various Fe(III) species can be produced during oxidation, including goethite, lepidocrocite, ferrihydrite, and green rust-like precipitates depending on pH and oxygen concentrations (Chirita et al., 2008; Jeong et al., 2010a).

2.4 Uranium Contamination in the Environment

Uranium occurs naturally within the environment and is widespread in the earth's crust, rocks, and soils while contributing to low levels of global background radiation. Uranium is most concentrated in sedimentary rocks, particularly organic shale, with a lesser presence in metamorphic and igneous rocks (Gascoyne, 1992). While the weathering of uranium-bearing rocks and minerals is the main source of dissolved uranium in groundwater, seawater is the largest reservoir of dissolved uranium with a highly uniform concentration of 3.3 $\mu g \cdot L^{-1}$. Variations in the levels of natural uranium contamination and exposure risks depend on uranium concentration in the bedrocks and weathering conditions (WHO, 1998).

Since the 20^{th} century, anthropogenic activities have introduced U contamination at unprecedented levels through extensive mining, milling, and refining processes. In the United States, the nuclear weapons program has left a substantial legacy of environmental contamination associated with the manufacturing of nuclear weapons in a network of 113 installations around the country. For example, at the Hanford site in Washington, U contamination of soil and groundwater has resulted from storage and waste disposal practices. Uranium is present in groundwater plumes intersecting the Columbia River and was detected in the river at a concentration up to ~ 200 $\mu g \cdot L^{-1}$ (Peterson et al., 2008).

At waste disposal sites, uranium was reported to migrated to surrounding soils and groundwater in the forms of sorbed, complexed, precipitated, or reduced species (Gavrilescu et al., 2009) (Figure 2.2). The mobility and fate of uranium are often controlled by its oxidation state, which is primarily U(IV) and U(VI) in essentially all geological environments. In the oxidized form in groundwater, U(VI) usually exists as soluble uranyl ion (UO_2^{2+}) complexes associated with carbonate and calcium, such as $(UO_2)_2CO_3(OH)_3^-$.

$CaUO_2(CO_3)_3^{2-}$, and $Ca_2UO_2(CO_3)_3^0$ (Dong and Brooks, 2006). Although soluble and mobile, uranyl and related species may sorb to soils and sediments, lowering dissolved uranium concentration and, thus, their potential of migration. Many subsurface soils and sediments strongly react with U(VI) species via adsorption, resulting in a significant retardation of uranium transport under oxic conditions (Barnett et al., 2000; Hyun et al., 2009; Boland et al., 2011). For example, in studies of adsorption of uranium to various Fe (hydr)oxides, uranyl-carbonato complexes were thought to be the dominant surface species (Bargar et al., 1999; Bargar et al., 2000). Increasing concentrations of carbonate and calcium in groundwater, however, can increase uranium solubility and limit its adsorption on mineral surfaces (Barnett et al., 2000; Wazne et al., 2003).

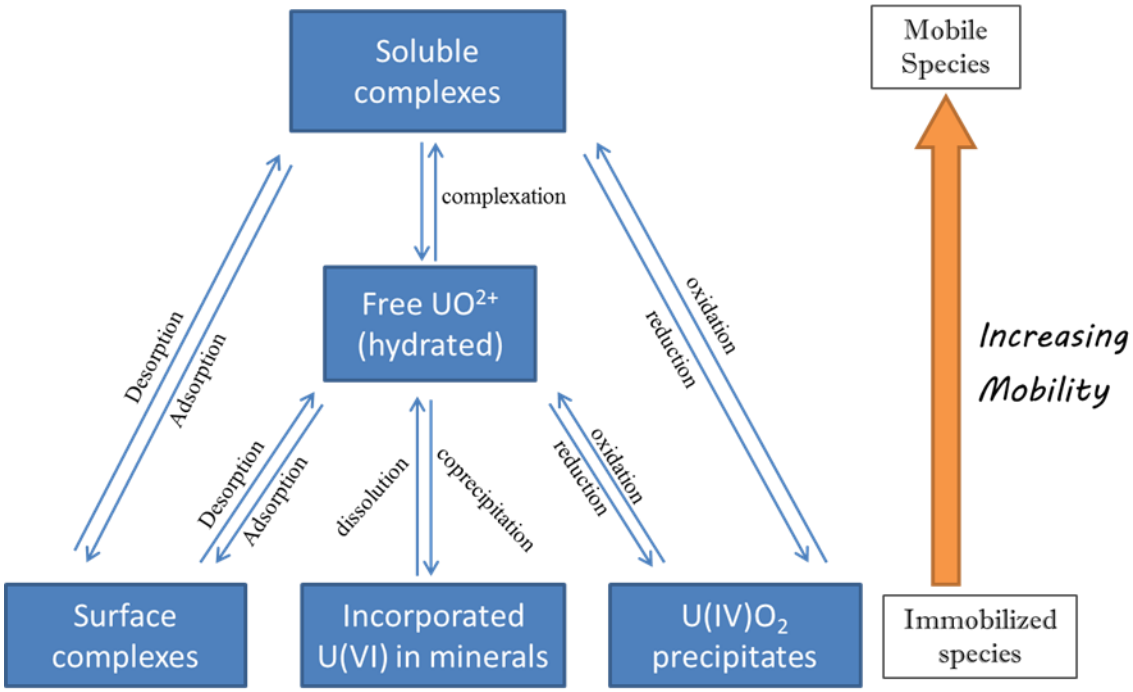

Figure 2.2 Transformation between uranium species in the environment and the relative mobility.

Although uranium speciation is controlled by site-specific geochemical conditions, uranium contamination is often dominated by U(VI) oxidation state at various DOE sites,

such as the Savannah River site and the Hanford site. Uranium was observed to be highly mobile when dissolved carbonate concentrations are high due to the formation of uranyl-carbonate species. As a retention mechanism, the sorption of U(VI) species to aquifer materials is frequently dominated by their association with iron hydroxide minerals. In contrast, high phosphate concentration in groundwater system can lead to the precipitation of uranium in very insoluble uranyl phosphate minerals.

2.5 Uranium Immobilization and Reoxidation

Under anaerobic conditions, U(VI) species may be reduced through a number of abiotic (Wersin et al., 1994; Behrends and Van Cappellen, 2005) and microbially mediated processes (Lovley et al., 1991; Lovley and Phillips, 1992; Abdelouas et al., 2000). Many microorganisms have been shown to mediate the reduction of U(VI), including Fe(III)-reducing bacteria (Lovley et al., 1991; Ganesh et al., 1997) and sulfate-reducing bacteria (Fredrickson et al., 2000; Holmes et al., 2002). Reduced U(IV) species are predominantly in the form of sparingly soluble U(IV) solid phases such as uraninite (UO_2). Recent studies also suggest the presence of monomeric U(IV) species, which may initially form in association with phosphate as a sorbed complex on soils and sediments (Bernier-Latmani et al., 2010; Fletcher et al., 2010; Veeramani et al., 2011). The monomeric U(IV) may be important as a more mobile form of U(IV) under reducing conditions (Cerrato et al., 2013), but its reactivity (i.e., lifetime) and relative concentration in the field are still unknown (Veeramani et al., 2011).

Because solid-phase uraninite is relatively immobile and thermodynamically stable under reducing geological and sedimentary environments (Ulrich et al., 2008), biostimulation

of uranium reduction has been investigated for over a decade and seemed to be effective (Phillips et al., 1995; Kelly et al., 2008; Ulrich et al., 2009; Moon et al., 2010). For example, a column study performed at the DOE Natural and Accelerated Bioremediation Research (NABIR) site in Oak Ridge, TN suggested that the bioreduction of U(VI) was feasible for U immobilization (Gu et al., 2005). A pilot-scale study carried out at the same site was successful in reducing U concentrations in the groundwater by adding carbonate to raise the bioavailability of U(VI), with the subsequent addition of ethanol to stimulate microbial activity for the *in situ* precipitation of reduced U(IV) solids (Wu et al., 2006a; Wu et al., 2006b).

Biostimulation is not trouble free, with concerns raised over the long-term stability of bioreduced and immobilized uranium. The nanometer-size uraninite produced by microorganisms could be mobile in porous sediments and more susceptible to oxidation than bulk uraninite (Suzuki et al., 2002). Reoxidation of uraninite to soluble U(VI) may occur when subjected to oxidants such as oxygen (Zhou and Gu, 2005; Moon et al., 2007; Komlos et al., 2008; Moon et al., 2009), nitrate (Finneran et al., 2002; Senko et al., 2002), Fe(III) (hydr)oxides (Sani et al., 2005; Wan et al., 2005; Ginder-Vogel et al., 2010), and manganese oxide (Fredrickson et al., 2002). The processes can be enhanced by the presence of carbonate and calcium (Casas et al., 1994; Ulrich et al., 2008).

Upon exposure to oxygen, UO_2 is unstable and can be effectively oxidized and consequently dissolved (de Pablo et al., 1996; Pierce et al., 2005). Oxidative dissolution of UO_2 by oxygen has been proposed to occur through a sequence of reaction steps, including oxygen adsorption, formation of activated surface complexes, electron transfer, and subsequent release of U(VI) products (Stumm, 1987; Torrero et al., 1997). While the

dissolution rates of UO_2 increase with increasing oxygen partial pressure, the lowest dissolution rate occurs at circumneutral pH at a given oxygen level (Torrero et al., 1997; Pierce et al., 2005). In the presence of carbonate, dissolution rates of UO_2 are enhanced through the formation of the predominant aqueous uranyl-carbonato complexes (Ginder-Vogel and Fendorf, 2007; Bargar et al., 2008), which can facilitate the detachment of U(VI) passivating layers. Common cations in groundwater, such as Ca^{2+} and Mg^{2+}, may further enhance UO_2 oxidative dissolution by promoting the detachment of oxidized U(VI) surface species via the formation of ternary complexes (Ulrich et al., 2009; Stewart et al., 2010).

The oxidation of UO_2 by iron hydroxides has been investigated by several research groups under the assumptions that iron hydroxides are ubiquitous in the subsurface environments (Cornell and Schwertmann, 2003) and may serve as effective oxidants. Sani et al. (2005) and Ginder-Vogel et al. (2010) showed that iron oxides can accelerate the abiotic oxidative dissolution of reduced U(IV) solids under sulfate reducing conditions, but the relationship between the type and amount of Fe(III) and the rate of U(IV) reoxidation has not been fully examined. The thermodynamic favorability of UO_2 oxidation by Fe(III) hydroxides depends on the geochemical conditions because of the close proximity of the electrochemical potential of the two redox couples (i.e., U(IV)/U(VI) and Fe(II)/Fe(III)) (Ginder-Vogel et al., 2006). As an evidence of this, Du et al. (2011) examined the thermodynamic constraints for the redox couples and claimed the possibility of U(VI) reduction by soluble Fe(II). These results suggest that further studies on UO_2 oxidation by Fe(III) hydroxides should carefully choose the geochemical conditions and consider both thermodynamic and kinetic limitations.

The introduction of nitrate, a common co-contaminant with uranium (Riley et al., 1992), may also result in reoxidation of UO_2 as observed by Senko et al. (2002) in field and laboratory studies. Although kinetics does not favor UO_2 abiotic oxidation by nitrate (Finneran et al., 2002; Senko et al., 2005b; Moon et al., 2007), the intermediates of dissimilatory nitrate (e.g., NO_2^-, N_2O, and NO) produced by denitrifiers may oxidize and mobilize U(IV) (Senko et al., 2002; Wu et al., 2007). The overall oxidation rates, however, are still significantly slower than those by oxygen and Fe(III) hydroxides (Senko et al., 2005a). The remobilization of uranium by nitrate should therefore be understood as a combined effect of biotic and abiotic activities. In a strictly abiotic system, nitrate should have only minor, if any, influence on UO_2 oxidation.

2.6 Uranium Sorption on Iron Hydroxide Minerals

The mobility of U(VI) is limited by its tendency to sorb on mineral surfaces, a reaction which can strongly retard the transport of U in soil and groundwater. Iron hydroxides are believed to be of particular importance due to their high sorptive capacities for uranium, high surface areas, and common occurrence in natural systems. When mackinawite is oxidized by dissolved oxygen, goethite and lepidocrocite are identified as major oxidation products that may influence the transport of U(VI) in groundwater (Bi et al., 2013). Therefore, an investigation of U(VI) adsorption behavior onto Fe(III) hydroxides is necessary for understanding the long-term stability of U in close association with iron sulfide minerals.

The Sorption of U(VI) on goethite and lepidocrocite has been shown to follow a Langmuir isotherm (Moyes et al., 2000). Sorption increases from essentially none to a

maximum value across a sharp sorption edge in the pH region of 4-6, with the maximum sorption occurring at circumneutral pH. In the atmosphere, however, the presence of CO_2 results in a desorption of U(VI) at pH > 8 due to the formation of stable uranyl-carbonato (e.g., UO_2CO_3) complexes in solution (Hsi and Langmuir, 1985; Sherman et al., 2008). In a groundwater system, stronger desorption of U(VI) from goethite may occur since dissolved carbonate is often present at a concentration 100 to 1000 times greater than that expected in equilibrium with air.

A number of studies have been done to understand the mechanism of U sorption and to develop surface complexation models to predict U retention and mobility in the environment. While sorption is believed to occur by forming inner-sphere surface complexes, the specific composition and reaction stoichiometry are known with much less accuracy. Recent investigations of surface complexes are aided by synchrotron-based X-ray spectroscopic analysis and density functional theory (DFT) calculations in addition to batch sorption experiments. For example, Bargar et al. (1999; 2000) utilized EXAFS to measure U(VI) adsorption on hematite and suggested the existence of anionic U(VI)-carbonato ternary complexes with bidentate coordination to the hematite surface. The Fe-oxide-U(VI)-carbonato complexes may be important transport limiting species in oxic aquifers within a wide range of pH values.

Similar characterization techniques have been applied to other iron hydroxide systems to examine surface complexes. In the absence of dissolved carbonate, EXAFS data suggested a mononuclear inner-sphere, edge-sharing complex of U(VI) with ferrihydrite (Ulrich et al., 2006). In the presence of dissolved carbonate and at pH similar to 8.0, a distal carbonate O-atom at ~4.3 Å supports the formation of bidentate ternary U(VI)-carbonato surface

complexes. However, in slightly acidic conditions (pH 5-6), the type of complexes may change from ternary carbonato-uranyl-ferrihydrite to binary uranyl-ferrihydrite complexes, which are likely to influence the binding stability and retention of U(VI) at the macroscopic level.

2.7 Knowledge Gaps and Hypotheses

A review of literature reveals that iron sulfide minerals have the potential to serve as redox buffers to retard reduced U(IV) solids from rapid oxidation. However, the current literature lacks sufficient detail to assess the importance of abiotic redox processes in controlling the transport and transformation of uranium in the subsurface during anoxic-oxic transitions, when iron sulfides are also present. There are a number of questions that need to be addressed to evaluate the role of FeS for oxidant scavenging and the consequent impact on long-term sequestration of uranium, including: (i) what quantity of iron sulfide minerals must be present relative to various oxidants to maintain a low redox potential; (ii) is a large excess iron sulfides relative to reduced uranium needed to keep uranium reduced in event of reentry of oxidants; (iii) what impact do geochemical conditions such as pH, carbonate and calcium concentrations have on reduced uranium reoxidation; and (iv) will oxidation products of iron sulfides impact uranium remobilization, once the iron sulfides are exhausted by the oxidants.

To better predict the fate of uranium under a scenario where active bioreduction ceases, an improved understanding in the thermodynamics and kinetics of heterogeneous redox reactions during anoxic-oxic transitions is necessary. By focusing this work on abiotic redox processes, this dissertation seeks to address the key steps of oxidative mobilization

processes controlling uranium retention in the subsurface. Several hypotheses provide the impetus for this work:

1. Mackinawite will abiotically inhibit the rapid oxidation of reduced U(IV) solids by oxygen and Fe(III) (hydr)oxides by serving as an oxidant scavenger.
2. Uranium will remain reduced as UO_2 in the presence of excess FeS until the reduction capacity is depleted, after which the adsorption of U(VI) by FeS oxidation products will become the major removal mechanism from the aqueous phase.
3. The inhibited rate of UO_2 oxidative dissolution by mackinawite will depend on geochemical conditions, such as solution pH, DO levels, FeS content, and calcium concentrations.
4. The efficiency of oxygen removal by FeS will depend on solution pH and DO concentration, as these parameters impact FeS oxidation processes.
5. After the reduction capacity of FeS is depleted, the release rate of dissolved U(VI) will be enhanced, depending on solution pH, FeS content, and DO concentration.
6. During the anoxic-oxic transition, the extent of the formation of a passivation layer on UO_2 surface will depend on the initial concentration of FeS and solution pH.
7. Under conditions that limit the formation of a passivation layer on UO_2, a more rapid attack /oxidation by dissolved oxygen will occur.

Chapter 3

Materials and Methods

This chapter introduces the chemical synthesis methods, solid phase characterization techniques, and reactor system design and operations. Specifically, the methods of synthesis and characterization of abiotic mackinawite, uraninite, and two-line ferrihydrite solids are described, along with a description of the batch and flow-through systems used for conducting oxidation experiments in oxic groundwater solution. In addition, the suite of analytical techniques used for determining aqueous species concentration, as well as solid phase structure, morphology, chemical oxidation state, and local coordination environment of reactive solid phase surface species. Lastly, the physical and chemical properties of synthetic mackinawite and uraninite particles are characterized using the analytical tools introduced above. As described in subsequent chapters, the methods detailed in this chapter allow for determining the rate of oxidation reaction, characterization of the oxidation products from the reactions of oxygen with FeS and UO_2, and the mechanisms of these reactions.

3.1 Solid Material Preparation

With a few exceptions, chemical preparation was conducted inside an anaerobic chamber (Coy Inc, Grass Lake, MI) with an atmospheric composition of ~5% H_2 balanced with N_2 gas. All chemicals were reagent grade unless otherwise specified. Aqueous solutions

were prepared with deoxygenated MilliQ water (with a resistivity of 18.3 MΩ·cm) that was boiled and purged with ultra high purity N_2 gas.

3.1.1. Mackinawite Synthesis

Mackinawite (FeS) was synthesized by mixing 1.1 M Na_2S solution with 0.57 M $FeCl_2$ solution (S:Fe ≈ 1.93) in a two liter flask in an O_2-free atmosphere following the procedure described in Butler and Hayes (1998). Black precipitates immediately formed in the mixed solution, which was stirred constantly stirring for an additional three days to allow aging. The glass flask was sealed tightly with a rubber stopper to prevent potential oxidation. The aged solid was then repeatedly washed (8 times) with deoxygenated MilliQ water and centrifuged at 10,000 rpm for 15 min. The final product was freeze-dried under vacuum and stored in capped glass vials inside the anaerobic chamber until use.

3.1.2 Uraninite Synthesis

Uraninite (UO_2) was produced by the reductive precipitation of uranyl nitrate (500 ppm, Antec Chemical) using a sodium sulfide solution in the anaerobic chamber following a procedure described by Beyenal et al. (2004). A sulfide solution (0.5 M) was added to a uranyl nitrate solution to achieve a molar ratio of 5:1 [S(-II): U(VI)] for complete reduction of U(VI). The mixture has a light orange color and a pH of ~10.8. The solution pH was then quickly adjusted to pH = 7 by adding 1 M hydrochloric acid. Within 30 min, brown precipitates started to form in the solution and accumulate over the next two days. After 3 days of aging, the dark brown precipitate was washed six times with deoxygenated water and two times with 30 mM bicarbonate solution. The final solids were stored in a suspension of

~15 mL MilliQ water in anaerobic chamber until use (typically within two months). For each set of completely mixed batch reactor experiments, UO_2 solid was freshly prepared, resulting in a slight variation in concentration. For the completely mixed flow-through reactor system, a batch of UO_2 solids was prepared for conducting multiple experiments to ensure constant concentration between experiments.

3.1.3 Two-line Ferrihydrite Synthesis

Two-line ferrihydrite is a poorly crystalline iron(III) hydroxide that was prepared by mixing ferric nitrate solution (0.1 M) with 1 M potassium hydroxide following a modified method of Schwertmann and Cornell (2000). As a result of the rapid hydrolysis of Fe(III), a reddish brown precipitate formed immediately upon mixing the two solutions. A potassium hydroxide solution was slowly added afterwards to bring the final solution pH to 7.5 under vigorous stirring. The precipitate was then centrifuged and washed with deoxygenated MilliQ water for six times to remove electrolytes. The final suspension was then bubbled with O_2-free N_2 gas for one hour to remove any O_2 dissolved in solution or sorbed to mineral surfaces. The ferrihydrite solids were stored in a suspension in the anaerobic chamber, and used within one month of synthesis to prevent ferrihydrite transformation into goethite or hematite.

3.2 Oxidation Experiment Design and Operation

The synthetic solids were subject to oxidation reactions with dissolved oxygen in an artificial groundwater to simulate oxidizing conditions when active bioreduction is halted and oxygen intrusion occurs. The artificial groundwater contained $NaHCO_3$, KCl, and $CaCl_2$ and

was constantly sparged with $O_2/CO_2/N_2$ gas mixture to achieve the desired solution pH and DO concentration. Although the solution did not represent a real groundwater with all constituents, it included the most important components affecting the oxidative dissolution of UO_2 (see Chapters 4 and 5). To study the reaction mechanisms and kinetics, completely mixed batch and flow-through reactor systems were designed and used to retain FeS and UO_2 solids within the reactor as a function of time under various geochemical conditions.

3.2.1 Batch System and Operation

A glass one-liter completely mixed batch reactor (CMBR) (CG-1926-02, Chemglass Life Sciences) was utilized to conduct oxidation experiments with FeS and UO_2 in pH = 7 artificial groundwater solution (Figure 3.1). The batch reactor was equipped with a water jacket and a 5-port lid to accommodate various probes and a sampling port. This reactor allows for gas mixtures with fixed partial pressures (e.g., P_{CO2} = 0.05 atm) to be introduced and temperature maintained at 25 ℃ by a circulating water bath. The reactor lid was sealed by silicone grease (ALCO) to prevent air diffusion into the reactor.

An oxidation experiment was initiated upon the addition of FeS or UO_2/FeS mixed suspensions into the reactor. Aliquots of suspension were periodically withdrawn through the sampling port and analyzed for both aqueous and solid products. Suspension pH, DO, and Eh were measured *in situ* by calibrated probes located on the ports of the lid, which remained in the solution over the entire reaction period. The suspensions were constantly and vigorously stirred to ensure immediate and complete mixing.

The large volume batch reactor (1 L) was chosen mainly for accommodating enough solid suspension for aqueous and solid chemical analysis. Each suspension sample (~10 mL)

contained enough material so several complementary characterization techniques could be used to monitor the reaction as a function of time. For each experiment, less than 200 mL of total suspension was sampled, minimizing the volume changes that could affect the reaction kinetics. The detailed experimental conditions are provided in Chapter 4.

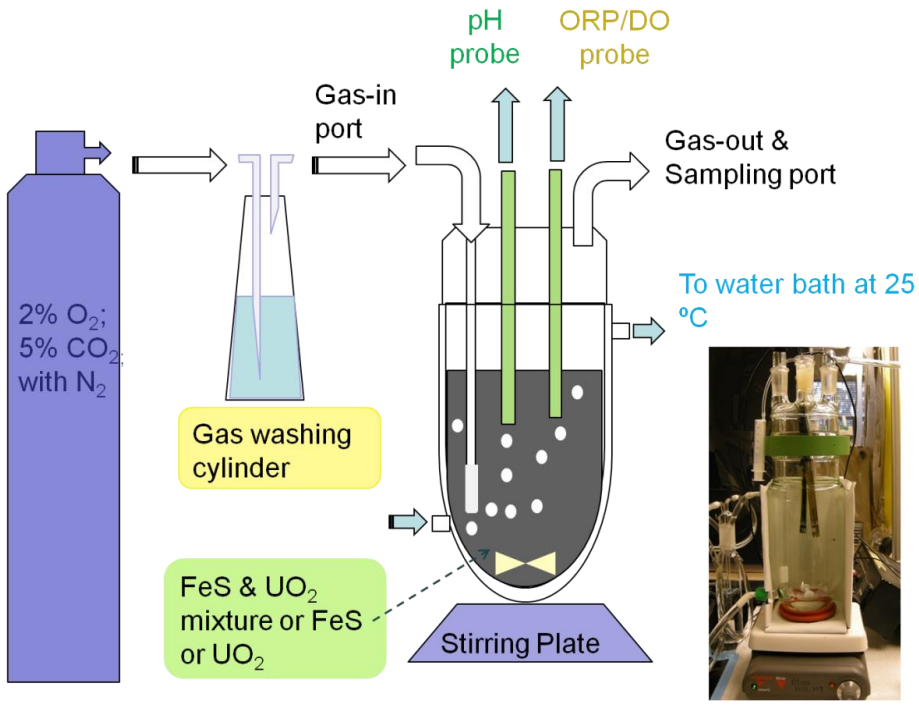

Figure 3.1 Schematic of the batch reactor system used for the oxidation of FeS and UO_2 suspensions in pH-controlled oxic groundwater.

3.2.2 CSTR System Design and Operation

The flow-through experiments were conducted with 50 mL continuous-flow stirred tank reactors (CSTRs) (Millipore 8050), the core component in the reactor system. The complete flow-through system includes a gas cylinder, feed solution container (1 gallon gas-tight glass jug), peristaltic pump, magnetically stir plates, CSTR, and an effluent collection/measurement system (Figure 3.2). Influent solutions of artificial groundwater were purged and equilibrated with custom $CO_2/O_2/N_2$ gas mixtures for at least two hours before experiment started. Suspensions of mixed iron and uranium solids were added to the CSTR

to obtain a total reactant volume of 50 mL. The reactor body was made of polysulfone, allowing for a clear view of the suspension retained in the reactor while replenishing the aqueous solution. The flow rates were controlled by a peristaltic pump (Watson-Marlow, 205U/CA), maintained between 1.8-2.2 mL min^{-1} and gravimetrically monitored during sampling. The flow rates were chosen to achieve steady-state dissolved U concentration ($[U]_{diss}$) far below saturation, resulting in a ~25 min hydraulic residence time (τ). Eh, pH, and DO concentrations were constantly monitored with probes installed at the end of the supply line. The effluent samples from the CSTR, passed through 0.1 μm (Millipore) filter membranes at the bottom of the CSTR, were periodically collected and preserved in 1% HNO_3 for chemical analysis. All experiments were operated at room temperature (24 ± 1 ℃) and covered by aluminum foil to avoid light.

For experiments under anoxic conditions, artificial groundwater and FeS/UO_2 suspension were prepared in the anaerobic chamber using deoxygenated MilliQ water. The CSTR and pumping system were also transferred to an anaerobic chamber with an oxygen concentration of less than 10 ppm.

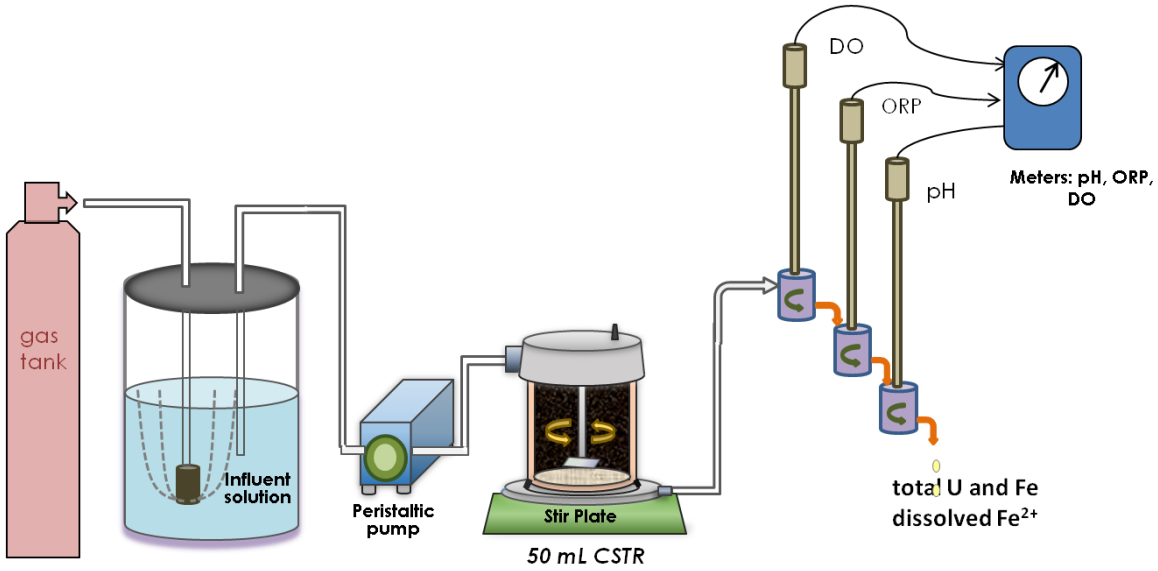

Figure 3.2 Schematic of the flow-through reactor system.

During flow-through operation, steady-state dissolution of uraninite is desirable for determining reaction kinetics. When a steady-state rate of dissolution of uraninite is established, the total dissolved uranium concentration in the effluent is constant. In Chapter 5, the rate analysis of UO_2 oxidative dissolution in the presence and absence of FeS is discussed. The steady-state rate obtained from the experiment assumes a perfectly stirred reactor and the reaction kinetics are not limited by equilibrium or mass transfer. The dissolution rate in the CSTR was determined under different stirring rates and flow rates to optimize the experimental conditions and to minimize the effect of mass transfer.

3.3 General Analytical and Characterization Methods

The synthetic minerals prepared for oxidation experiments were subjected to a thorough characterization to confirm the mineral phase, and to determine the particle size and specific surface area. In the batch and flow-through reactor systems, oxidized FeS and UO_2 particles and their oxidation products were analyzed for assessing reaction mechanisms. Both aqueous species and solid phases were examined using a combination of analytical and characterization techniques which are briefly discussed in the following sections.

3.3.1 Inductively Coupled Plasma-Mass Spectrometry (ICP-MS)

ICP-MS is a multi-element technique that can be used to determine the concentrations of metals and non-metals at concentrations as low as one ppb in an aqueous solution. The high sensitivity and accuracy of ICP-MS measurements for total dissolved metals are achieved by ionizing the aqueous solution with inductively coupled plasma and using a mass spectrometer (quadrupole) to separate and quantify those ions.

In this dissertation research, total dissolved calcium, iron, and uranium concentrations in aqueous samples were regularly measured by a PerkinElmer ELAN DRC-e ICP-MS. Uranium calibration standards from 0 to 50 ppb were prepared in 1% nitric acid solution using a 1000 ppm uranium standard. Standards were also prepared for iron (0 - 5 ppm) and calcium (0 - 100 ppm) using the corresponding standards (1000 ppm). An internal line gallium standard (10 ppb) was used as a reference for monitoring instrument performance. The samples collected from batch and flow-through experiments were acidified by concentrated nitric acid to ensure an overall nitric acid content of ~1%. A dilution of samples was performed as needed to achieve concentrations within the working range of standard curves. The ICP-MS instrument has a detection limit for total dissolved calcium, iron, and uranium of approximately 1 ppm, 0.1 ppm and 0.5 ppb, respectively. For quality control, one standard solution was measured as a sample every five samples. The calculated percentage errors for uncertainty of the three elements were all less than 5%.

3.3.2 Ultraviolet-Visible Spectrophotometry

Colorimetric analysis is a common method of determining the concentration of chemical element or chemical compound in a solution. After reacting with a color reagent, the analyte exhibits characteristic absorption spectrum in the UV- visible range of light from about 200 nm to 780 nm. The light-absorbing analyte can then be quantitatively related to its concentration using Beer-Lambert law (Equation 3.1), which shows a linear relationship between absorbance and concentration of an absorbing species:

$$A = \varepsilon l C \qquad \text{(Equation 3.1)}$$

where A is absorbance, l is path length, ε is absorption coefficient, and C is molar concentration of absorbing species.

In this dissertation research, UV-visible spectroscopy was used to determine the concentration of dissolved Fe(II) species. Divalent Fe reacts with ferrozine reagent to form a stable magenta complex species at neutral pH (Stookey, 1970). The maximum absorbance occurs at 562 nm with a molar absorption coefficient close to 30,000 $L \cdot mol^{-1} \cdot cm^{-1}$ at pH = 7. Appropriate concentrations of standards ranging from 0- 20 µM were made to obtain a calibration range.

For the measurement of Fe(II) in aqueous samples, a 1 mL sample solution was typically reacted with 1 - 4 mL ferrozine stock solution (1 g/L) at pH = 7 (buffered with 50 mM HEPES). Within two hours of reaction, the absorbance of samples and standards were analyzed using a UV/Vis spectrophotometer (Varian) or FLx800 Fluorescence microplate reader (BioTek) at a wavelength of 562 nm. A quartz cuvette (0.5 cm path-length) or a 96 well standard microplate (0.4 mL) was used. The Fe(II) concentration was calculated using predetermined molar extinction coefficient of $_{nm}$ 28860 ± 50 $M^{-1}cm^{-1}$. The Fe(II) concentration determined by this method was compared to that obtained by ICP-MS to confirm that all measurable Fe in aqueous solution was Fe(II) within error.

3.3.3 X-ray Diffraction (XRD)

X-ray diffraction (XRD) is one of the primary characterization techniques used in this dissertation to identify iron- and sulfur-bearing solid phases and crystal structure. Due to the periodic arrangement of atoms in a crystal, an incident X-ray wave with the wavelength λ is

reflected with maximum intensity when the Bragg condition is fulfilled (Figure 3.3). This condition for constructive interference is described by Bragg's law:

$$2d \sin\theta = n\lambda \qquad \text{(Equation 3.2)}$$

where d is the interplanar distance in a crystal, θ is the scattering angle, n is an integer determined by the order given, and λ is the wavelength of the incident X-ray beam.

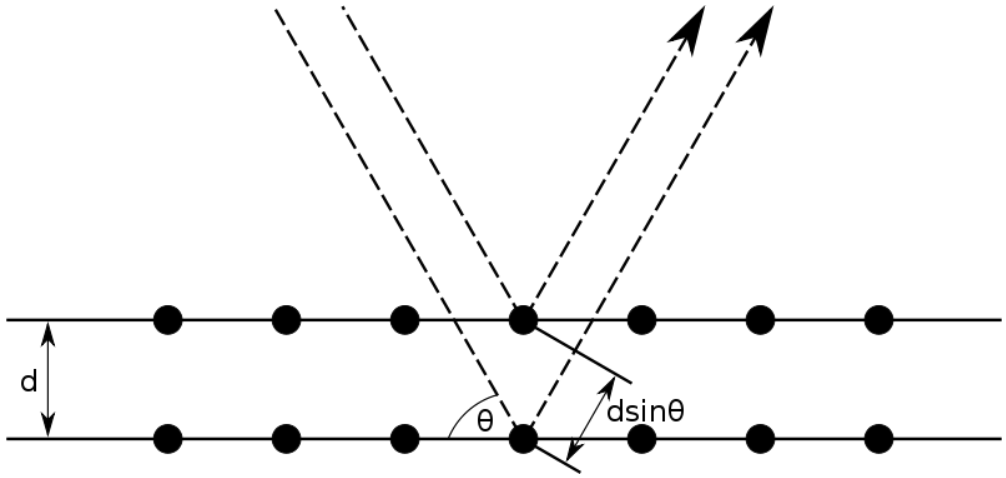

Figure 3.3 Bragg diffraction when two beams with identical wavelength and phase approach a crystalline solid and are scattered off two different atoms within it. Constructive interference occurs when the difference of travel distance is equal to an integer multiple of the X-ray wavelength.

For XRD analysis, solid samples were prepared by mounting the wet paste onto glass slides using a spatula to produce a smooth thin layer. The slides were then dried in an anaerobic chamber to prevent sample oxidation. For powder samples of more than 0.5 g, solids were crushed with a mortar and pestle and pressed onto a glass plate with a shallow depression. Diffraction patterns were typically collected over the range of 10-70° 2θ using a Rigaku rotating anode diffractometer equipped with a monochromated Cu-Kα source (λ=1.54 Å) and operated at at 40 kV and 100 mA. The diffraction pattern was recorded with a step mode, a step size of 0.05 °, and counting times of 2.5 s per step (total pattern collection time of 50 min per sample).

The X-ray diffraction pattern contains characteristic sets of Bragg reflections for single or mixed crystalline materials present in the sample. A data processing software JADE9.5 (Materials Data Inc.) was used to determine peak position and widths of individual diffraction peak with an optimization routine of peak fitting and decomposition. By comparing the patterns with standard references in a crystallographic database (ICDD), the iron and sulfur solids produced from FeS and UO_2 oxidation reactions were identified. Using the *Scherrer* equation, the crystallite size of solids was estimated in some cases based on the broadening of a peak in a diffraction pattern.

3.3.4 Transmission Electron Microscopy (TEM)

Transmission electron microscopy uses a high energy electron beam which passes through a thin-section to image and analyze the microstructure of materials with nano- to atomic- scale resolution. The electrons are focused with electromagnetic lenses and the image is observed on a fluorescent screen and recorded on a digital camera. Information about the morphology, crystal structure and defects, and chemical composition can be obtained by a combination of electron-optical imaging, electron diffraction, and X-ray spectrometry. The X-ray produced by the incident beam after interacting with specimen is especially useful for determining chemical information, which is characteristic of the elements contained in a sample. In this dissertation research, TEM analyses were performed on synthetic FeS and UO_2 particles and their oxidation products to observe crystal size and to identify phases to supplement other characterization techniques.

All TEM samples were prepared by diluting solid suspensions with de-oxygenated DI water to achieve a solid concentration of ~ 0.5 g/L. One drop of suspension was dried on an

ultra thin lacey carbon film coated 300-mesh Au grid (Ted Pella, Inc) in an anaerobic chamber. The prepared specimens were transferred in the vacuum container to the TEM chamber to minimize possible oxygen exposure.

A JEOL 2010F analytical electron microscope (AEM) operated at 200 kV was used for conventional bright-field (BF) TEM, high-resolution electron microscopy (HREM), selected area electron diffraction (SAED), and X-ray energy dispersive spectroscopy (XEDS). Image processing, including the generation of diffraction patterns, was completed using Gatan Digital Micrograph 3.6.4.

3.3.5 X-ray Photoelectron Spectroscopy (XPS)

X-ray photoelectron spectroscopy is a surface-sensitive chemical analysis technique that measures the elemental composition, oxidation state and electronic state of the elements that exist within a material. XPS uses monochromatic soft X-ray beam (e.g., Al-Kα or Mg-Kα) to irradiate a sample while simultaneously ejecting electrons from core levels of atoms. The identification of the elements present on the sample surface (1-10 nm) can be directly determined from the kinetic energies (binding energies) of the ejected photoelectrons characteristic of a particular element. XPS also allows for the determination of the oxidation state of the elements present from small variations in the measured binding energies and other structural effects.

Because of its sensitivity to surface-bound uranium, XPS analysis was primarily used for determining the oxidation state of uranium during oxidative dissolution in the presence and absence of FeS. Wet paste samples from selected flow-through experiments were collected on filter paper using a hand-operated vacuum pump inside an anaerobic chamber.

The dried powders were then mounted on double-sided Cu tape. The samples, kept inside airtight containers, were transferred to the XPS chamber with less than 1 min exposure time.

XPS spectra were collected on a Kratos Axis Ultra XPS using a monochromated Al-Kα X-ray source (1486 eV). The charge neutralizer filament was used for all samples to control charging of particles that were in poor contact with the stage. Surface charging effects were corrected using the adventitious carbon 1s spectral line at a binding energy of 284.5 eV. Survey and narrow-scan XPS spectra were obtained using pass energies of 160 and 20 eV, respectively. Survey scans were used to determine the average composition of the surface. The semiquantitative composition of the near-surface layer was calculated from the peak areas of the Fe(2p), S(2p), O(1s), and U(4f) peaks and normalized by their respective sensitivity factor. Narrow-scan spectra were collected for U (4f), C (1s), and Fe (2p) peaks to determine the speciation and oxidation states of these elements.

Raw spectra, after smoothing and energy calibration, were fitted into a Shirley baseline and a Guassian-Lorentzian peak shape. Abiotic shoepite was used as a standard for U(VI) when fitting sample spectra. Best fits were acquired using the fitting routine in CasaXPS. Uranium-4*f* spectra were fitted with a doublet of U4$f_{7/2}$ and 4$f_{5/2}$ peaks with a spin-orbit splitting of ~0.67 eV. The peak area of U4$f_{5/2}$ was constrained to be three quarter (3/4) of the U4$f_{7/2}$ peaks. The full width at half maximum (FWHM) of all the core peak components was constrained to be the same in the fits, within ranges reported in the literature. Using the binding energies determined from a U(VI) reference standard, the U(IV) peak position was further determined. The relative concentration of U(VI) and U(IV) were calculated from peak areas of fitting results and reported as percentages.

3.3.6 X-ray Absorption Spectroscopy (XAS)

X-ray absorption spectroscopy uses synchrotron radiation as a photon source to produce extremely intense and tunable X-ray beams that interact with backscattering elements within a sample. The XAS signal comes from all of the atoms of a single element as selected by the X-ray energy. XAS includes both X-ray absorption near edge structure (XANES) and extended X-ray absorption fine structure (EXAFS) analyses. While XANES can be used to determine the valence state and coordination geometry, EXAFS is often used to determine the local molecular structure of a particular element within a sample. Because XAS probes the near coordination environment of the selected element, within about 6 Å, and its theory and interpretation does not rely on any assumptions of symmetry or periodicity, XAS can be used for the analysis of amorphous, liquid, molecular systems in addition to crystalline materials.

In this research, selected solid samples from batch and flow-through experiments were collected as a function of reaction time for XAS analysis. For U and Fe analysis, samples of wet paste were diluted with boron nitride and placed into aluminum sample holders. For S analysis, a thin suspension was deposited in a recessed area of a polycarbonate sample holder and dried inside the anaerobic chamber to minimize oxidation. XAS data measurements were performed at the Stanford Synchrotron Radiation Lightsource (SSRL) from 2010 to 2013. Uranium L_{III}-edge and iron *K*-edge absorption spectra were collected in fluorescence mode at beamline 4-1 or 11-2 using a 13- or 100-element Ge detector at a low temperature (77 K). A liquid nitrogen cryostat (77 K) was used to reduce thermal disorder and improve the signal to noise ratio. The beam energy was calibrated to 17038 eV of Y *K*-edge position for U and 7112 eV of Fe K-edge position for Fe. Sulfur *K*-edge spectra were

collected at beamline 4-3 in fluorescence mode using a passivated implanted planar silicon (PIPS) detector at room temperature under an inert (He) atmosphere. Prior to the data collection for each sample, the beam energy was calibrated to the maximum of the first edge feature of a $Na_2S_2O_3 \cdot 0.5H_2O$ sample at 2472.02 eV. Multiple scans were collected for all XAS samples to improve the signal to noise ratios.

XAS data were subjected to XANES and EXAFS analyses. Prior to analysis, XAS spectra were energy-calibrated and averaged. EXAFS were extracted and k^3-weighted from averaged data files after background subtraction and spline fitting using SixPACK and IFEFFIT code (Newville, 2001; Webb, 2005). Backscattering phase and amplitude functions for EXAFS fitting were obtained using FEFF 6 code with crystallographic input files generated by ATOMS (Rehr et al., 1992). To obtain the optimal structural parameters, including coordination numbers (*CN*s) and interatomic distances (*R*), the mean-square disorder (^{2}) and energy reference E_0 parameters were allowed to float during the fitting. For linear combination fitting (LCF) of first-derivative U XANES, a uranyl(VI) nitrate solution and a crystalline UO_2 solid sample were used as U(VI) and U(IV) reference standards, respectively. The uncertainty of valence state determinations from XANES data is generally ~10% (Boyanov et al., 2007). LCF of S XANES spectra were conducted using synthetic mackinawite and AR-grade S_8^0 as standards of S(-II) and S(0), respectively. To address S_8^0 particle-size effect on XANES absorbance in fluorescence mode (Pickering et al., 2001), both finely ground (~1–10 μm) and dissolved (1% w/v in toluene) S_8^0 were used as S(0) model compounds (Burton et al., 2009). The uncertainty of the LCF is generally about 10% for sulfur XANES spectra (Prietzel et al., 2011).

Modeling of the U EXAFS data included two U-O single scattering (SS) paths, one U-U SS path, and the multiple scattering (MS) paths from two neighboring oxygen atoms. The many-body factor S_0^2 was fixed at 0.9 to reduce the number of fitting parameters. Accuracies of interatomic distances and *CN*s were estimated to be ±0.02 Å and ±20%, respectively.

3.3.7 Other Analytical Techniques

Ion chromatography (IC) allows the separation and quantification of ions and polar molecules in aqueous solution based on their affinity to the ion exchanger (i.e., resin). In this dissertation research, a Dionex DX-100 was utilized to measure the concentrations of aqueous $S_2O_3^{2-}$ and SO_4^{2-} species with an IonPac® AS9 column (Dionex) and an eluent comprised of 3.5 mM $NaHCO_3$ and 1.5 mM Na_2CO_3 solutions.

To determine the concentration of elemental sulfur, an oxidation product of FeS, an oxidized suspension was first extracted by tetrachloroethylene (TCE) for 20 hours to allow adequate equilibration time. The dissolved S_8^0 in TCE was then analyzed by liquid chromatography (LC, Agilent 1090) with an eluent of 95%:5% methanol: water (McGuire and Hamers, 2000). The analysis of S_8^0 using the LC has a precision of about ± 7%.

As a complementary technique to examine iron products, Mössbauer spectroscopy was utilized to characterize mackinawite and its oxidation products in addition to XRD and XAS. Mössbauer spectroscopy has been widely used to investigate Fe oxidation states, as well as structural and magnetic properties of Fe oxides. However, its application to the characterization of mackinawite and other iron sulfide minerals has been sparse. A general consensus on mackinawite Mössbauer spectral features is lacking in the literature, likely due

to the artifacts associated with the sample preparation and handling (Morice et al., 1969; Vaughan and Ridout, 1971; Mullet et al., 2002). In this study, selected Fe samples were shipped to Pacific Northwest National Laboratory (PNNL) after freeze drying. The prepared Mössbauer disks were stored in anoxic chamber until analysis using a WissEl Elektronik (Germany) instrument. Spectra were obtained at various temperatures, from room temperature to 77 K, and occasional spectra at liquid He (4.5 K). The structural and magnetic properties of Fe were obtained to differentiate Fe components as a function of oxidation time. Details of sample preparation, modeling procedures, and criteria can be found in Chapter 4 and Kukkadapu et al. (2006).

3.4 Properties of Synthetic Materials

In this research, nanocrystalline mackinawite and uraninite were prepared and used as model compounds to investigate the potential of iron sulfide in inhibiting U(IV) solid from oxidation in artificial oxic groundwater. After chemical synthesis, the materials were characterized in terms of mineralogy, surface area, and particle size, which are essential properties of solids that strongly control their chemical reactivity in heterogeneous systems.

3.4.1 Mackinawite Characterization

The synthetic nanocrystalline mackinawite was characterized by XRD for phase identification and by TEM for morphology and particle size. Mackinawite was prepared with the same recipe previously studied by Hayes research group and it had similar structural properties to the material used in the past studies (Jeong et al., 2008).

The XRD pattern of the synthetic solid is shown in Figure 3.4, confirming a crystalline phase of mackinawite with no detectable impurities. The diffraction peaks are broad and weak, indicating a poor degree of crystallinity. The crystallite size of mackinawite determined from the full width at half maximum (FWHM) of diffraction peaks ranges from 5.3 nm to 9.4 nm, depending on specific peak being used. This result indicates that the synthetic mackinawite is nanocrystalline with an average crystallite size of ~6 nm. The small crystallite size suggests a large surface area and, potentially, a high reactivity.

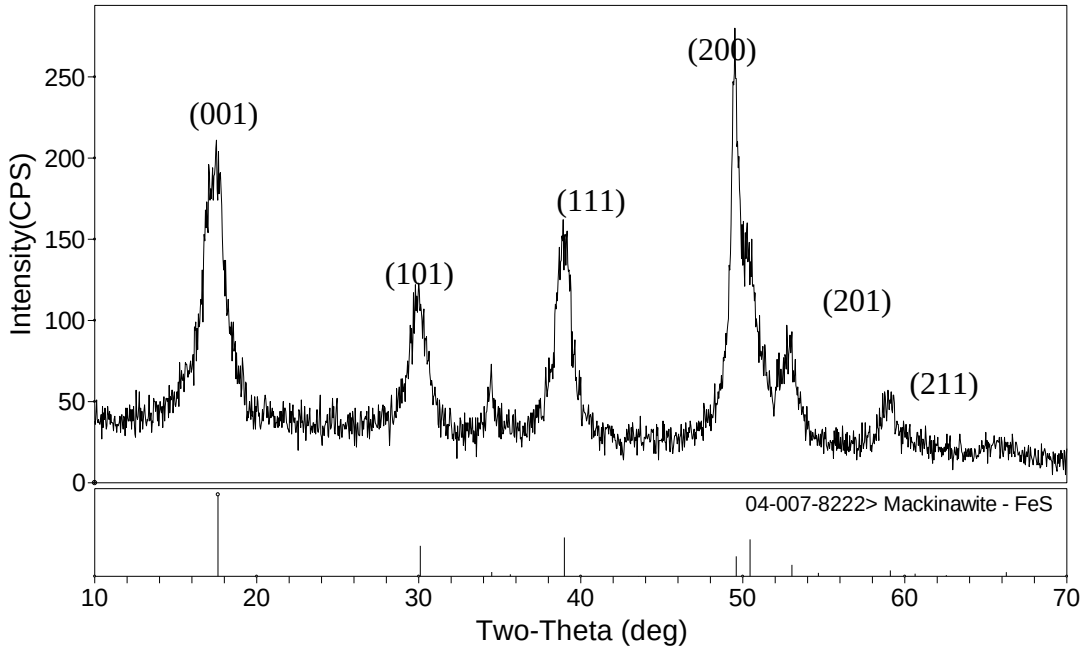

Figure 3.4 XRD pattern of synthetic mackinawite.

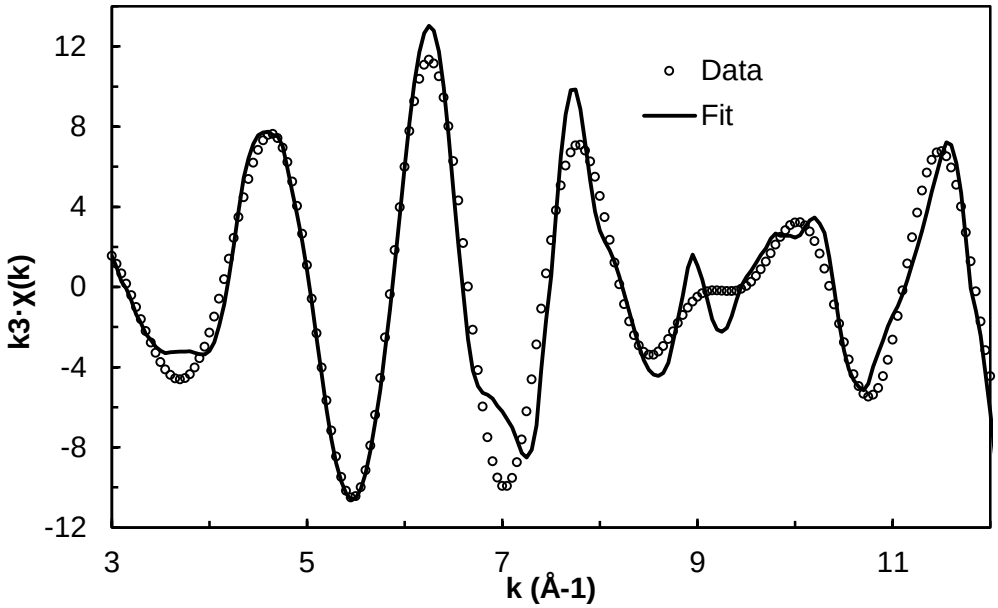

Figure 3.5 Fe K-edge EXAFS data and fit for synthetic mackinawite.

The Fe *K*-edge EXAFS analysis (Figure 3.5) indicates that Fe atoms are coordinated by 3.7 S atoms at the interatomic distance of 2.24(9) Å with ^{2} of 0.0034 and 2.2 Fe atoms at 2.61(5) Å with ^{2} of 0.0029. These structural parameters match reasonably well with previously reported values for mackinawite. For example, Lennie et al. (1995) have reported a coordination number of 4 S atoms with Fe at 2.256 Å from their XRD structure refinement. The Fe-S and Fe-Fe distances are also in good agreement with a previous EXAFS result for synthetic mackinawite of 2.24 Å and 2.60 Å, respectively (Jeong et al., 2008).

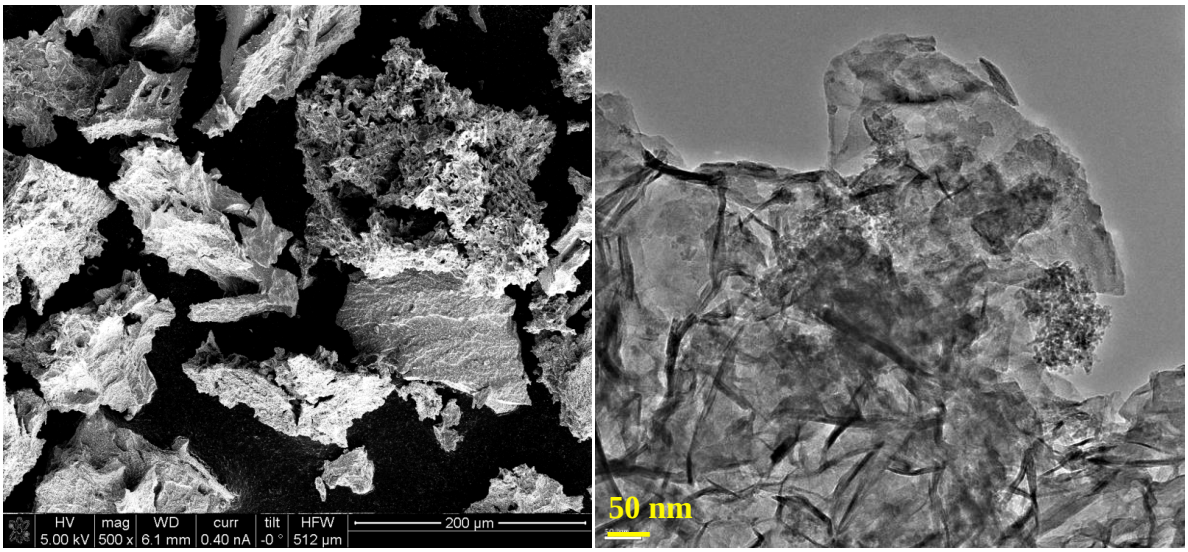

Figure 3.6 SEM (left, courtesy of Dr. Ellis) and TEM (right) images of synthetic mackinawite particles.

Freeze-dried mackinawite particles observed under low magnification SEM are shown to form micrometer-sized irregular aggregates composed of a large number of flake-like nanoparticles (Figure 3.6). In contrast, the TEM image of hydrated mackinawite particles shows that FeS is disordered aggregation of platelets with curvatures and irregular boundaries, similar to results of Ohfuji and Rickard (2006). The results are consistent with its tetragonal layered structure of stacked (001) planes. The layers within the nanostructure revealed by TEM impart mackinawite particles with additional interlayer surface area.

3.4.2 Uraninite Characterization

The synthetic uraninite solids were characterized by XRD, TEM, and XAS to determine their mineral phase, morphology, particle size, and local coordination environment. The synthetic UO_2 solids were brown or blackish brown powders with a face-centered cubic lattice (Figure 3.7). The XRD pattern of uraninite is shown in Figure 3.8, which was used to derive the average crystallite size of ~4 nm. Using the crystallite

dimension of the nanocrystalline uraninite, the specific surface area (SSA) was estimated to be ~170 m^2/g at a density of 8.7 g/cm^3.

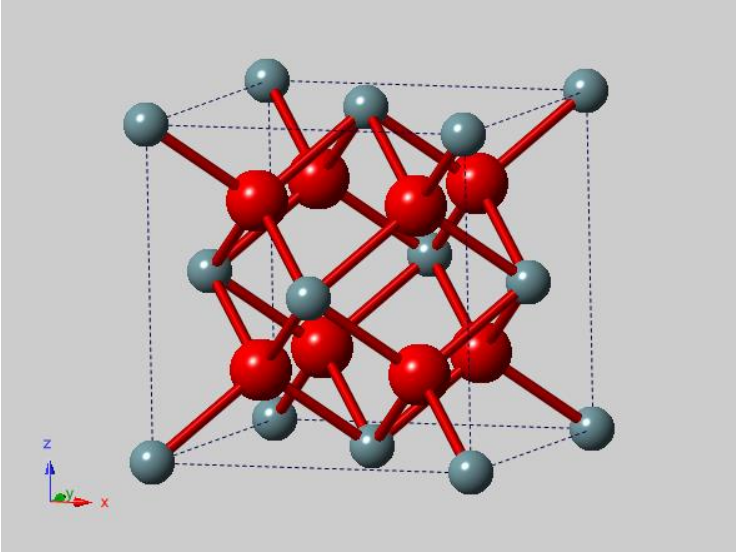

Figure 3.7 Crystal structure of crystalline uraninite. Red: uranium atom, blue: oxygen atom.

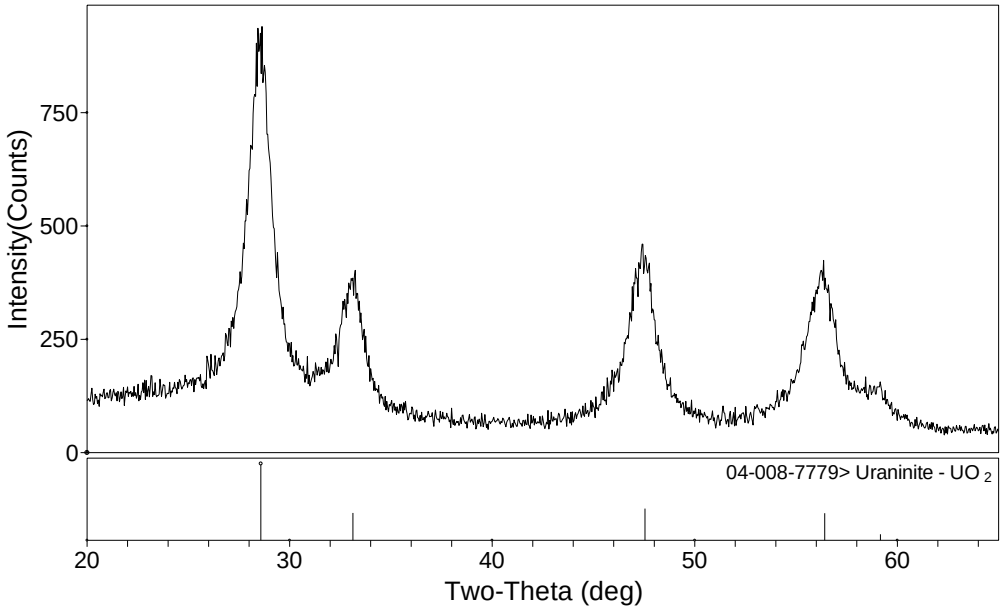

Figure 3.8 X-ray diffraction pattern of synthetic UO_2 precipitates.

TEM images (Figure 3.9) show loose, porous, nano-particulate U(IV) precipitates. Particles have diagonal lengths ranging from ~5 to ~ 20 nm, similar to the U(IV) precipitates synthesized by Beyenal et al (2004) using the same procedure. The SSA estimates based on TEM images range from ~50 to ~140 m^2/g, smaller than those based on XRD. The SSA was not measured by multipoint N_2-BET because BET analysis requires drying the UO_2 solids which could result in particle aggregation and a decrease in surface area. Due to the wide range of SSA estimates for nano-scale synthetic UO_2 by the various approaches, the dissolution rates in this dissertation were normalized by an estimated surface area of 80 m^2/g.

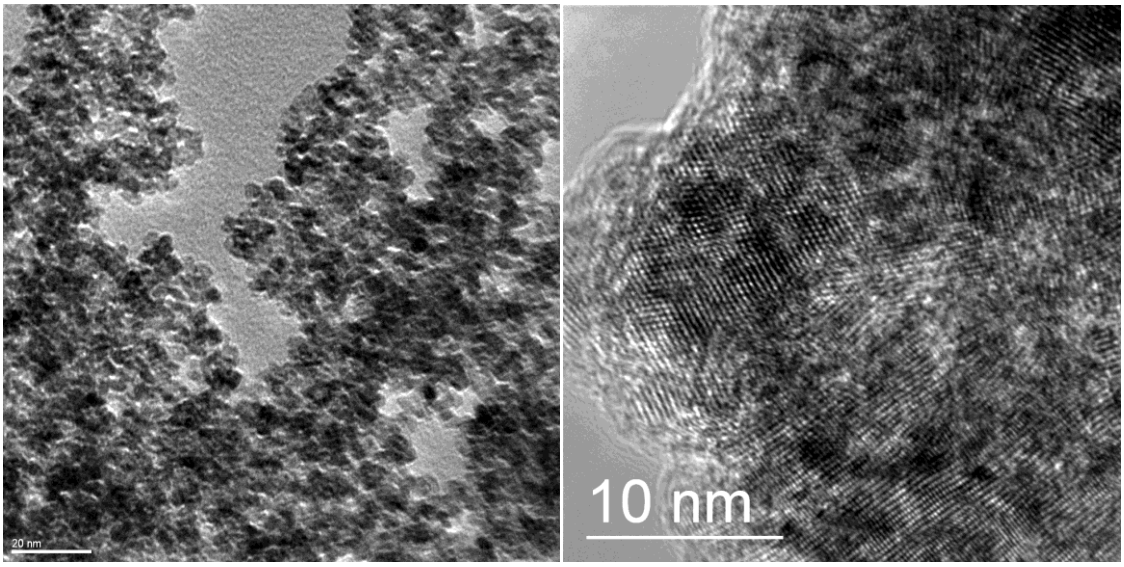

Figure 3.9 TEM images of synthetic UO_2 precipitates. (a) BF image of uraninite nanoparticles (small, dark particles); (b) HREM lattice fringe image of the same material.

EXAFS analyses on synthetic UO_2 (Figure 3.10) indicated that the first shell of atoms surrounding the central U atom consisted of 6.2 O atoms at the interatomic distance of 2.26 Å, and a second shell of 3.6 U neighbors at 3.83 Å. The results are summarized in Table 3.1. The low second-shell coordination number relative to a model uraninite (12 U(IV) neighbors)

suggests that the synthetic uraninite is a poorly-crystalline, nano-scale precipitate with structural defects. The structural parameters of synthetic UO_2 are in agreement with low temperature abiotic (Hyun et al., 2012) and biogenic uraninite (Singer et al., 2009; Veeramani et al., 2009).

In addition, XAS data of a uranyl nitrate solution were also collected and used as a U(VI) reference standard. The central uranium atom in the uranyl solution indicated 2.0 axial O atoms at 1.76(3) Å and 5.8 equatorial O atoms at 2.42(9) Å (Table 3.1). These values are consistent with values reported for U(VI) solutions (Bargar et al., 2000).

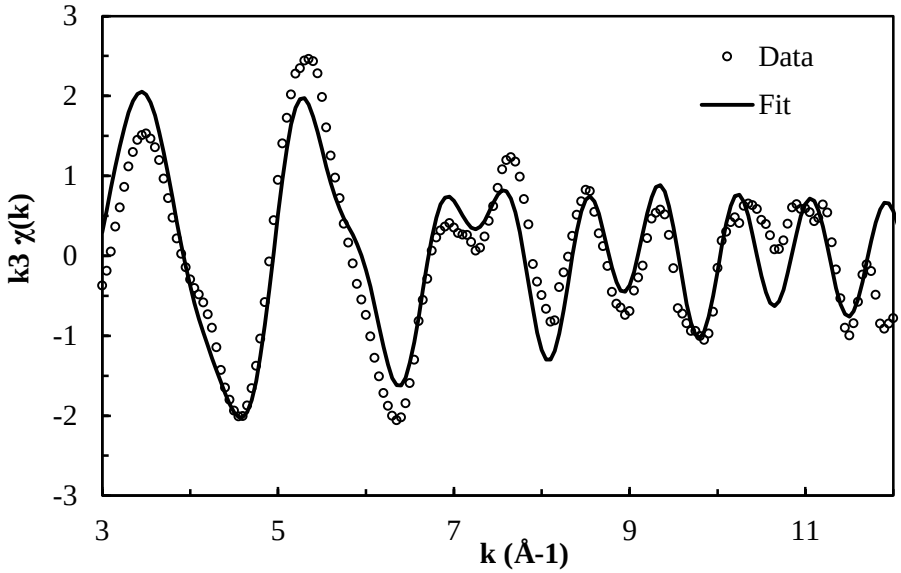

Figure 3.10 U L_{III}-edge EXAFS spectra and fit of synthetic uraninite used in batch studies. The open circles are data; solid line is the fit.

While XRD and EXAFS confirmed the structure of nano-sized uraninite, XANES and XPS spectra indicate a minor presence of U(VI) impurities associated with the reduced uranium particles. Linear combination fitting of the spectra (Table 3.2) shows that ~28% of total uranium is U(VI). The U(VI) component in synthetic uraninite agrees with XPS analysis (Figure 3.11), which indicates that the uraninite surface is comprised of ~20% of U(VI)

(Table 3.2). Assuming that U(VI) species are only present on the surface of uraninite particles and the average particle size is ~6 nm, the estimated thickness of the U(VI) surface coating is ~0.2 nm. This oxidized (passivated) surface layer may play an important role in controlling the rate of UO_2 oxidation by dissolved oxygen.

Table 3.1 Structural parameters extracted from EXAFS analysis. (*CN*: coordination number, *R*: interatomic distance, σ^2: Debye-Waller factor).

Sample	**Edge**	**Path**	***CN***	***R*(Å)**	**σ^2**
Uraninite precipitate	U L_3 edge	U(IV)-O	6.2	2.25(8)	0.0155
U(VI) solution	U L_3 edge	U-O_{ax}	2.0	1.76(3)	0.0023
		U-O_{eq}	5.8	2.42(9)	0.0099

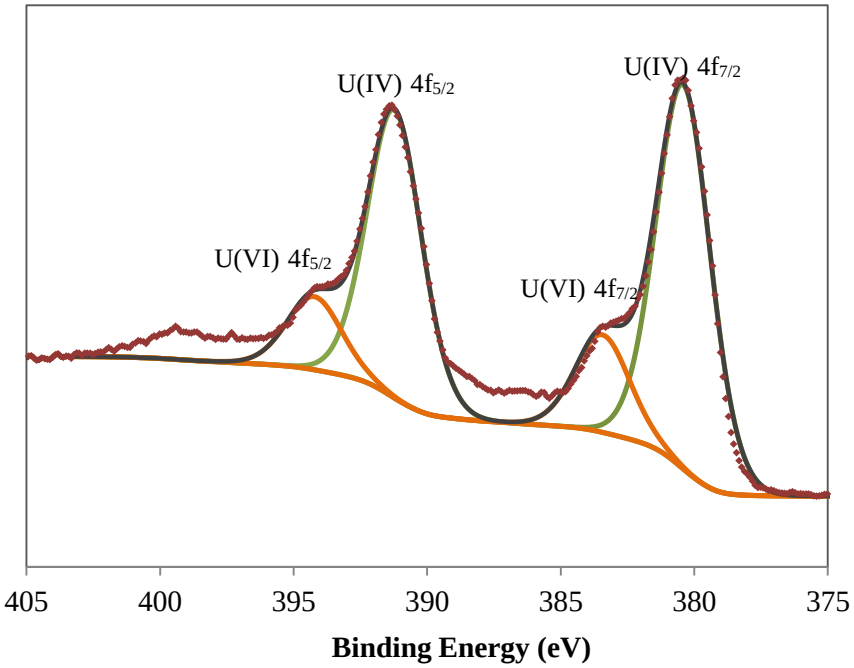

Figure 3.11 U 4f XPS spectra for synthetic UO_2 particles prepared for oxidation experiments. Points are the experimental data and black solid line is the sum of fit. Orange and green lines are the results of quantitative Gaussian-Lorentzian curve fitting showing individual contributions from components.

Table 3.2 Determination of U oxidation state in synthetic uraninite by XANES LCF and XPS analyses. Error is provided in parenthesis.

Element	Oxidation State	XANES	XPS
Uranium	*U(IV)*	72 (2)	80 (5)
	U(VI)	28 (2)	20 (5)

Chapter 4

Oxidative Dissolution of UO_2 in a Simulated Groundwater Containing Synthetic Nanocrystalline Mackinawite

4.1 Introduction

The environmental risks posed by low-level U contamination are mainly associated with the degree of its mobility, which strongly depends on redox conditions and solid-phase U solubility. Under oxic conditions, U(VI) is soluble and forms stable complexes with carbonate and calcium in groundwater, increasing U solubility by several orders of magnitude and thus enhancing its mobility (Guillaumont et al., 2003; Dong and Brooks, 2006; Stewart et al., 2010). In contrast, reduced U(IV) species are often immobilized by biotic or abiotic redox processes as sparingly soluble U(IV) solid phases such as uraninite (UO_2) (Langmuir, 1978). Recent studies further suggest that monomeric U(IV) species may form during microbial U(VI) reduction in association with phosphate or carbonate as sorbed complexes on soils and sediments (Bernier-Latmani et al., 2010; Fletcher et al., 2010; Boyanov et al., 2011), before converting to more stable U(IV) precipitates.

This chapter is adapted from: Bi, Y., Hyun, S. P., Kukkadapu, R. K., and Hayes, K. F., *Geochimica et Cosmochimica Acta.* **2013**, 102, 175-190.

Given that UO_2 is highly insoluble in reducing, low-temperature geological and sedimentary environments (Finch and Ewing, 1992; Ulrich et al., 2008), the reduction of mobile U(VI) to UO_2 by sulfate reducing bacteria (SRB) has been under consideration as a strategy for uranium groundwater remediation. *In situ* biostimulation to reduce U(VI) to UO_2 has been conducted for more than a decade and has been proven to be effective (Senko et al., 2002; Istok et al., 2004; N'Guessan et al., 2008). Recent work further indicates that non-uraninite U(IV) forms, (i.e., monomeric U(IV) species), may also be produced after biotic reductive immobilization and influence the U mobility in the subsurface (Bernier-Latmani et al., 2010; Sharp et al., 2011). However, when subjected to oxidants such as oxygen, reoxidation of the immobilized U(IV) to soluble U(VI) may occur (Zhou and Gu, 2005; Moon et al., 2007; Komlos et al., 2008; Moon et al., 2009). Therefore maintaining reducing conditions or generating an abundant supply of reduced solids, such as $FeS_{0.9}$ (mackinawite; hereafter referred as FeS), for redox buffering and oxidant scavenging during post-stimulation periods may be needed for long-term *in situ* stabilization of U.

Aqueous sulfide and sulfide minerals formed under sulfate reducing conditions were shown to maintain a low redox potential in groundwater and abiotically promote the reduction of U(VI) to UO_2 (Wersin et al., 1994; Suzuki et al., 2005; Hua et al., 2006). FeS has been recognized as an important ingredient and source of sulfide in many toxic metal remediation systems including U bioremediation, although its role has not been fully understood (Abdelouas et al., 1999a; Coles et al., 2000). When exposed to oxygen, FeS undergoes oxidation-induced transformation with a reaction half-time ranging from minutes to a few hours (Burton et al., 2009; Jeong et al., 2010a). The iron solid-phase end products of FeS oxidation, usually goethite and lepidocrocite (Jeong et al., 2010a), may further impact

the reoxidation rates of UO_2 (Sani et al., 2005; Ginder-Vogel et al., 2006; Nico et al., 2009; Spycher et al., 2011a). In addition, oxidized U(VI) may be incorporated into the goethite structure through phase transformation under anoxic conditions as indicated by Nico et al. (2009) and Boland et al. (2011). Structurally incorporated U(VI) could be more stable and resistant to oxidants such as oxygen (Stewart et al., 2009), providing a possible long-term sink for U and strategy for U remediation. It is unclear, however, whether the incorporation of U(VI) into iron oxides occurs in oxic groundwater.

Relatively few studies have investigated the reactions of UO_2 with FeS or the protective nature of FeS in inhibiting UO_2 oxidation. The abiotic mechanism of U(IV) oxidation is also not well understood and often difficult to isolate in field or column studies where microorganisms are active and biogenic oxidants are prevalent. The observed inhibition of UO_2 reoxidation by biogenic FeS in sediments (Abdelouas et al., 1999a; Moon et al., 2009) may actually be the combined effects of abiotic and biotic activities. Past column studies were not performed to specifically test the endurance of FeS protection of UO_2 against oxygen intrusion, in which all FeS was reacted to exhaustion (Abdelouas et al., 1999b). Additional work is needed to establish the role of abiotic reoxidation processes of UO_2 when sulfate reducing conditions are succeeded by oxic conditions.

The objective of the study presented in this chapter was to investigate the oxidative dissolution of synthetic UO_2 by dissolved oxygen in absence and presence of FeS under abiotic simulated groundwater conditions. Dissolution rates of UO_2 are presented and compared to previous studies. Possible aqueous species and surface reactions supported by analytical and spectroscopic results are discussed for elucidating the influence of FeS on UO_2 oxidation by oxygen.

4.2 Experimental Methods

4.2.1 Oxidative Dissolution Experiments

For the oxidation experiments, 1 L of an artificial groundwater solution containing 4.0 mM $NaHCO_3$, 0.4 mM KCl, and 2.0 mM $CaCl_2$ was prepared using deoxygenated water (Table 4.1). Five grams of freeze-dried FeS powder were suspended in an anoxic aliquot of the artificial groundwater solution (~200 mL) and continuously stirred for two days to allow sufficient time for solid phase hydration. The remainder of the solution was transferred to the 1L batch reactor (Figure 3.1) and purged for up to 4 h with a 2% P_{O2}, 5% P_{CO2}, 93% P_{N2} gas mixture before the start of the experiment until stable DO and pH readings were achieved.

Table 4.1 Comparison of groundwater compositions in equilibration with 2% P_{O2}, 5% P_{CO2} gas mixture.

Experimental design	FeS with UO_2 (mM)	Control **UO_2 only** (mM)	Control **FeS only** (mM)	Equilibrium concentration for all three experiments
Na^+	4.0	4.0	4.0	4.0
HCO_3^-	4	9	4	11.3 (as DIC)*
Cl^-	4.4	4.4	4.4	4.4
Ca^{2+}	2.0	2.0	2.0	2.0
K^+	0.4	0.4	0.4	0.4

* Total dissolved inorganic carbonate (DIC) concentration calculated from Visual MINTEQ at equilibrium with 0.02 atm O_2 and 0.05 atm CO_2 gas.

The oxidation experiment was initiated upon the addition of FeS and UO_2 suspensions to the reactor. The suspensions were transferred from the anaerobic chamber with limited exposure time to air (< 30 s). This operation assumed immediate and complete mixing of the suspension in the reactor under vigorous stirring. The final suspension was

slightly more than 1 L due to the addition of a small volume of UO_2 suspension (~15 mL). The resulting concentration was ~5.0 g/L and ~0.4 g/L of FeS and UO_2, respectively. The solid phase UO_2 concentration was determined by total digestion with concentrated nitric acid. Over the duration of the oxidation experiment, the system was continuously purged with the 2% P_{O2}, 5% P_{CO2}, 93% N_2 gas mixture at a flow rate of 0.1 L/min to maintain a pH of ~7 in the suspension and a constant headspace composition. The pH, DO, and Eh of the suspension were measured *in situ* by calibrated probes located on the ports of the lid, which remained in the solution over the entire reaction period.

Aliquots of suspension were periodically withdrawn through the sampling port using a 15 mL polypropylene syringe, and then immediately transferred to the anaerobic chamber. Subsamples of ~2mL of suspension (solid plus aqueous phase) were used for an elemental sulfur extraction analysis as described below. The remaining sample (~13 mL) was centrifuged and filtered through 0.1 μm syringe filters (Millipore). A remainder of the filtrate was used for IC analysis of $S_2O_3^{2-}$ and SO_4^{2-}. The remainder of the filtrate was acidified in ~1% nitric acid and stored in a refrigerator (4 ℃) until used for metal analyses with ICP-MS. Solid materials settled by centrifugation were transferred to a crimp-sealed vial and stored in an anaerobic chamber until characterized. A total of 14 sets of samples at different time points were obtained over the course of the experiment until the total dissolved uranium concentration reached steady state. The end solid phase products were rinsed using 30 mM $NaHCO_3$ solution to extract surface-adsorbed U(VI). The batch experiments were performed in duplicate.

Control experiments with either FeS or UO_2 as a single phase in suspension were also conducted in duplicate following the same procedures as described above. In the batch

experiment with FeS alone, the concentration was 5 g/L, while the experiment with only UO_2 the concentration was 0.42 g/L. In the UO_2 control experiments, the artificial groundwater was prepared with 9.0 mM $NaHCO_3$, 0.4 mM KCl, and 2.0 mM $CaCl_2$ to achieve a pH = 7. A slight variation in UO_2 solid concentration existed for batch experiments involving U oxidative dissolution from the variation in the amount of UO_2 delivered in 15 mL of a stock suspension (Table 4.2).

4.2.2 Analyses

Total dissolved iron, uranium, and calcium were determined by ICP-MS. Dissolved Fe(II) in the filtrate was determined photometrically by the ferrozine method (Stookey, 1970). Total dissolved iron was verified using the ferrozine method (Viollier et al., 2000) and compared with the total concentration measured by ICP-MS. Briefly, Fe(III) in the solution is reduced to Fe(II) by hydroxylamine under acidic pH and then measured by a spectrophotometer at 562 nm in the presence of ferrozine. Aqueous $S_2O_3^{2-}$ and SO_4^{2-} were analyzed by IC (Dionex DX-100). Elemental sulfur in the solid phase was analyzed by liquid chromatography (Agilent 1090) with an eluent of 95%:5% methanol: water (McGuire and Hamers, 2000).

Solid samples collected from batch experiments were analyzed by XRD, XAS, and Mössbauer spectroscopy. XAS data collection was carried out at Stanford Synchrotron Radiation Lightsource (SSRL) following the procedure described in Chapter 3. XAS data were subjected to X-ray absorption near edge structure (XANES) and extended X-ray absorption fine structure (EXAFS) analyses after energy calibration and data average. EXAFS spectra were extracted and k^3-weighted from averaged data files after background

subtraction and spline fitting using SixPACK and IFEFFIT code (Newville, 2001; Webb, 2005). Backscattering phase and amplitude functions for EXAFS fitting were obtained using FEFF 8 code with crystallographic input files generated by ATOMS (Rehr et al., 1992). To obtain the optimal structural parameters, including coordination numbers (*CN*s) and interatomic distances (*R*), the Debye-Waller factor (^{2}) and energy reference E_0 parameters were allowed to float during the fitting. The many-body factor S_0^2 was fixed at 0.9 to reduce the number of fitting parameters. For U modeling, a uranyl(VI) nitrate solution and synthetic UO_2 solid sample were used as U(VI) and U(IV) reference standards, respectively. Accuracies of interatomic distances and *CN*s were estimated to be ±0.02 Å and ±20%, respectively. Linear combination fitting (LCF) of S XANES spectra was conducted using synthetic mackinawite and AR-grade S_8^0 as standards for S(-II) and S(0), respectively. To address S_8^0 particle-size effect on XANES absorbance in fluorescence mode (Pickering et al., 2001), both finely ground (~1–10 μm) and dissolved (1% w/v in toluene) S_8^0 were used as S(0) model compounds (Burton et al., 2009). The uncertainty of the LCF is generally about 10% for sulfur XANES spectra (Prietzel et al., 2011).

Mössbauer spectra of powder samples were collected using either a WissEl Elektronik (Germany) or Web Research Company (St. Paul, MN) instruments that included a closed-cycle cryostat SHI-850 (Janis Research Company, Inc), a Sumitomo CKW-21 He compressor unit, and an Ar-Kr proportional counter detector with WissEl setup or a Ritverc (St. Petersburg, Russia) NaI detection system. A 57Co/Rh source (50-mCi to 75-mCi, initial strength) was used as the gamma energy source. With the WissEl setups, the transmitted counts were stored in a multichannel scalar (MCS) as a function of energy (transducer velocity) using a 1024-channel analyzer. The setups data were folded to 512 channels to

provide a flat background and a zero-velocity position corresponding to the center shift (CS) of a metal Fe foil at room temperature (RT). Calibration spectra were obtained with a 25-μm-thick Fe foil (Amersham, England) placed in the same position as the samples to minimize any geometry errors. The Mössbauer data were modeled with Recoil software (University of Ottawa, Canada) using a Voigt-based structural fitting routine (Rancourt and Ping, 1991). The coefficient of the variation of the spectral areas from individual sites generally ranged between 1% and 2% of the fitted values. Details of sample preparation and modeling procedures and criteria are reported in Kukkadapu et al. (2006).

4.2.3 UO_2 Dissolution Rate Calculation

UO_2 oxidative dissolution occurred in the presence and absence of 5 g/L FeS. In these experiments, once oxidative dissolution began, $[U]_{diss}$ initially increased linearly but then reached a plateau at longer times. Dissolution rates for UO_2 were obtained by subjecting the initial linear portion of the plots to regression analysis. For the rate analysis, typically more than four points were utilized, resulting in R^2 values greater than 0.98 for all least-square fits. Regression analysis also yielded 95% confidence intervals for error estimates. The dissolution rates normalized to mass (r_m) and surface area (r_n) are compared to results of previous oxidation studies performed under similar conditions in Table 4.1.

Table 4.2 Comparisons of UO_2 oxidative dissolution rates obtained from batch experiments in 1 L CMBR under different experimental conditions. U dissolution rates are based on mass (r_m) and surface area (r_n) of UO_2 solids.

Design	[UO_2]		Reactor Design	[FeS] g/L	P_{O2} Bar	[DIC] mM	pH	r_m ($\times 10^9$) mol g^{-1} s^{-1}	r_n ($\times 10^{10}$) mol m^{-2} s^{-1}
	g/L	mmol/L							
This work, moderately oxidizing conditions.									
Syn-UO_2	0.42	1.56	Batch	\	0.02	~10*	7.01	5.4 ± 0.2	1.08 §
Syn-UO_2	0.45	1.67	Batch	\	0.02	~10*	6.71	5.0 ± 0.4	1.0 §
Syn-UO_2 w/ FeS	0.47	1.74	Batch	5.0	0.02	~10*	6.98	12 ± 4	2.4 §
Syn-UO_2 w/ FeS	0.49	1.80	Batch	5.0	0.02	~10*	6.97	13 ± 5	2.6 §
Published data, similar moderately oxidizing conditions.									
Syn-UO_2[a]	0.79	2.9	Flow-through	\	0.01	1	8.0	3.94	6.62
Syn-UO_2[a]	1.14	4.2	Flow-through	\	0.01	10	8.7	1.50	2.50
Bio-UO_2[a]	1.59	5.9	Flow-through	\	0.01	1	8.5	4.67	0.93
UO_2 (cr)[b]	7.8	29	Batch	\	0.2	100	8.0	20 ± 2	170

* calculated using Visual MINTEQ at equilibrium with 0.05 atm CO_2 gas.

§ calculated by using an estimated surface area of 50 m^2/g for the synthetic nanocrystalline UO_2.

References: [a.] Ulrich et al, (2009). [b.] Pierce et al. (2005).

4.3 Results and Discussion

4.3.1 Oxidative UO_2 Dissolution

4.3.1.1 Dissolution of UO_2 at pH 7

To study the effects of FeS on the oxidative dissolution of synthetic UO_2, total dissolved U (U_{diss}) and Fe (Fe_{diss}) were monitored as a function of time in the artificial groundwater in equilibrium with the gas mixture (2% P_{O2}, 5% P_{CO2}, and 93% P_{N2}) at pH = 7 in the presence of FeS (Figure 4.1). Duplicate profiles were similar in the trend of dissolved U, both showing a lag phase of U dissolution for approximately 50 to 60 hr. U_{diss} remained below 0.05 mM during the lag phase, before an abrupt increase of U_{diss} occurred. From ~55 to ~92 hour, U_{diss} increased almost linearly at a rate of 1.2 – 1.3 mol g^{-1} s^{-1} (Table 4.2). The initial rate analysis showed good agreement with rates evaluated from previous studies on UO_2 dissolution (Ulrich et al., 2009), despite the different pH conditions (pH 7 vs. 8.0–8.8) and reactor configuration (batch vs. flow-through reactor) (Table 4.2). As $[U]_{diss}$ leveled off near 160 hr, it reached a plateau concentration at ~1.0 mM (~63% of the initially added UO_2), indicating that <40% of added U remained in association with solid phases. Figure 4.1 also shows the profiles of total dissolved Fe in comparison to U_{diss} over ~180 hr reaction. During the lag phase of UO_2 dissolution, dissolved Fe remained as Fe(II) in the reactor. The sharp spike of Fe_{diss} observed at ~4 hr was accompanied by the very low level of $[U_{diss}]$ (Figure 4.1b). As Fe_{diss} dropped below 0.03 mM after ~10 hr, U_{diss} increased to a higher level of ≤0.06 mM for additional ~40 hr. As soon as dissolved Fe(II) became undetectable in the suspension, U_{diss} started to increase as a result of UO_2 oxidative dissolution.

To illustrate the difference in UO_2 dissolution in the presence and absence of FeS, the results of control experiments are plotted together with an U_{diss} profile in Figure 4.1. Figure

4.2 shows that U_{diss} increased linearly at the initial reaction stage without delay in the control and remained higher than the experiment with FeS until ~60 hr reaction. Using the initial linear portion of the dissolution profile, the mass-normalized dissolution rate for UO_2 in this study, was 5.0 – 5.4 mol g^{-1} s^{-1} (Table 4.2). The rate is comparable to those reported by Ulrich et al. (2009) for synthetic and biogenic UO_2 oxidation by dissolved oxygen, but is lower by a factor of two compared to experiments in the presence of FeS. U_{diss} concentration reached a plateau of ~0.80 mM after 200 hr, accounting for approximately 50% of the total uranium input. The final steady-state U_{diss} achieved a lower concentration in the control. In contrast to the experiments with FeS, a more significant portion of the U remained in solid phase after 200 hr reaction in the control.

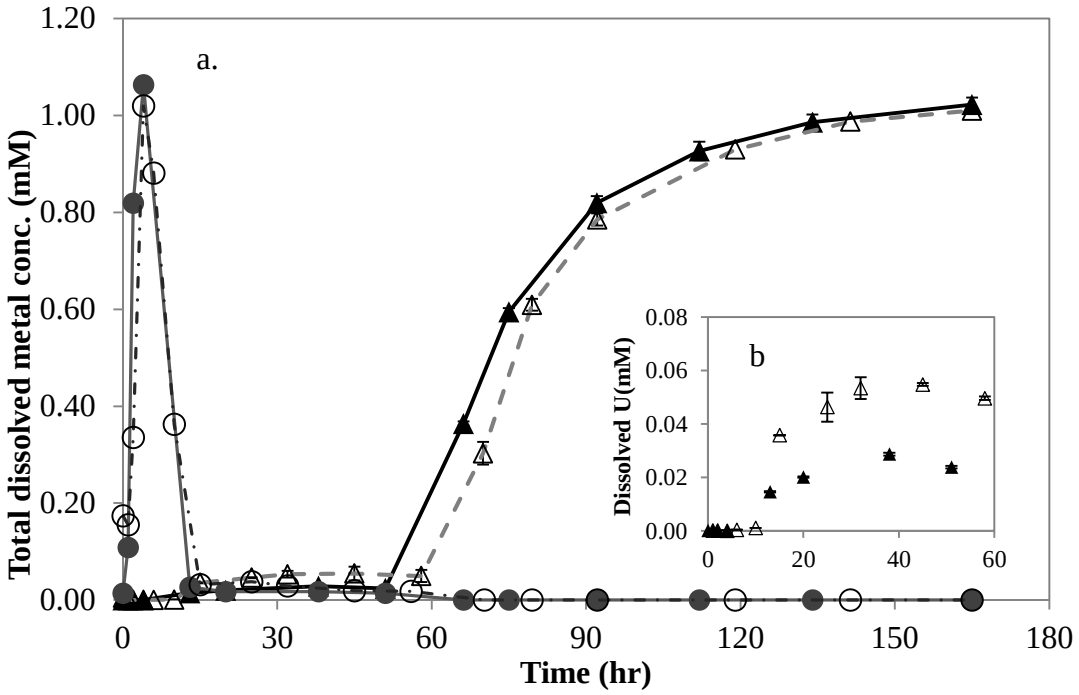

Figure 4.1 The kinetic profiles of (a) total dissolved U (▲) and Fe (●) as a function f time during UO_2 oxidative dissolution in the presence of FeS under a pH = 7 groundwater condition equilibrated with 2% P_{O2}, 5% P_{CO2} gas mixture. The inset plot (b) shows enlarged plot of U_{diss} for the initial 60 hr of reaction time in the presence of FeS. Replicates are represented by filled and empty markers. Error bars, reflecting one analytical standard deviation of analysis, are sometimes smaller than the symbol size.

The delayed dissolution of UO_2 in the presence of FeS compared to the control is primarily attributed to the low concentration of DO, which stayed at an undetectable level for ~60 hr (Figure 4.2b). The Fe(II) species, including soluble Fe(II) and FeS, may also contribute to the low levels of dissolved U by abiotic reduction of U(VI). Liger et al. (1999) reported abiotic surface-catalyzed U(VI) reduction by soluble Fe(II) in a near-neutral pH range. Reduction of U(VI) solely by soluble Fe(II) was observed by Du et al. (2011) when reactant and product concentrations were in the range for thermodynamically favorable reduction. Because dissolved Fe(II) was as high as ~1.1 mM over the initial ~10 hr, it appears that dissolved and surface-adsorbed Fe(II) prevented the oxidation of UO_2. Any oxidized U(VI) species would have likely been recycled back to the reduced form of U(IV) in the suspension over the first 10 hr. In addition, solid phase Fe(II) (i.e., FeS) can delay UO_2 oxidation by reducing aqueous U(VI) to U(IV) and producing elemental sulfur and ferric iron (Hua and Deng, 2008; Hyun et al., 2012).

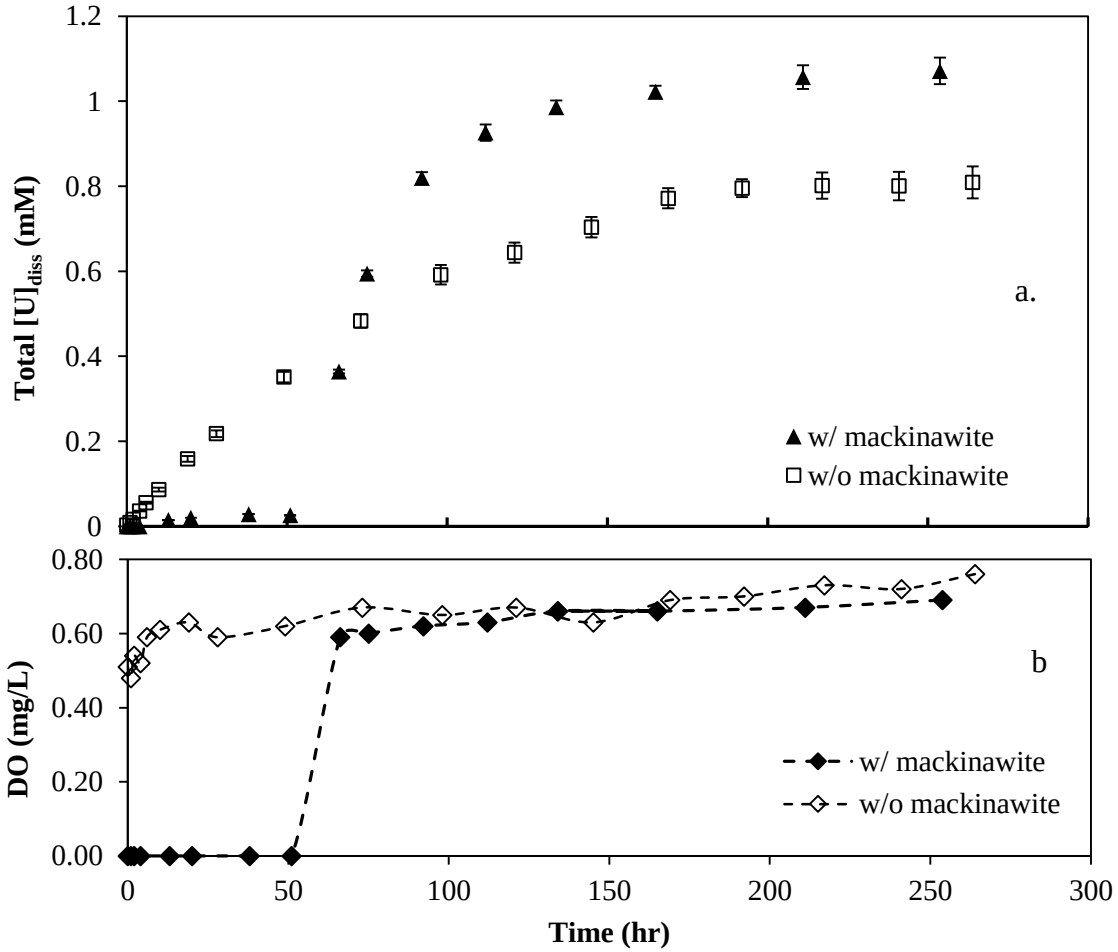

Figure 4.2 Comparison of kinetic profiles of (a) total dissolved U; and (b) DO in the presence (*filled markers*) and absence (*empty markers*) of FeS over the course of the oxidation experiment. Error bars reflecting one analytical standard deviation of analysis are sometimes smaller than the symbol size.

As the oxidation reaction proceeded, the dissolved Fe(II) decreased to a level of ~0.03 mM between 10–60 hr, while the dissolved U increased to submillimolar levels. U_{diss} remained relatively constant, accounting for less than 5% total U in the system. During this time frame, UO_2 solids underwent moderate oxidative dissolution with U_{diss} considerably higher than the UO_2 solubility at pH = 7 under anaerobic conditions (Casas et al., 1998; Guillaumont et al., 2003; Bargar et al., 2008; Spycher et al., 2011b). The consumption of Fe(II) species by dissolved oxygen resulted in less Fe(II) reducing capacity for converting

oxidized U(VI) to U(IV). However, as long as FeS was present, significant oxidative dissolution of UO_2 did not occur.

Beyond the lag phase, rapid UO_2 dissolution was associated with the substantial increase in DO levels (Figure 4.2b) due to the depletion of FeS, as noted in the change in XRD patterns over time (Figure 4.3). After $[U]_{diss}$ reached a plateau in the batch system, the extraction of surface-adsorbed U(VI) from the solid products by 30 mM bicarbonate solution recovered additional ~0.4 mM U (~25 % of total U). At the end of the experiment with FeS, most UO_2 was oxidized to U(VI) as soluble U(VI) species. Thermodynamic calculations by Visual MINTEQ (detailed in Appendix B) indicated that the dominant aqueous U(VI) species were $Ca_2UO_2(CO_3)_3$ (aq) and $CaUO_2(CO_3)_2^{2-}$ ternary complexes, which represented ~90% of soluble U(VI) (Figure 4.4). The U(VI) solution was under-saturated with respect to any known U(VI) solid phases, including schoepite ($UO_3{\cdot}2H_2O$), rutherfordine (UO_2CO_3), UO_3(s), $UO_2(OH)_2$(s) and becquerelite ($Ca(UO_2)_6O_4(OH)_6{\cdot}8(H_2O)$). The remaining non-dissolved U was speculated to be either U(VI) incorporated into FeS oxidation products or partially oxidized U(IV) solid phase. To address these possibilities, the solid-associated U form was characterized by XAS as discussed in section 4.3.1.2.

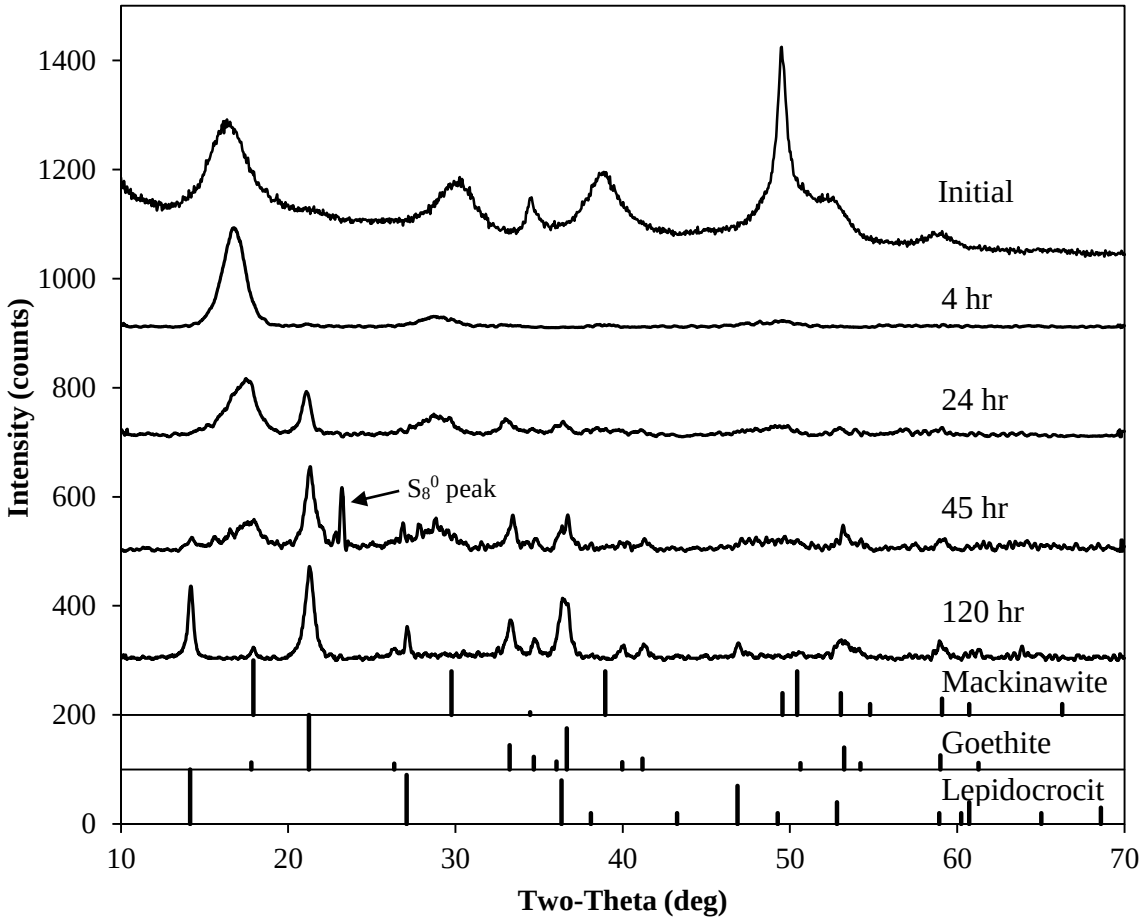

Figure 4.3 Diffraction patterns of oxidized samples in the batch system. Oxidation times are indicated adjacent to the diffractograms.

In the case of the control, an additional ~0.2 mM U(VI) (10% of total U) was extracted using a 30 mM bicarbonate solution at steady-state. Approximately 40% of total U still remained in the solid form, notably higher than the residual solid U in the experiment with FeS present. The XRD pattern of the sample collected at ~ 200 hr revealed the presence of a U(IV) oxide phase (Figure 4.5). Given the nearly identical XRD patterns of $UO_{2.00}$ and partially oxidized U(IV) oxides (i.e., U_3O_7, U_4O_9), it is difficult to confirm the exact phase of UO_2 oxidation product by XRD alone. Because UO_2 solid was not completely oxidized to U(VI) in the presence of oxygen, a partially oxidized layer with a low solubility likely

protected the UO_2 core from complete dissolution (Torrero et al., 1997; de Pablo et al., 2004; Ulrich et al., 2009). Pierce et al. (2005) showed that UO_2 oxidative dissolution rates decreased as the solution concentration approached equilibrium with a passivation layer in the presence of oxygen, a similar trend observed in the present study. This idea is also supported by the fact that only 10% of the residual was carbonate extractable in the control (where U(IV) is extractable but UO_2 is not). The steady-state dissolved U(VI) concentration thus is thought to be governed by the solubility of partially oxidized U(IV) layer surrounding the UO_2 core.

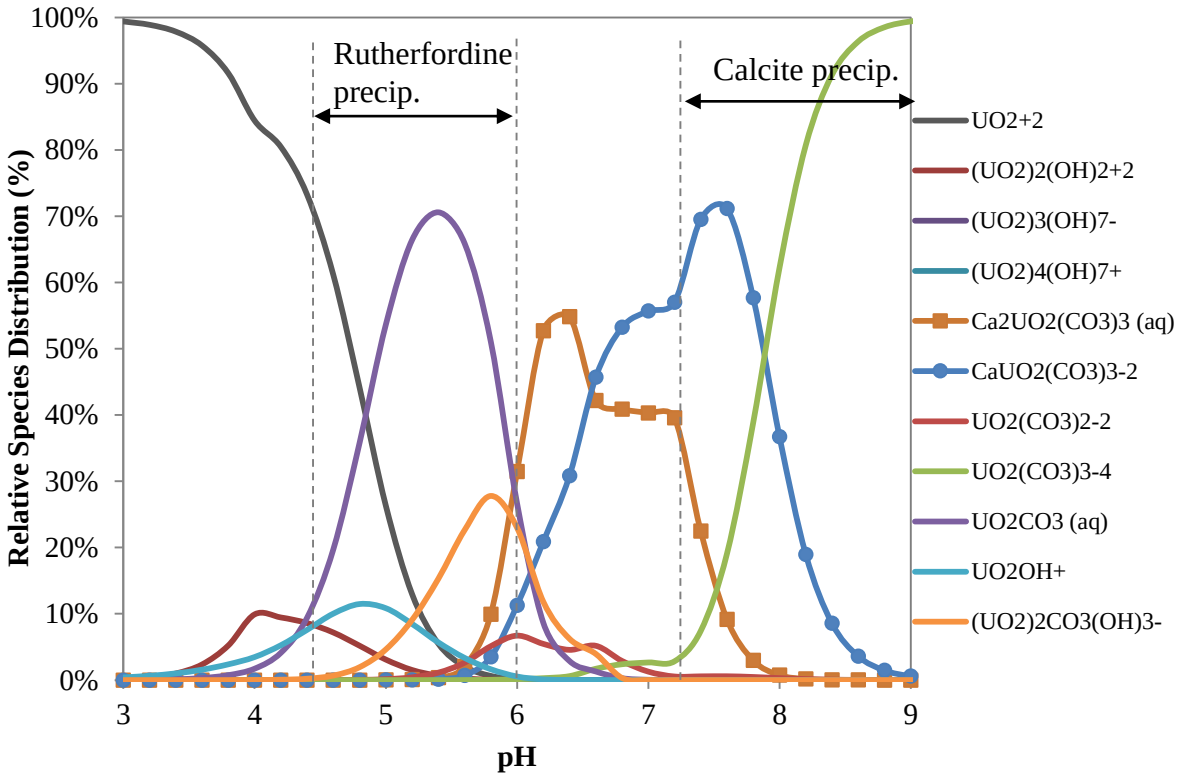

Figure 4.4 Dissolved U(VI) species distribution as a function of pH calculated by Visual MINTEQ. The arrows indicate the pH range where precipitation occurs: rutherfordine (pH = 4.4–6.2) and calcite (pH >7.3). Simulation conditions: 1.1 mM UO_2^{2+}, 4.0 mM $NaHCO_3$, 0.4 mM KCl, and 2.0 mM $CaCl_2$, equilibrated with a 2% P_{O2}, 5% P_{CO2} gas mixture.

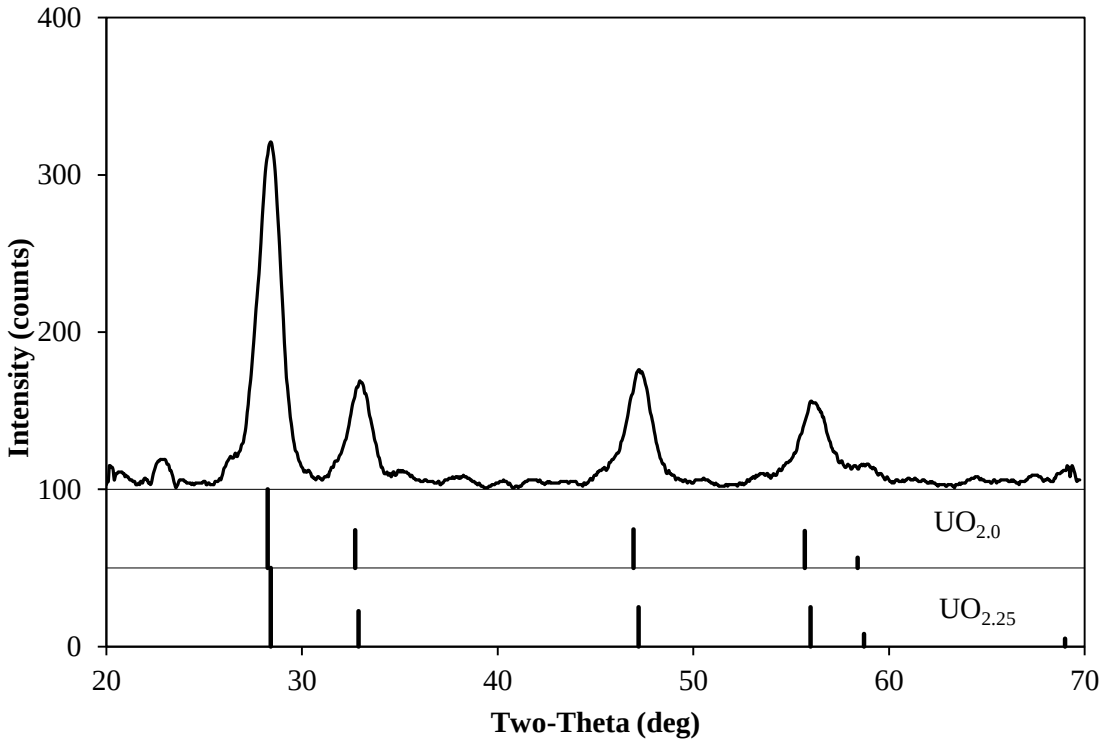

Figure 4.5 X-ray diffraction pattern of residual UO_2 collected at 260 hr reaction of oxidation by oxygen compared to stoichiometric UO_2.

4.3.1.2 X-ray Absorption Spectroscopy Results.

To track the changes in solid phase U speciation during oxidation, U L_{III}-edge XANES and EXAFS spectra of selected oxidized samples were analyzed. The XANES results (Figure 4.6) were used to examine the change of U oxidation state in the bulk material. The 48-hr sample shows a lack of energy shift of absorption edge compared to the 0.1-hr sample, indicating an unchanged oxidation state of U(IV). This result is consistent with the insignificant oxidative dissolution of UO_2 during the lag phase up to ~60 hr. An inspection of the Fourier transformed U L_{III}-edge EXAFS data (Figure 4.7) also shows the unchanged coordination environment of U during this time period. The corresponding structural parameters extracted from the EXAFS data analyses (Table 4.3) resemble those of unreacted UO_2 (Veeramani et al., 2009; Bernier-Latmani et al., 2010), notably a strong first

O shell at 2.34 Å (corresponding to the phase shift at 1.8 Å *R*+ d*R*) and a strong U shell at 3.83 – 3.85 Å (corresponding to phase shift at 3.8 Å *R*+ d*R*) in the 0.1-hr and 48-hr solid samples. The XAS results, along with the macroscopic dissolution data, clearly confirm that DO was preferentially consumed by FeS, delaying UO_2 oxidation during this lag period.

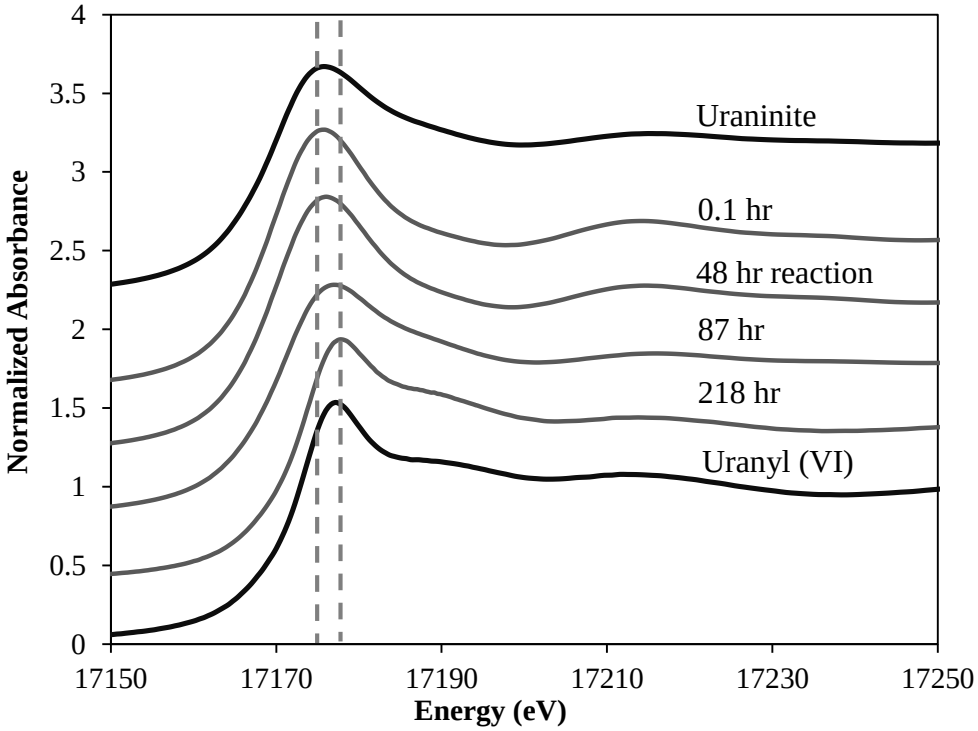

Figure 4.6 Uranium L_{III}-edge XANES spectra of batch samples in the presence of FeS as a function of time. The dotted lines bracket the peak position of U(IV) in uraninite. An energy shift to higher eV indicates the oxidation of U to a higher valence state.

The shift of the U L_{III}-edge to a higher energy occurred (Figure 4.6) when U_{diss} and DO rapidly increased after ~60 hr (Figure 4.2) due to the oxidation of UO_2 by available DO. The XANES spectrum of the solid phase collected at 87 hr is different from the U(IV) or U(VI) standards, suggesting a mixed or an intermediate valance state. Modeling of the Fourier transforms (Table 4.3) shows that U has 2.1 nearest O neighbor atoms at 1.84 Å, the

signature feature of the axial O atoms bound to U(VI) as in uranyl ion (UO_2^{2+}). The presence of axial O suggests that UO_2 oxidation has resulted in oxidized uranyl ions bound to the solid phases. The EXAFS analysis also indicates the presence of solid phase U with structural characteristics of a reduced U(IV) phase, with 9.7 O neighbors at 2.28 Å and 3.0 U neighbors at 3.84 Å. These features are interpreted as arising from the remnant UO_2, suggesting that a UO_2 core remains intact at 87 hr. The Debye-Waller factors for the U^{IV}-O and U^{IV}-U^{IV} bonds in the UO_2 structure obtained from 0.1-hr, 48-hr, and 87-hr samples have a continuously increasing trend with reaction time, consistent with the increased disorder of the O and U backscatterer positions around the central U atom. The increased disorder in the UO_2 structure along with the mixed U structural parameters suggest the formation of a partially oxidized passivation layer during the oxidative dissolution of UO_2. The oxidized surface layer and diminishing UO_2 core relative to the surface layer are also supported by earlier studies on UO_2 oxidation. De Pablo et al. (1996) reported an oxidized surface layer in the form of U_3O_7 in batch experiments at pH 8, while Torrero et al. (1997) reported a surface phase comprised of U_4O_9 using a continuous flow-through reactor at pH 8.2. Ulrich et al. (2009) also indicated a progressive surface layering surrounding both biogenic and synthetic UO_2 as a function of P_{O2}, pH, and dissolved inorganic carbon (DIC).

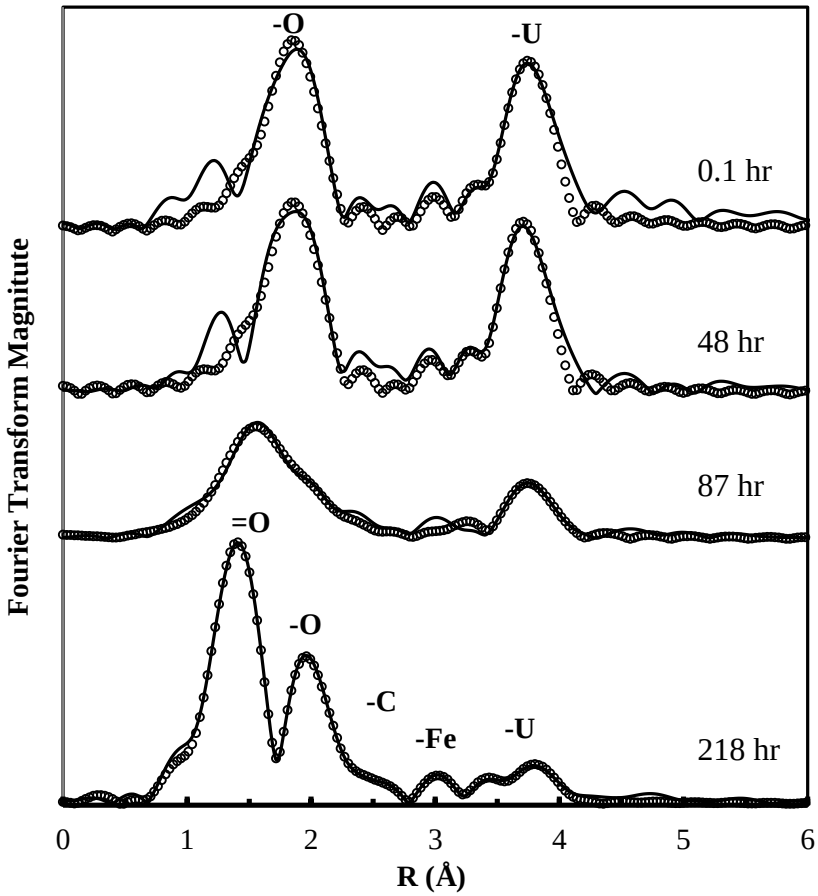

Figure 4.7 Fourier transform magnitudes of U L_{III}-edge EXAFS in the samples over the course of the oxidative dissolution experiment in the presence of FeS (line: data, dots: fits).

At 218 hr, when $[U]_{diss}$ reached steady-state values, the XANES and EXAFS analyses indicated that U in the solid sample was substantially oxidized to U(VI) (Fig. 4.4, 4.5). The Fourier transforms clearly show dissimilar features compared to the samples at early oxidation stages and a lack of U^{IV}-O and U^{IV}-U^{IV} bonds. The central U atom has 2.4 axial O atoms at 1.81 Å, 3.4 equatorial O atoms at 2.45 Å, 0.82 C atoms at 2.96 Å, 1.9 Fe atoms at 3.31 Å, and 1.1 U atoms at 3.93 Å (Table 4.3). These structural parameters derived from the EXAFS modeling support the structural model of surface-adsorbed multinuclear U(VI) carbonato complexes on Fe oxyhydroxides, which are the major solid-associated U phases in the 218-hr sample. This U(VI) surface species is comparable to those reported in previous

studies by Bargar et al. (2000) and Ulrich et al. (2006) for U(VI) sorption on hematite and ferrihydrite, respectively. The presence of the strong backscattering from the axial oxygen atoms characteristic of uranyl ion and the lack of the O shell composed of 6 O atoms at 2.09 Å expected from the U(VI) incorporated into the goethite structure (Nico et al., 2009) exclude the possibility of significant U(VI) incorporation into the octahedral sites of the nanogoethite structure. Thus, U(VI) retention through replacing Fe^{3+} in Fe oxides structure (Nico et al., 2009; Stewart et al., 2009; Boland et al., 2011) is not an apparent route under the current experimental conditions using oxic groundwater. Rather, an adsorption of multinuclear U(VI)-carbonato complexes by nanogoethite or lepidocrocite is the retention mechanism for dissolved U(VI) in the simulated groundwater. In addition, XAS analyses indicate the absence of a U(VI) solid (e.g., rutherfordine) in the 218-hr sample, consistent with thermodynamic calculations by Visual MINTEQ.

Table 4.3 Structural parameters obtained from U L_{III}-edge EXAFS data analysis of solids collected from the batch reactor oxidative dissolution study as a function of time.

	0.1 hr	48 hr	87 hr	218 hr
N_{O1}	6.6 (U^{IV}-O)	6.8 (U^{IV}-O)	2.1 (U^{VI}-O)	2.4 (U-O_{ax})
R_O (Å)	2.34(2)	2.34(1)	1.83(6)	1.81(3)
^2_O	0.0091	0.0096	0.0113	0.0036
N_{O2}			9.7 (U^{IV}-O)	3.4 (U-O_{eq})
R_O (Å)			2.28(3)	2.45(2)
^2_O			0.0295	0.0058
N_C				0.82
R_C (Å)				2.96
^2_C				0.0039
N_{Fe}				1.9
R_{Fe} (Å)				3.31
$^2_{Fe}$				0.0101
N_U	4.7 (U^{IV}-U^{IV})	5.8 (U^{IV}-U^{IV})	3.0 (U^{IV}-U^{IV})	1.1 (U^{IV}-U^{IV})
R_U (Å)	3.85(5)	3.83(2)	3.84(3)	3.93
^2_U	0.0044	0.0057	0.0083	0.0037

N: coordination number of the bond; *R*: interatomic distance of the bond;
^{2}: Debye-Waller factor of the bond.

4.3.2 Oxidation of FeS

4.3.2.1 Iron in FeS Oxidation

FeS inhibits UO_2 oxidative dissolution by keeping DO levels low (Figure 4.2). To better understand the mechanism of this inhibition, the solution and solid phase FeS oxidation products were monitored. Given that previous work illustrated that Fe(II) and S(-II) within the FeS structure largely follow independent oxidation pathways (Jeong et al., 2010a), the tracking of each of their oxidation products is presented separately. The experimental results are compared with control experiments with FeS only (no UO_2) and show identical trends for both Fe(II) and S(-II) (Figure A.1). We conclude that at an FeS:UO_2 molar ratio of ~30:1, UO_2 solids do not notably influence the oxidation of FeS by DO.

Starting with Fe results, Figure 4.1 shows the characteristic trend of Fe_{diss} as a function of reaction time. Immediately after exposure to oxygen, $[Fe]_{diss}$ increased rapidly to a peak concentration of ~1.1 mM at 4 hr, followed by a sharp decrease of $[Fe]_{diss}$. Similar patterns of $[Fe]_{diss}$ were previously reported in the case of aerobic oxidation of mackinawite, although the maximum $[Fe]_{diss}$ occurred at shorter time (1 hr) for the higher P_{O2} of 0.2 atm (Jeong et al., 2010a). This behavior was attributed to incongruent Fe(II) dissolution from FeS. The preferential initial release of dissolved metal ions into the solution phase as the first step of oxidative decomposition has been observed for many other sulfide minerals, such as FeS_2, PbS, and FeAsS (Buckley and Woods, 1985; Mikhlin et al., 2000; Belzile et al., 2004; Mikhlin, 2007). After the initial increase, the subsequent decrease in $[Fe]_{diss}$ resulted from the oxidation of Fe(II) and precipitation of Fe(III) oxyhydroxides. The consumption of DO by Fe(II) oxidation is thought to be one of the primary reasons for the low DO levels at < 51 h.

To identify the Fe oxidation products, solid phase samples were collected and characterized using XRD (Figure 4.3) and Mössbauer spectroscopy (Figure 4.8). The initial synthetic FeS is dominated by a singlet in 77K spectrum (Figure 4.8a) due to low spin (LS) Fe(II) in tetrahedral environment (labeled as Fe(II)-LS-Tet), a spectral component noted in several Mössbauer studies. The two minor sextets noted in the spectrum (Fe(II)-B and Fe(II)-C), however, were not observed in the previous studies. Although the nature of the sextets is not clear, they are not due to greigite (Fe_3S_4) or any Fe(III)-oxyhydroxide (Murad and Cashion, 2004) given that identical spectra were obtained at both 4.2 K and 77 K. It is possible that these sextets represent Fe(II) sites within the FeS structure with slightly different coordination environment than the Fe(II)-LS-Tet (Mullet et al., 2002).

The Mössbauer spectra obtained at 4.5 K shows that the 4-hr sample is evidently different from the initial FeS (Figure 4.8b). A good fit with the data was realized in four different Fe environments, including Fe(II)-LS-Tet singlet, Site B Fe(II) sextet, Site C Fe(III) sextet, and ferrihydrite Fe(III). Only a small amount of the initial FeS (9% of the total Fe) was comprised by the Fe(II)-LS-Tet singlet, indicating significant structural changes in FeS within 4 hr of reaction. Hyperfine fields of the two inner sextets, labeled Site B Fe(II) and Site C Fe(III), are similar to the sextets noted in the 11 K Mössbauer spectrum of an unoxidized synthetic mackinawite prepared by the reaction of sulfide with metallic Fe (Mullet et al., 2002). The Site C sextet is probably due to Fe(III) in the modified FeS structure as indicated by Mullet et al. (2002) because its features were virtually similar at both room temperature and 4.5 K. Mullet et al. (2002) further proposed that these two sextets are due to Fe(II)- and Fe(III)-Tet bound to monosulfide in a weathered thin layer covering the bulk material. Their premise was based on the EXAFS interpretation of Lennie and

Vaughan (1996), coupled to RT Mössbauer, Fe, S, and O X-ray photoelectron spectroscopy (XPS) analysis, and TEM observations of their sample. However, the inner sextets in the 4-hr sample may not be due to Fe(II) and Fe(III) in a thin weathered layer, given the large Site B Fe(II) contribution (75%) and the nearly complete transformation of the initial FeS to various species. Further studies, beyond the scope of this present study (e.g., TEM, XPS, surface Mössbauer, and dissolution studies), are needed to adequately address the nature of these two sextets. The unambiguous precipitation of ferrihydrite (9% of the total Fe) is identified by the comparison of the 77, 25, and 4.5 K spectra and model-derived Mössbauer spectral parameters of the outer sextet in the 4.5 K spectrum (Table 4.4). Based on a combination of Fe(III) in Site C and ferrihydrite, it appears that only ~15% Fe(II) of initial FeS was oxidized. The change of oxidized mackinawite is also reflected in the XRD pattern which shows a more prominent *001* peak (16.9 °2θ) and a diminished higher *hkl* peaks (Figure 4.3), a result of anisotropic dissolution of FeS. The presence of ferrihydrite is not evident in the XRD (Figure 4.3) due to low degree of crystallinity and concentration (9% of total Fe).

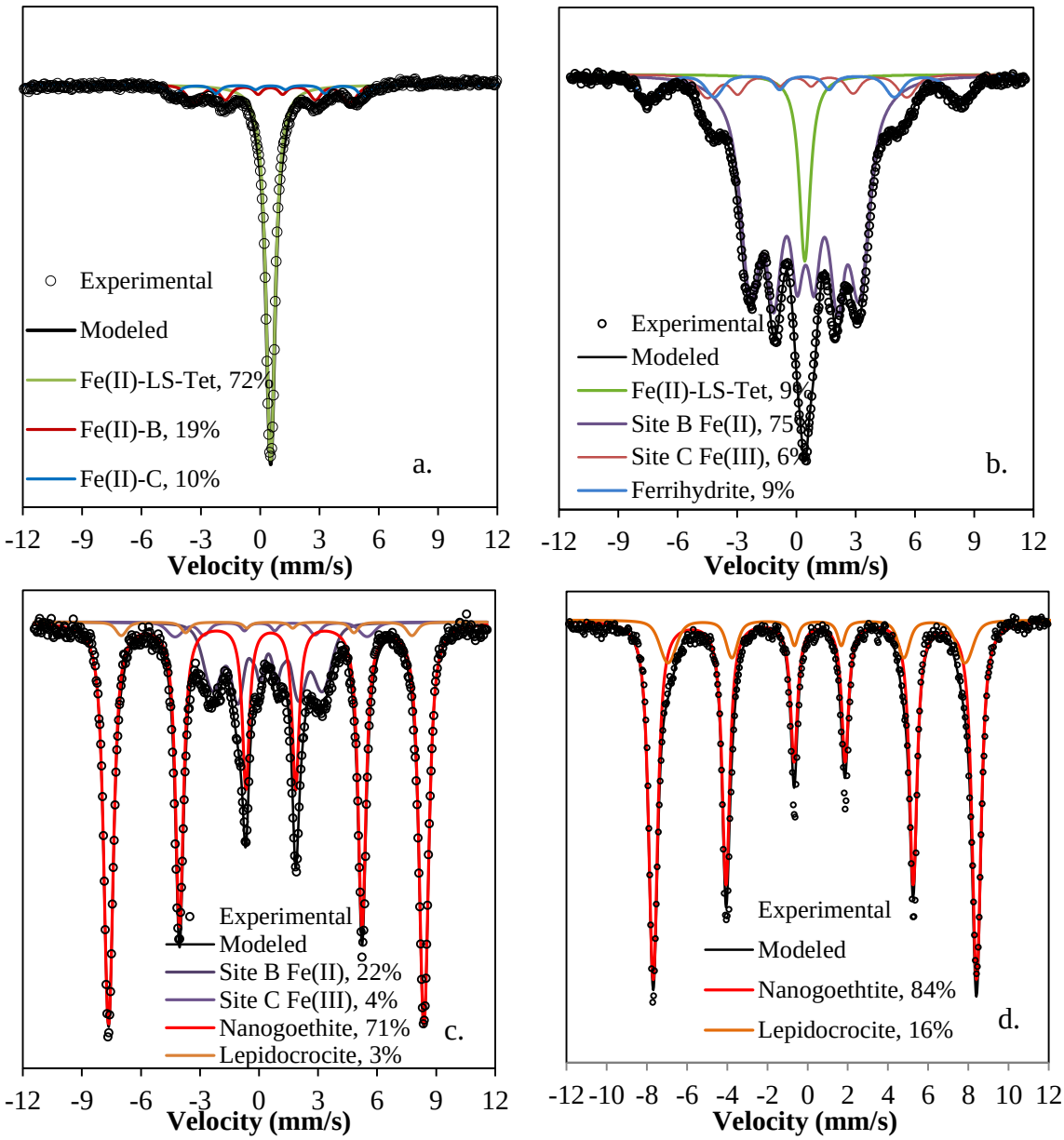

Figure 4.8 Mössbauer spectra (experimental and modeled) of initial and oxygen oxidized FeS samples: (a) initial synthetic FeS at 77 K (a singlet peak due to low spin Fe(II) in tetrahedral environments and two sextets due to Fe(II) in structurally different environments); (b) 4-hr sample at 4.5 K (Fe(II)-LS-Tet(a) and Fe(II)-LS-Tet(b), and Fe(III)-LS-Tet are due to Fe associated with the weathered layer, while the outer sextet is due to ferrihydrite); (c) 45-hr sample at 4.5 K; and (d) 168-hr sample at 4.5 K. *Circles* are experimental data; *black solid lines* are fitted models; and *colored lines* are elementary components. The relative abundance of each component is calculated as percentage in the legend.

The Mössbauer spectrum shows a complete disappearance of Fe(II)-LS-Tet singlet features at 45 hr oxidation (Figure 4.8c). Additionally, the Site B Fe(II) contribution decreases (also minor systematic changes occurred in the Mössbauer parameters, as anticipated) (Table 4.4) with a concurrent precipitation and accumulation of goethite. The persistence of Site B Fe(II) in this sample is in agreement with the sustained oxygen scavenging capacity of FeS up to ~60 hr. Besides goethite, the sample contained minor amounts of lepidocrocite. The formation of goethite and lepidocrocite likely resulted from the transformation of ferrihydrite (Fig. 4.6b) catalyzed by aqueous Fe(II) in the suspension (Pedersen et al., 2005; Yee et al., 2006). A comparison of the 4.5 K spectrum to the room temperature and 77 K spectra (not shown) further indicate that the goethite is nanoparticulate.

As oxidation continued, nanogoethite and lepidocrocite grew in abundance at the expense of Site B Fe(II) and Site C Fe(III) (Figure 4.8d). Nanogoethite and lepidocrocite made up the Fe mineralogy of the 120-hr sample (Figure 4.3), consistent with the results reported by Jeong et al. (2008) and Chirita et al. (2008). The Mössbauer spectroscopy study clearly demonstrates that the FeS oxidation to nanogoethite and lepidocrocite proceeded via an intermediate Fe(II)-dominant Fe(II)/Fe(III) state (Site B and Site C) that was not discernible from XRD. The various Fe(III) solid products, including nanoparticulate nanogoethite and lepidocrocite, are responsible for controlling the concentration of U(VI) in solution by adsorption and promoting UO_2 oxidation. The role of specific Fe(III) oxyhydroxide products in UO_2 oxidation, however, remains to be determined.

Table 4.4 Mössbauer parameters for initial mackinawite and selected oxidized samples at 77 K and 4.5 K.

Sample	Temp.	Mineral /Fe-species	Mössbauer parameters[a]						
			HWHM (mm/sec)	<CS> (mm/sec)	or (mm/sec)	stdev< (mm/sec)	Tesla	stdev Tesla	Area (%)	χ^2 (reduced)
Initial FeS	77 K	Fe(II)-LS-Tet	0.25	0.53	0.11	0.09	na	—	72	2
		Fe(II)-B		0.56	0.037	—	24.4	1.51	19	
		Fe(II)-C		0.48	-0.05	—	29.6	0.73	10	
4 hr oxidized	4.5 K	Fe(II)-LS-Tet	0.32	0.43	0.1	0.075	—	—	9	1.7
		Site B Fe(II)		0.45	-0.02	—	15.8	5.4	75	
		Site C Fe(III)		0.25	0.29	—	31.3	1.8	6	
		Ferrihydrite		0.41	0.01		48.7	2.7	9	
45 hr oxidized	4.5 K	Site B Fe(II)	0.21	0.46	-0.02	—	16.1	3.7	22	1.2
		Site C Fe(III)		0.32	0.29	—	30.3	1.8	4	
		Nanogoethite		0.48	-0.12	—	49.7	0.8	71	
		Lepidocrocite		0.47	-0.08	—	45.8	1.0	3	
168 hr oxidized	4.5 K	Nanogoethite	0.21	0.48	-0.12	—	49.9	0.6	84	2.1
		Lepidocrocite		0.48	-0.03	—	45.8	1.9	16	

HWHM = half-width at half maximum < CS> = average center shift; < = average quadrupole splitting; < = averagequadrupole shift parameter; <H> = average hyperfine field;
stdev = standard deviation; na = not applicable; χ^2= reduced chi square (goodness of the fit).

4.3.2.2 Sulfur in FeS Oxidation

Along with Fe(II) dissolution and oxidation, another mechanism for the effective scavenging of oxygen during the initial 51 hr is the redox reaction that occurs with S(-II) in the FeS structure. A variety of sulfur species may result from FeS oxidation, including polysulfides (S_n^{2-}), elemental sulfur (S_8^0), thiosulfate ($S_2O_3^{2-}$), and sulfate (SO_4^{2-}) (Schippers and Sand, 1999; Chirita, 2009; Jeong et al., 2010a). Due to the very rapid decomposition of polysulfides (Rickard and Morse, 2005), only S^0_8, $S_2O_3^{2-}$, and SO_4^{2-} were quantified in this study. The overall trends of S(-II) oxidation are tracked by measured Eh (Figure 4.9a).

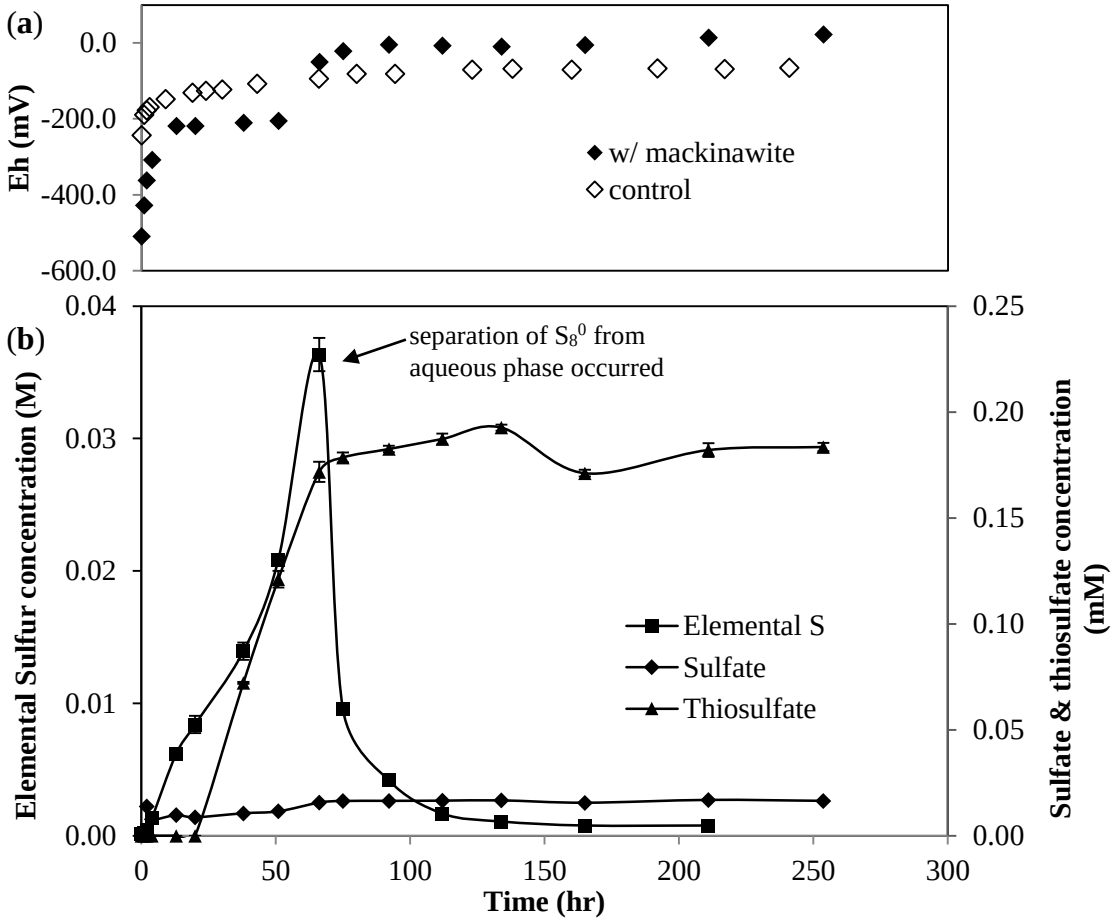

Figure 4.9 The kinetic profiles of (a) sulfur species, i.e., elemental sulfur, thiosulfate, and sulfate; and (b) Eh during the oxidation experiments. The arrow indicates the event of S_8^0 separation from the aqueous phase. Error bars reflecting one standard deviation of analysis are sometimes smaller than the symbol size.

As Figure 4.9b shows, S_8^0 was the primary intermediate S oxidation product throughout the experiment. Over the first 2 hr reaction, no oxidized S species were detected, indicating preferential Fe(II) oxidation was dominant in this time frame. Elemental sulfur began to appear at 4 hr of reaction with its concentration rapidly increasing to a maximum at ~66 hr (0.036 M). The peak concentration of S_8^0 accounted for only ~65% of the total S input as FeS (0.056 M). The loss of H_2S gas from the reactor or losses of S_8^0 to the air-water interface may have led to an incomplete recovery of sulfur. The transformation of structural sulfide into S_8^0 is supported by XANES spectra (Figure 4.10). Sulfur *K*-edge XANES spectra clearly illustrate the evolution of the S(-II) moiety of FeS to S_8^0 in the solid phase, although an intermediate polysulfide phase was not identified. The peak at 2470.4 eV gradually decreased over time, accompanied by the increase of S_8^0 peak at 2472.4 eV until FeS was completely depleted. Consistent with the extraction results in Figure 4.9b, the more oxidized sulfur species were not detected in the XANES spectra, suggesting their minor existence in the system. A linear combination fitting of XANES spectra (Table 4.5) indicated that ~50% of mackinawite S(-II) was transformed to S_8^0 by 24 hr reaction. The oxidation of S(-II) and polysulfide, together with Fe(II) oxidation, probably consumed almost all DO during the first 51 hr of oxidation, until all FeS was depleted and the formation of S_8^0 was complete.

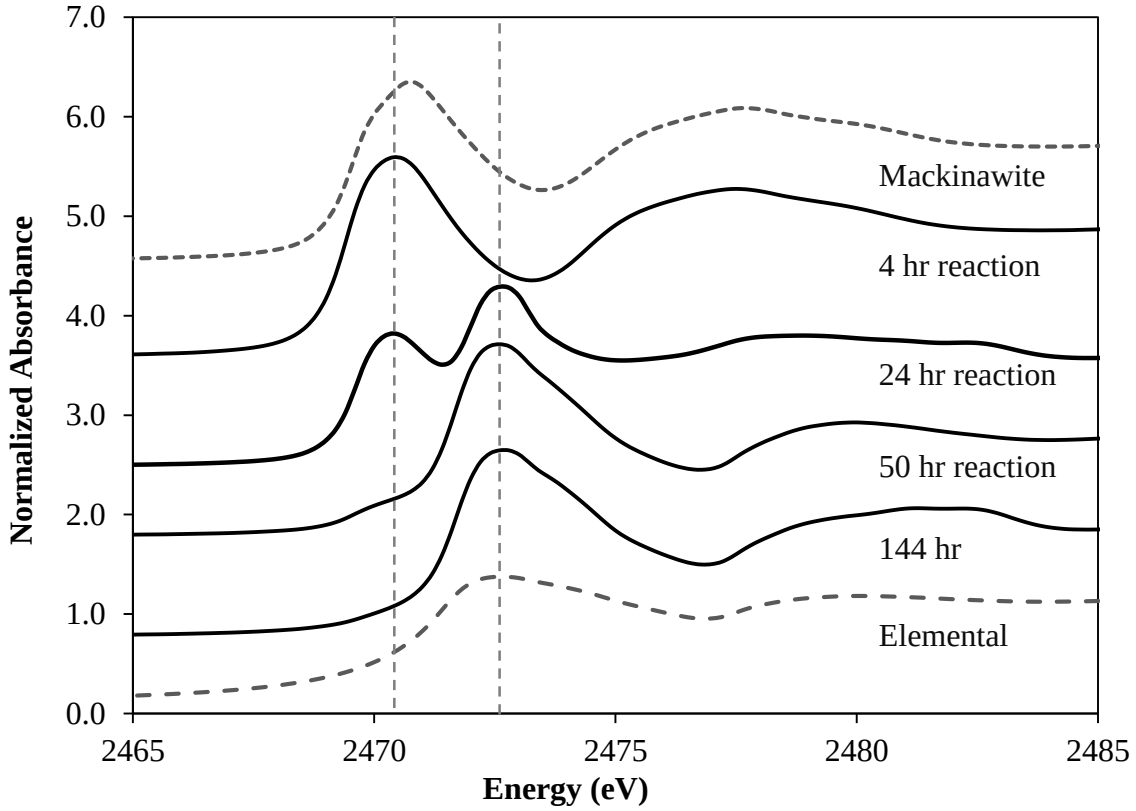

Figure 4.10 Sulfur *K*-edge XANES spectra of batch samples over the course of the FeS oxidation experiment.

Table 4.5 Sulfur speciation in samples of FeS as calculated by XANES linear combination fitting. The relative concentration of S components, i.e., mackinawite and elemental sulfur are presented as percentages. Relative errors of fitting are given in parentheses.

	4 hr	**24 hr**	**50 hr**	**138 hr**
S(-II) (%) Mackinawite	100 (0.5)	56.5 (1.8)	2.8 (1.4)	0
S(0) (%) Elemental sulfur	0	46.4 (2)	96.5 (2.5)	100 (5.4)

The occurrence of $S_2O_3^{2-}$ was first observed at 4 hr, but the concentration of $S_2O_3^{2-}$ only slowly increased to ~0.18 mM at 75 hr and remained at this level. In contrast, SO_4^{2-} remained at an even lower concentration throughout the experiment, and only slightly

increased over time. Both of the sulfur oxidation species were insignificant relative to the production of S_8^0, indicating the dominance of S_8^0 in this abiotic system. This result has been reported previously in FeS systems where microbial activity is absent (Burton et al., 2006; Burton et al., 2009). Assuming that the effective oxidative transformation of S_8^0 requires sulfur-oxidizing bacteria (Burton et al., 2009), the resistance of S_8^0 to chemical oxidation by oxygen, as observed in the present study, is expected. The absence of pH change also confirms a lack of oxidative S_8^0 conversion into $S_2O_3^{2-}$ and SO_4^{2-}. For example, if the ~0.036M amount of S^0_8 observed at 66 hr had been completely oxidized, a large number of protons would have been generated, along with a lower solution pH based on Eq. 4.1 and 4.2.

$$\frac{1}{8}S_8^0(s)+\frac{3}{2}O_2+H_2O = SO_4^{2-}+2H^+ \qquad (4.1)$$

$$\frac{1}{8}S_8^0(s)+6Fe^{3+}+4H_2O = SO_4^{2-}+6Fe^{2+}+8H^+ \qquad (4.2)$$

Considering the concurrent formation of iron oxyhydroxides (i.e., nanogoethite and lepidocrocite), the overall reaction for the FeS oxidation in this study is proposed as:

$$FeS(s)+\frac{3}{4}O_2+\frac{1}{2}H_2O= \frac{1}{8}S_8^0(s)+FeOOH(s) \qquad (4.3)$$

The preferential reaction of oxygen with nano-sized FeS thus effectively inhibits UO_2 oxidation until FeS is depleted by oxidation.

4.4 Conclusions

The long-term success of *in situ* reductive immobilization of U depends on the stability of U(IV) precipitates (e.g., uraninite) under redox fluctuating redox conditions. As this work shows, reoxidation and mobilization of uraninite may take place relatively rapidly, even in the presence of relatively low DO (~0.7 mg/L) when FeS is absent. When present, FeS can effectively inhibit the oxidation of UO_2 by keeping DO low as long as it persists. Upon the depletion of FeS, a rapid oxidative dissolution of UO_2 may result, leading to the complete oxidation of UO_2 to U(VI) species. Fe oxyhydroxides formed during oxidation then provide an adsorptive sink for dissolved U(VI). In view of the results of this work, the following general conclusions may be drawn:

1. Mackinawite can provide practical protection of UO_2 precipitates when it is added or naturally formed as a result of biostimulation of SRB. The stability of U(IV) solid phases is maintained in the presence of FeS as a result of the preferential reaction of DO with FeS before reacting with U(IV). Given that bacteria capable of reducing U, Fe, and SO_4^{2-} are ubiquitous in natural systems, reduced U(IV) solids and FeS can be simultaneously produced at U-contaminated sites where Fe(III) minerals and sulfate are frequently encountered. In such cases, FeS may serve as an effective oxygen scavenger and redox buffer, and aid in keeping U(IV) stabilized in U contaminated environments undergoing redox cycling.

2. The extent of FeS protection may be limited by its physical proximity and concentration relative to UO_2. When in excess of DO concentrations, FeS persistence may significantly inhibit UO_2 oxidative dissolution. Provided that sulfate reducing conditions are eventually restored before DO levels rise significantly, the concentration

of dissolved U(VI) may remain insignificant in the groundwater. However, when oxidants, such as oxygen, are in excess of the reducing capacity of FeS, the consumption and depletion of FeS by oxygen may ultimately facilitate UO_2 oxidation. Therefore, the effectiveness of FeS and extent of its protection will vary depending on the molar ratio of FeS to UO_2 (~30:1 in this study) and its proximity to U(IV) phases.

3. Although the incorporation of U(VI) into the structure of iron oxyhydroxide was not apparent in this study, significant adsorption of U(VI) species onto the FeS oxidation products was observed. Further investigations are needed to evaluate of the impact of oxygen concentration, pH, and other solution conditions, to determine whether effective immobilization of U(VI) into the structure of iron oxyhydroxides is possible.

Following these conclusions, the next study seeks to examine the impact of FeS on the kinetics of abiotic UO_2 oxidative dissolution in artificial oxic groundwater under field-relevant conditions. If the dissolution rate of UO_2 can be inhibited by FeS to a significantly low level, the long-term stability of reduced U(IV) against reoxidation may be promising after effective biostimulation operations.

Chapter 5

Nano-FeS Impedes UO_2 Dissolution Rate under Varied Oxic Conditions

5.1 Introduction

As shown in Chapter 4, uraninite is thermodynamically unstable in the presence of oxygen and can be effectively oxidized and consequently dissolved within several hours to days in batch or sediment column experiments (Casas et al., 1994; de Pablo et al., 1996; Pierce et al., 2005). Oxidative dissolution of UO_2 by oxygen has been proposed to occur through a sequence of reaction steps at the UO_2 surface, including oxygen adsorption, formation of activated surface complexes, electron transfer, and subsequent release of U(VI) products (Torrero et al., 1997; Shoesmith, 2000). Oxidative dissolution rates determined by various authors range from 10^{-12} to 10^{-7} mol m^{-2} s^{-1} based on batch and flow-through reactor studies (Casas et al., 1994; De Pablo et al., 1999; Pierce et al., 2005; Ulrich et al., 2009). Due to the complexity of the mechanism of oxidative UO_2 dissolution, a variety of rate-limiting steps have been proposed. At neutral to alkaline pH, oxidative dissolution may proceed through intermediate U oxides (i.e., U_3O_7 or U_4O_9), which may form a surface layer

---

This chapter is adapted from: Bi, Y.; Hayes, K. F., Nano-FeS Inhibits UO_2 Reoxidation under Varied Oxic Conditions. *Environ. Sci. Technol.* **2013,** *48* (1), 632-640.

surrounding a core of UO_2 (de Pablo et al., 1996; Torrero et al., 1997; Finch and Murakami, 1999). Oxygen diffusion through the passivation layer to contact fresh UO_2 surface and oxidize U(IV) may also be rate limiting, particularly when the oxygen concentration is low (Grambow, 1989; De Pablo et al., 1999). Alternatively, in the presence of carbonate, Ulrich et al. (2009) proposed the detachment of U(VI)-carbonato complexes as the rate-limiting step based on the observation of increased dissolution rate relative to the carbonate-free system. It is likely that the rate-limiting step for UO_2 oxidative dissolution varies depending on the experimental conditions. The reaction rates can also be impacted if the reprecipitation of dissolved U forms secondary phases (Torrero et al., 1997; Finch and Murakami, 1999; Santos et al., 2006) or if reducing agents such as iron sulfides are simultaneously present, which can react with dissolved or solid-phase U species.

Long-term stability of reduced U(IV) solids may be achieved when the dissolution and/or reoxidation of UO_2 are sufficiently slow during occasional low levels of oxidant intrusion. As shown in Chapter 4 and previously (Abdelouas et al., 1999b; Bi et al., 2013), oxygen scavenging by FeS retards UO_2 reoxidation and provides redox buffering during oxygen intrusion. Yet, the kinetics and mechanisms of UO_2 oxidative dissolution under oxic flowing conditions in the presence of FeS have not been addressed. The impact of geochemical variables, such as pH, DO concentration, and FeS concentration on the kinetics of UO_2 dissolution also has not yet been systematically studied.

The objective of the present study was to examine the impact of FeS on the rate of abiotic UO_2 oxidative dissolution in artificial oxic groundwater under field-relevant conditions. Using continuously stirred tank reactors (CSTRs), the kinetics of UO_2 dissolution was examined in the presence and absence of FeS. Dissolution rates were measured as a

function of pH, DO and FeS concentrations, and the solid phase reaction products were identified through spectroscopic techniques. A conceptual mechanistic reaction model was developed for the inhibition of UO_2 dissolution by FeS. The results of this study contribute to the understanding of the long-term stability of reduced U(IV) against reoxidation in groundwater environments, where oxic conditions prevail for brief periods, following a prolonged anoxic bioreductive period.

5.2 Experimental Methods

5.2.1 Oxidative Dissolution Experiments

The oxic flow-through experiments were conducted with 50 mL CSTRs (Millipore 8050) under varied pH (6.1 – 8.1; common for groundwater), DO influent concentration (0 – 7.8 mg/L to simulate oxygen intrusion into a reducing zone), and FeS concentration (Fe:U molar ratios of ~2.5 – 120 to simulate excess Fe ranges in a bioreduced zone). A detailed description of the setup is given in Chapter 3. Each reactor was loaded with ~0.48 mM UO_2 suspension and FeS of varied concentrations to provide the desired FeS:UO_2 ratio. All feed solutions were constantly purged with custom $CO_2/O_2/N_2$ gas mixtures and prepared with MilliQ water containing 0.4 mM KCl, 2.0 mM $CaCl_2$, and different $NaHCO_3$ concentrations to achieve a final pH of 6.1, 7.1, or 8.1 (Table 5.1). With a flow rate between 1.8-2.2 mL min^{-1}, the CSTR has a hydraulic residence time (τ) of ~25 min. Experiments were operated until DO breakthrough occurred or the inhibited UO_2 dissolution period ended, typically up to 200 residence times. The inhibition period is defined as the time over which $[U]_{diss}$ remains at average steady-state concentration before DO breakthrough, i.e., when $[U]_{diss}$ increased by more than twice the standard deviation from the average steady-state

value. At the completion of flow-through experiments, solid samples were collected on the membrane by draining the reactor. A time series of solid samples were collected at 5, 120, and 160 residence times from experiments of fixed pH 7.1, 1.8 mg L^{-1} DO, and 18.7 mM FeS. Additional solid sample was taken from a control experiment of pH 7.1 and 1.8 mg L^{-1} DO in absence of FeS after reaction of 65 residence times. This flow-through system was also utilized to study the dissolution of UO_2 under oxygen-free conditions in the presence and absence of FeS.

Table 5.1 Groundwater compositions in equilibration with $CO_2/O_2/N_2$ gas mixtures for pH 6, 7, and 8 experiments.

Gas mixture $CO_2/O_2/N_2$ (vol%)	$NaHCO_3$ (mM)	$CaCl_2$ (mM)	KCl (mM)	Influent pH	Influent DO (mg/L)	Influent DIC* (mM)
5/4/91	0.8	2.0	0.4	6.1	1.8	2.5
5/4/91	8.0	2.0	0.4	7.1	1.8	9.7
0/4/96	1.0	2.0	0.4	8.1	1.8	1
5/20/75	8.0	2.0	0.4	7.1	7.8	9.7
5/0/95	8.0	2.0	0.4	7.1	<0.2	9.7

* Concentration calculated from Visual MINTEQ at equilibrium with the gas mixtures

The experimental conditions chosen for this study, such as pH and DO, reflect the typical geochemical conditions found in the field: U-contaminated groundwater typically has a pH of 6.5-8.5, which is similar to the pH range used in this study. The DO concentration in this study was selected to simulate groundwater with elevated DO levels in an unconfined aquifer from water table fluctuation and oxygen intrusion, allowing mildly-oxidizing to near DO saturation.

5.2.2 Sample Analyses

Total dissolved uranium and iron were determined in effluent samples by ICP-MS (PerkinElmer ELAN DRC-e). Dissolved Fe(II) was measured photometrically by the

ferrozine method at 562 nm using a UV/Vis spectrophotometer (Varian) (Stookey, 1970), which was compared with total Fe concentration measured by ICP-MS. The dissolved Fe(II) equaled the total dissolved Fe measured by ICP-MS within an error of 5%. Using numerical integration, released Fe(II) (μmol) during the inhibition period was estimated for each experiment. The dissolved sulfide in the effluent was determined by a silver-sulfide ion selective electrode (Fisher Scientific accumet) (Wilmot et al., 1988). Selected aqueous samples were also analyzed by IC (Dionex) for $S_2O_3^{2-}$ and SO_4^{2-}.

Solid samples collected from flow-through reactors at pH 6.1, 7.1, and 8.1 were characterized by powder X-ray diffraction (XRD) using a Rigaku 12 kW rotating anode diffractometer at 40 kV and 100 mA with a monochromated Cu-K_α radiation from 10 ºto 70 º range of 2-θ.

In selected experiments, XAS analyses of wet solid pastes from the CSTR were performed at the Stanford Synchrotron Radiation Lightsource (SSRL) as previously described in Chapter 4. Uranium L_{III}-edge absorption spectra were collected in fluorescence mode at Beamline 4-1 or 11-2 using a 13- or 100-element Ge detector at a low temperature (77 K). Sulfur *K*-edge spectra were collected at Beamline 4-3 in fluorescence mode using a passivated implanted planar silicon detector at room temperature under an inert (He) atmosphere. XAS data were later subjected to X-ray absorption near edge structure (XANES) and extended X-ray absorption fine structure (EXAFS) analyses using SixPACK and IFEFFIT code (Newville, 2001; Webb, 2005).

5.2.3 Dissolution Rate Calculation

After reaching a steady-state effluent uranium concentration, the oxidative dissolution rate of UO_2 (R_m) (mol g^{-1} s^{-1}) by oxygen was obtained using the equation 5.1:

$$R_m = \frac{[U]_{ss} \times Q}{V \times [UO_2]} \qquad (5.1)$$

where R_m (mol s^{-1} g^{-1}) is a mass-normalized oxidative dissolution rate of UO_2, Q (L s^{-1}) the flow rate, V (L) the reactor volume, $[U]_{ss}$ (mol L^{-1}) the steady-state concentration of total dissolved uranium, and $[UO_2]$ (g L^{-1}) the mass concentration of uraninite in the reactor. Due to the unknown degree of aggregation and thus uncertainty in synthetic UO_2 surface area, surface-area normalized rate (mol m^{-2} s^{-1}) were not estimated in this study.

After an initial non-steady state period (related to start-up and reactor mixing), steady-state U effluent concentration was typically reached after ~50 residence times, and maintained until the end of the inhibition period prior to significant U(VI) concentration breakthrough. The reported steady-state effluent U concentrations are the average of measurements from at least 6 samples for all experiments. Error bars represent two standard deviations of the rate calculated from the reactor output at steady-state, reflecting the 95% confidence interval. During the inhibition period, less than 6% of the total UO_2 dissolved and exited the CSTR. In comparison, control experiments in the absence of FeS released about 50% of the total U at the end of steady-state dissolution, resulting in a decreased mass of UO_2. The mass of UO_2 during steady-state dissolution was adjusted in the rate calculations for all experiments.

5.3 Results

5.3.1 Inhibited UO_2 Dissolution Rate

In the presence of FeS, the oxidative dissolution of UO_2 was inhibited and resulted in low levels of U concentration (<1 μM) over a range of solution conditions (Table 5.2). Examples of UO_2 dissolution profiles at pH 7.1 (experiment 2a and 2b in Table 5.2) are shown in Figure 5.1. After the initial start-up period, the steady-state $[U]_{ss}$ was less than 0.2 μM. The low effluent U concentrations remained for a total of ~160 residence times over the inhibition period before rapidly increasing due to FeS depletion. Over the pH range of 6.1–8.1, similar levels of effluent U concentration were observed in the presence of 18.7 mM FeS, while $[U]_{ss}$ in absence of FeS were significantly greater at ~4 μM (Figure 5.2).

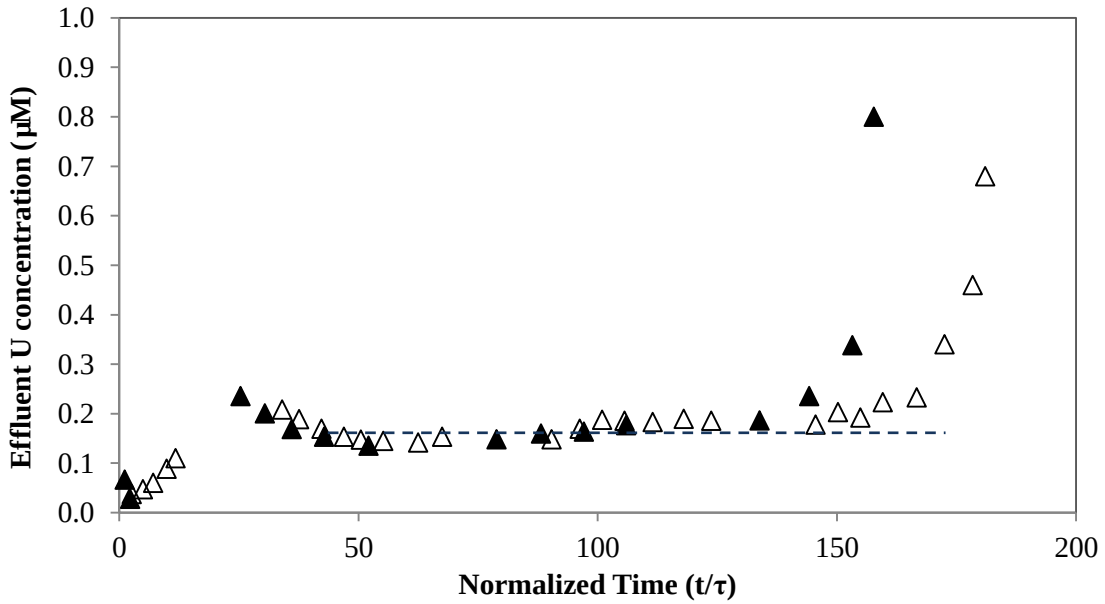

Figure 5.1 Uranium dissolution profiles in the flow-through experiments at pH 7.1 (experiments 2a, 2b in Table 5.2) in the presence of 18.7 mM FeS. Influent solution contains 1.8 mg L^{-1} DO. Replicates are represented by the filled vs open symbols. The dotted line represents the steady-state U concentration used for rate calculation. The normalized time is calculated by dividing real reaction time (t) by the hydraulic residence time (τ) of the reactor.

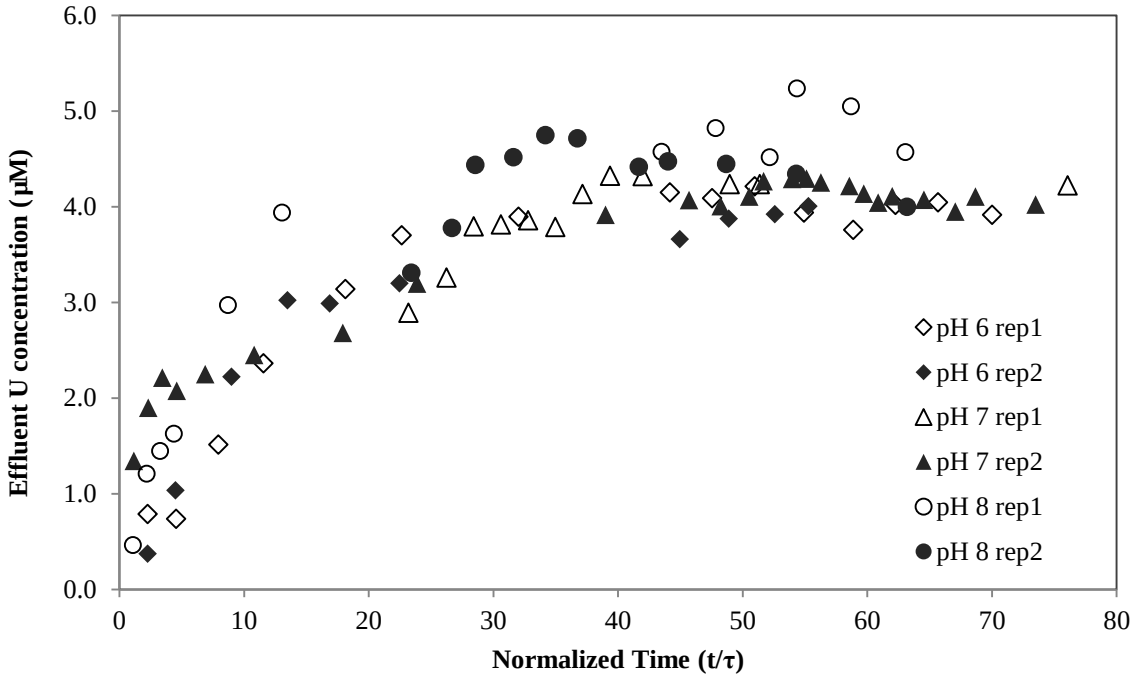

Figure 5.2 Uranium dissolution profiles at various pH in the flow-through experiments in absence of FeS. Replicates are represented in filled or empty symbols. Experimental conditions: 1.8 mg/L DO and 0.48 mM UO_2.

Table 5.2 Experimental UO_2 dissolution rates normalized to solid mass (R_m) obtained under various combinations of oxidizing conditions and water compositions.

Exp. ID	Initial $[UO_2]$ (mM)	Initial [FeS] (mM)	pH	DO (mg L^{-1})	DIC* (mM)	Flow rate (mL min^{-1})	$[U]_{ss}$ (μM)	$R_m \times 10^{-10}$ mol g^{-1} s^{-1}	Inhibition duration (t/τ)
Variation of pH									
1a	0.48	18.7	6.1	1.8	2.5	1.83	0.124	5.81 ± 0.36	120
1b	0.48	18.7	6.1	1.8	2.5	1.98	0.106	5.39 ± 0.65	115
2a	0.48	18.7	7.1	1.8	10	1.88	0.162	7.80 ± 0.54	168
2b	0.48	18.7	7.1	1.8	10	1.96	0.168	8.48 ± 0.47	158
3a	0.48	18.7	8.1	1.8	1	1.82	0.182	8.50 ± 0.35	183
3b	0.48	18.7	8.1	1.8	1	1.91	0.145	7.14 ± 0.43	195
Control	0.48	\	6.1	1.8	2.5	1.87	3.94	257 ± 4.8	n/a
Control	0.48	\	6.1	1.8	2.5	1.89	4.01	268 ± 6.8	n/a
Control	0.48	\	7.1	1.8	10	1.91	4.18	298 ± 4.2	n/a
Control	0.48	\	7.1	1.8	10	1.82	4.24	295 ± 3.9	n/a
Control	0.48	\	8.1	1.8	1	1.81	4.80	334 ± 16	n/a
Control	0.48	\	8.1	1.8	1	1.95	4.55	328 ± 8.2	n/a
Variation of FeS									
4a	0.48	56.8	7.1	1.8	10	1.87	0.116	5.32 ± 0.28	490
5a	0.48	4.8	7.1	1.8	10	1.87	0.503	23.2 ± 2.5	48
5b	0.48	4.8	7.1	1.8	10	1.91	0.418	19.1 ± 1.4	49
6a	0.48	1.2	7.1	1.8	10	1.85	0.936	42.7 ± 6.7	9
Variation of DO									
7a	0.48	18.7	7.1	7.8	10	1.84	0.323	15.3 ± 0.65	53
7b	0.48	18.7	7.1	7.8	10	2.15	0.247	13.6 ± 0.77	50
8a	0.48	18.7	7.1	<0.2	10	1.88	0.111	5.38 ± 0.43	n/a
Control	0.48	\	7.1	7.8	10	2.24	7.02	554 ± 13	n/a
Control	0.48	\	7.1	7.8	10	2.19	6.44	505 ± 47	n/a
Control	0.48	\	7.1	<0.2	10	1.85	0.428	20.7 ± 0.65	n/a

* Dissolved inorganic carbon calculated from Visual MINTEQ at equilibrium with CO_2 gas mix used.

For the three pH conditions studied, FeS reduced the rates of UO_2 dissolution by more than an order of magnitude compared to the rates in its absence (Figure 5.3a). FeS inhibited UO_2 oxidative dissolution by consuming the DO entering the CSTR. With an influent DO concentration of 1.8 mg L^{-1}, FeS reduced the DO level in the CSTR to <0.5 mg L^{-1} as measured in the effluent solution by a DO probe, which has a detection limit of ~0.2 mg L^{-1}. Higher DO levels between 1.3–1.9 mg L^{-1} were observed in the effluent for control

experiments in absence of FeS, consistent with the higher influent DO levels. With similar levels of DO, the UO_2 dissolution rates were found to be independent of pH in this study.

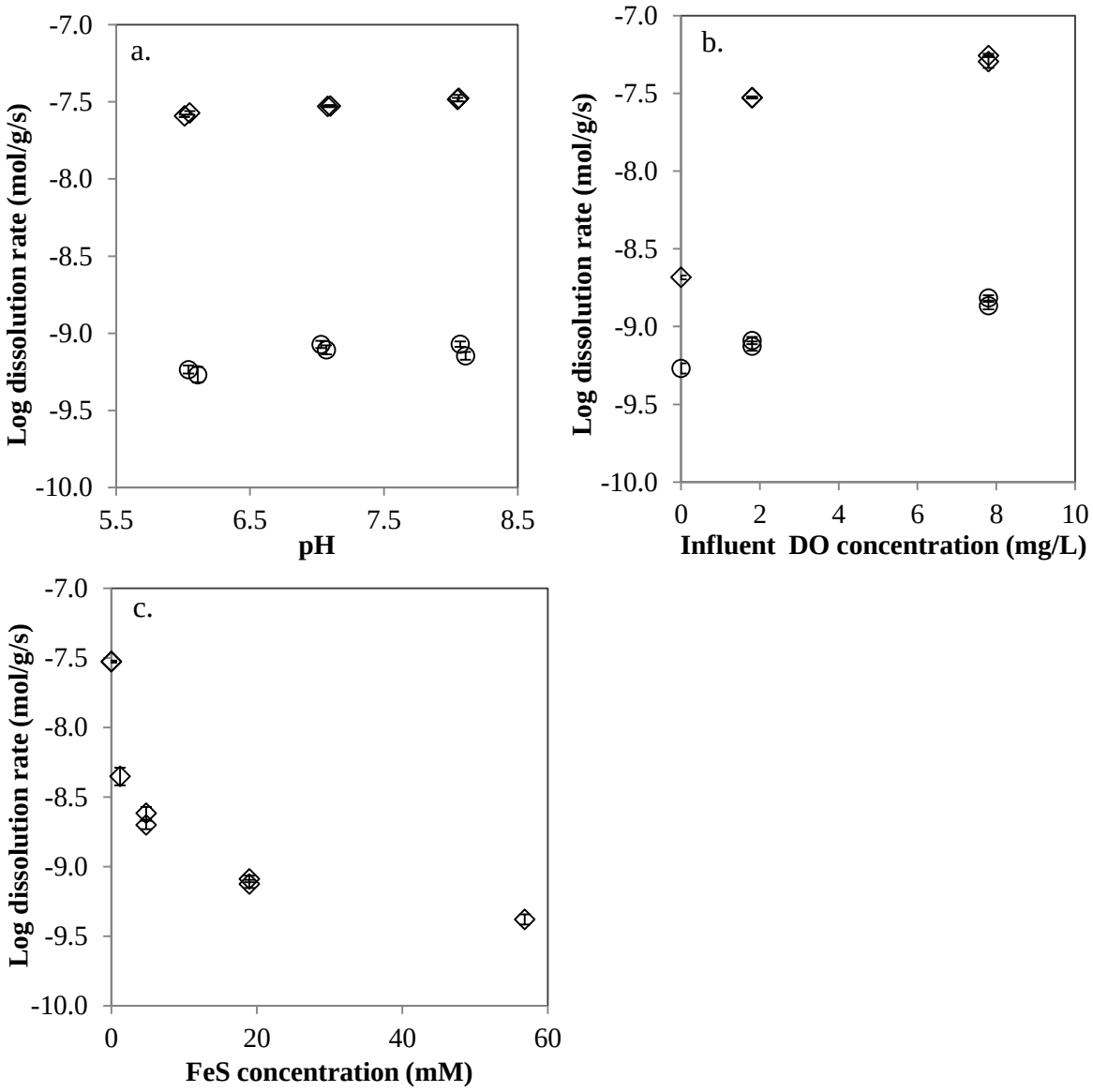

Figure 5.3 Steady-state UO_2 dissolution rates (mol g^{-1} s^{-1}) determined in the presence (○) and absence (◊) of FeS as a function of (a) pH; (b) DO concentration (mg·L^{-1}) at18.7 mM FeS and pH 7.1; and (c) FeS concentration (g/L) at pH 7.1. Error bars represent 95% confidence interval of 6 to 16 individual samples for the dissolution rates.

At pH 7.1 and FeS concentration of 18.7 mM, the inhibited UO_2 dissolution rate increased with increasing influent DO concentration (Figure 5.3b), but remained significantly lower than the control without FeS. At 7.8 mg L^{-1} DO, FeS inhibition resulted in a $[U]_{diss}$ of 0.26–0.32 μM and dissolution rate of 13.6–15.3 $\times 10^{-10}$ mol g^{-1} s^{-1}, compared to the more than one order of magnitude higher rate for the control (~5.4 $\times 10^{-8}$ mol g^{-1} s^{-1}). During the inhibition period, DO was effectively reduced to well below 0.5 mg L^{-1} by FeS in the CSTR. In contrast, the rate obtained under anoxic conditions was 5.4 $\times 10^{-10}$ mol g^{-1} s^{-1}, which resulted in the lowest UO_2 dissolution rate in the presence of FeS. Interestingly, this rate was even lower than an "anoxic" control experiment (~20 $\times 10^{-10}$ mol g^{-1} s^{-1}), indicating the complete removal of O_2 in the flow-through system with no FeS was not achieved (see section 5.4.1).

At a fixed UO_2 concentration of 0.48 mM, pH = 7.1, and DO = 1.8 mg L^{-1}, higher FeS concentrations resulted in lower $[U]_{ss}$ and UO_2 dissolution rates (Table 5.2, Figure 5.3c). The lowest rate of 5.3 $\times 10^{-10}$ mol g^{-1} s^{-1} was observed in the presence of 56.8 mM FeS, ~70% of the rate at 18.7 mM FeS. In the presence of 4.8 mM FeS, the dissolution rate increased to ~20 $\times 10^{-10}$ mol g^{-1} s^{-1}. At the lower FeS concentration of 1.2 mM, a faster rate of 42.7 $\times 10^{-10}$ mol g^{-1} s^{-1} occurred. Although low DO levels occurred in the effluent in the presence of FeS, they increased slightly from ~0.3 to 0.9 mg L^{-1} when the FeS loading decreased from 56.8 mM to 1.2 mM.

5.3.2 Fe(II) Release and Inhibition Duration

The consumption of DO by FeS was accompanied by a pH-dependent Fe(II) release into the effluent solution. At pH 6.1, considerable FeS dissolution resulted in a higher

dissolved Fe(II) concentration compared to that at higher pH (Figure 5.4). The concentration of dissolved Fe(II) quickly peaked at ~0.15 mM after ~6 residence times; it then slowly dropped to ~0.11 mM and remained at this level for roughly 115 residence times. At pH 7.1, the concentrations of Fe(II) peaked at lower values and continuously decreased over the entire period of DO consumption. The smallest release of Fe(II) was found at pH 8.1, where detectable Fe(II) persisted for only the initial ~35 residence times. Approximately 81% of the total Fe was released as dissolved Fe(II) at pH 6.1, compared to 27% and 0.2% of total Fe released at pH 7.1 and 8.1, respectively. Notably, the duration of inhibited UO_2 dissolution was closely related to the released amount of Fe(II) into effluent, which was estimated for each experiment during the inhibition period. A regression analysis on the inhibition duration vs. the percentage of Fe(II) release provides a good linear relationship between the two variables, with smaller total Fe(II) release leading to longer inhibition time. The slightly acidic pH 6.1, at which considerable Fe(II) dissolution occurred as noted above, resulted in a significantly reduced inhibition period as compared to that at higher pH.

DO and FeS concentrations also influenced Fe(II) release and the inhibition period of UO_2 dissolution. Higher DO concentrations resulted in a higher and sharper Fe(II) peak and a faster drop in Fe(II) concentration, while lower DO caused a lower and broader peak but a longer persistence of dissolved Fe(II) in the effluent (Figure 5.5). The amount of released Fe(II) decreased with increasing influent DO concentration, suggesting more FeS oxidized to Fe(III) precipitates in the CSTR at higher DO. With a DO concentration of 1.8 mg L^{-1} and pH of 7.1, decreasing FeS concentration resulted in less Fe(II) release, which was proportional to the added FeS. The longer inhibition period is therefore linearly correlated with greater FeS concentration and Fe(II) release at a fixed pH and DO concentration.

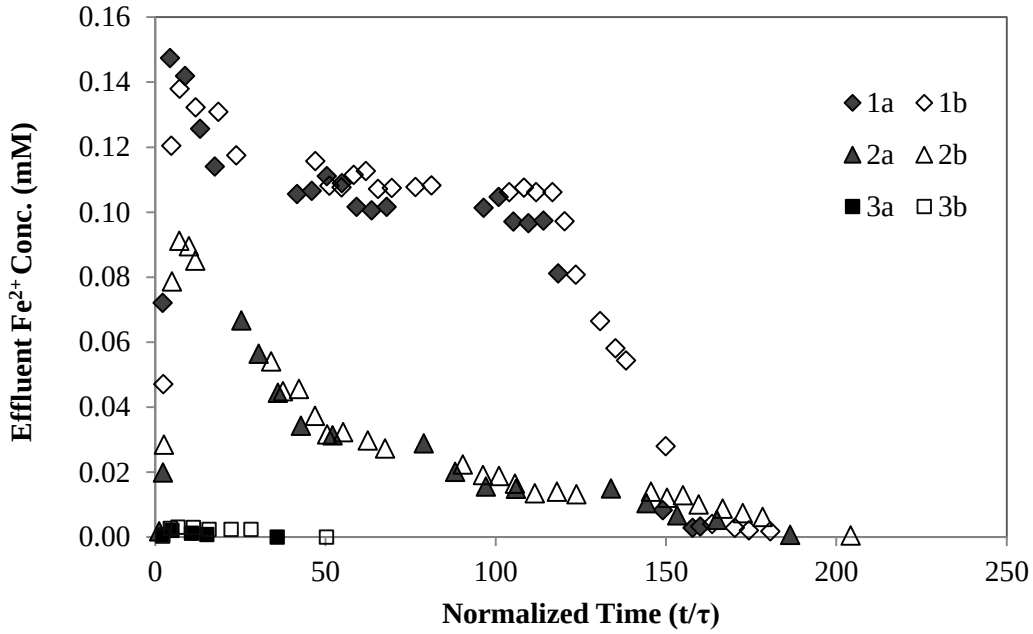

Figure 5.4 The dissolved Fe(II) release profiles from FeS dissolution at different pH (experiments 1a, 1b, 2a, 2b, 3a, and 3b in Table 5.2) containing 1.8 mg L^{-1} DO. Replicates are represented by the filled vs open symbols.

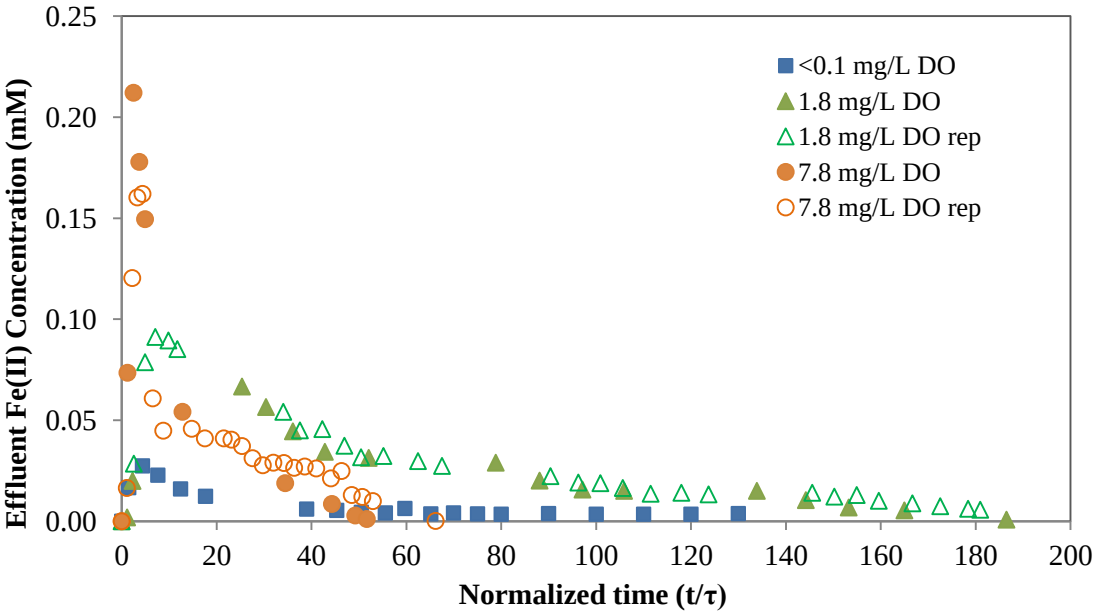

Figure 5.5 The dissolved Fe(II) release profiles from FeS dissolution at different influent DO concentrations of pH 7 artificial groundwater. Replicates are represented in filled or empty symbols.

5.3.3 Characterization of U Solid Phase with XAS.

A time series of solid samples were collected from the CSTR at 5, 120, and 160 τ from the replicate experiments run at the conditions of pH 7.1, 1.8 mg L^{-1} influent DO, and 18.7 mM FeS. The first two samples were taken during the inhibition period of UO_2 dissolution, while the last sampling occurred immediately after oxygen breakthrough. These CSTR samples, along with an oxidized UO_2 sample from a control experiment, were then characterized by XANES and EXAFS analyses of U L_{III}-edge spectra.

XANES analysis showed that the solid U samples were predominantly made up of U(IV) (>90%) over the entire inhibition period (Figure 5.6 and Table 5.3). EXAFS spectra, fits, and associated Fourier transforms (FTs) (Figure 5.7) confirmed that nano-sized UO_2 was the primary U(IV) solid phase retained in the CSTR throughout the reaction period, with no significant accumulation of U(VI) species within the solid phases. The fitted parameters from the EXAFS analyses are listed in Table 5.4. In contrast, the sample from UO_2 control experiment showed a clear energy shift of the absorption edge from the U(IV) standard (Figure 5.6), suggesting mixed oxidation states of U after reacting with DO in the absence of FeS (~53% U(VI)).

The FTs of all CSTR samples (Figure 5.7b) show a peak at ~1.9 Å, corresponding to a U-O interatomic distance (R) of ~2.33 Å. The first shell U-O coordination number (CN) of 5.9 (less than the 8 O of a crystalline $UO_{2.00}$) was determined from unreacted synthetic UO_2 and fixed during fitting for all reacted samples, allowing for the comparison of second shell U between samples. The second peak at ~3.6 Å of the FTs was fit with a shell of 3.8 – 4.4 U atoms at ~3.84 Å. In the 160 τ sample, the second-shell CN is not only lower than $UO_{2.00}$ with 12 U(IV) neighbors, but also less than the earlier samples in the time series (~4.4 U).

The decreased second-shell CN suggests that the dissolved UO_2 had smaller particle size than its earlier counterparts, likely due to enhanced UO_2 dissolution after oxygen breakthrough. The solid phase U, however, remained essentially as poorly crystalline, nano-sized UO_2 during the entire inhibition period. The solid phase U is comparable to biogenic uraninite samples reported in previous studies (Singer et al., 2009; Veeramani et al., 2009).

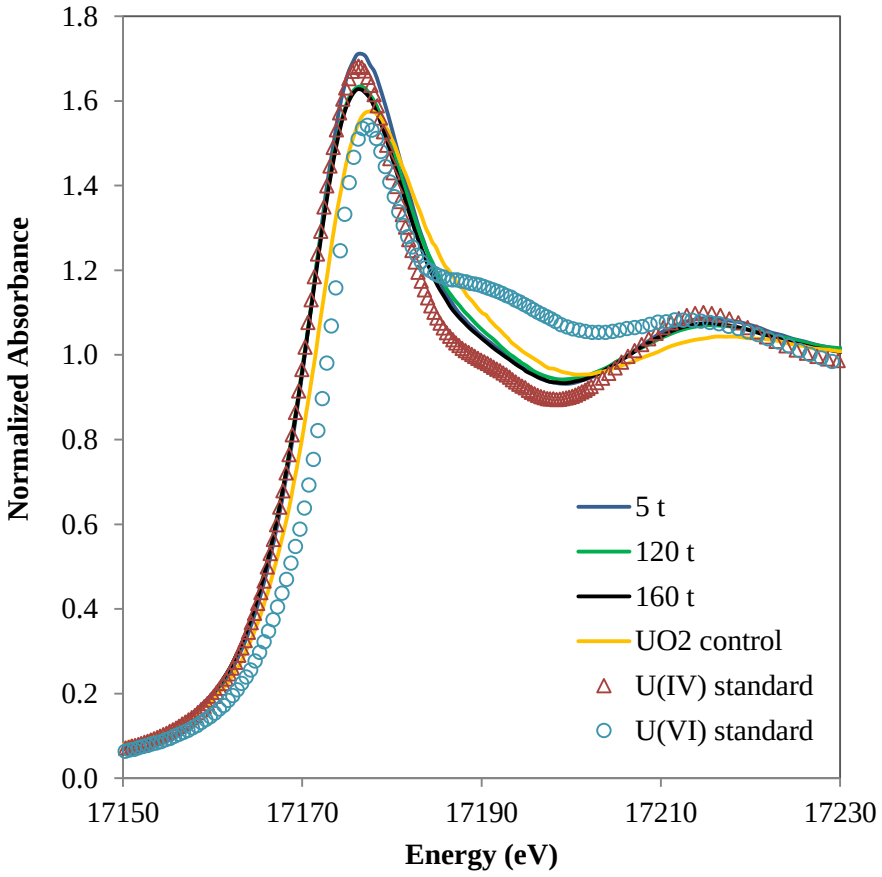

Figure 5.6 Normalized uranium L_{III}-edge XANES spectra of CSTR samples as a function of oxidation residence time in the presence of FeS compared to U(VI) and U(IV) standards (dotted lines). An energy shift to higher eV indicates oxidation of U to higher valence state. An edge position at higher energy and a shoulder at 17190 eV indicates U(VI), whereas an edge position at lower energy and lack of the shoulder indicate U(IV).

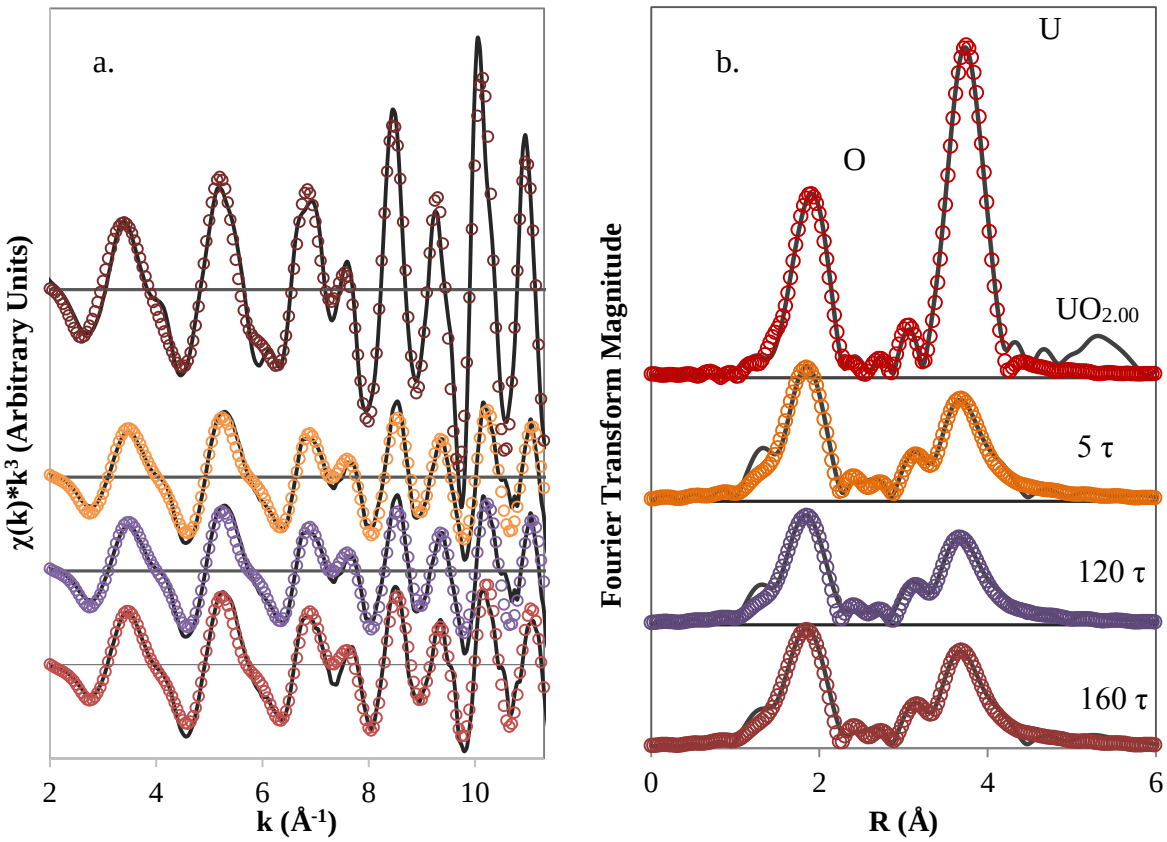

Figure 5.7 U L_{III}-edge spectra for samples collected at 5, 120, and 160 residence times in flow-through experiments in the presence of 18.7 mM FeS at pH 7.1 in comparison with crystalline $UO_{2.00}$. (a) EXAFS spectra (solid line) collected at 77 K with fit to data (open circles) (k range for modeling = 2.0–11 $Å^{-1}$) and (b) corresponding Fourier transforms (solid lines) and fit to data (open circles) uncorrected for phase shifts.

Table 5.3 Uranium and sulfur speciation in selected CSTR samples as calculated by XANES LCF results. The relative concentration of U and S components, i.e., U(IV) and U(VI) are presented as percentages. Relative errors of fitting are given in parentheses.

Element	Species component	5 τ	120 τ	160 τ	control
Uranium	*U(IV) (%) uraninite*	92 (2)	84 (4)	90 (2)	47 (5.4)
	U(VI) (%) Uranyl	8 (2)	16 (4)	10 (2)	53 (5.4)
Sulfur	*S(-II) (%) Mackinawite*	95 (4)	8 (3)	0 (5)	n/a
	S(0) (%) Elemental sulfur*	5 (4)	92 (3)	100 (5)	n/a

* In the fluorescence mode, self-absorption of S_8^0 can cause the attenuation of the XANES absorbance, a phenomenon that has been described as a particle-size effect (Pickering et al., 2001). To improve the fit of XANES LCF, both finely ground S_8^0 (~1–10 μm) and dissolved (1% w/v in toluene) S_8^0 were used as S(0) model compounds.

Table 5.4 Structural parameters extracted from U L_{III}-edge EXAFS data of samples collected from the CSTR. Paths denoted with O1, U1, and O2 stand for first oxygen shell, the first uranium shell, and a second oxygen shell, respectively. The path O=U=O is a multiple scattering path. Estimated errors are given in parentheses.

Sample / Path		**U-O1**	**U-U1**	**U-O2**	**O=U=O**
UO_2 standard	*CN*	8.0	12.0	24.0	8.0
	R (Å)*	2.37 (0.02)	3.87 (0.01)	4.53 (0.04)	4.74 (0.03)
	σ^2 (10^{-3} Å^2)	5 (1)	2 (1)	8 (2)	9 (2)
5 τ	*CN*	5.9 [a]	4.4 (2.2)	8.8 (4.3)	5.9 [a]
	R (Å)*	2.33 (0.01)	3.84 (0.01)	4.31(0.1)	4.65 (0.02)
	σ^2 (10^{-3} Å^2)	6 (1)	2 (3)	22 (21)	13 (2)
120 τ	*CN*	5.9 [a]	4.39 (2.2)	8.8 (4.4)	5.9 [a]
	R (Å)*	2.33 (0.01)	3.84 (0.01)	4.35 (0.09)	4.66 (0.02)
	σ^2 (10^{-3} Å^2)	9 (1)	2 (3)	13 (12)	19 (2)
160 τ	*CN*	5.9 [a]	3.8 (2.0)	7.2 (4.1)	5.9 [a]
	R (Å)*	2.33 (0.01)	3.84 (0.01)	4.27 (0.1)	4.67 (0.02)
	σ^2 (10^{-3} Å^2)	8 (1)	2 (2)	18 (23)	16 (2)

CN: coordination number; *R*: interatomic distance; σ^2: mean-square disorder.
[a] U-O1 in the synthetic UO_2 structure was best fit with 5.9 oxygen atoms. This number was fixed in all sample fits.
* *R* values are the actual bonding distances, which are phase-shifted from the FTs peak positions.

5.3.4 Identification of FeS Oxidation Products

To identify the sulfur products resulting from oxygen scavenging by FeS, dissolved sulfide, thiosulfate, and sulfate concentrations were measured in the effluent. The concentrations of these dissolved sulfur species, however, were found to be negligible in all experiments (section 4.3.2.2), suggesting that S(-II) was predominantly oxidized to solid-phase products in the CSTR.

To determine solid sulfur phases that may have formed by oxidation, *K*-edge XAS data were collected (Figure 5.8). Based on XANES analyses, for all three pH conditions

tested, the primary solid phase sulfur species formed from FeS oxidation was elemental sulfur (Table 5.3). The relative production of S_8^0 appeared to be independent of solution pH and contributed to the overall oxygen scavenging capacity of FeS.

Solid-phase FeS oxidation products remaining in the CSTR were also characterized by XRD. The results indicated that Fe(III) hydroxide solids (i.e., goethite and lepidocrocite) and elemental sulfur formed after FeS was oxidized. Because substantial amounts of Fe(II) were released at lower pH, a lesser amount of Fe(III) products were produced from FeS oxidation by oxygen (< 20% total Fe as Fe(III) at pH 6.1), with lepidocrocite as the dominant Fe(III) phase. In contrast, the direct transformation of FeS to an Fe(III) solid phase at pH 8.1 resulted in the nearly complete conversion of the Fe(II) in FeS to goethite and little loss of Fe(II) from the reactor.

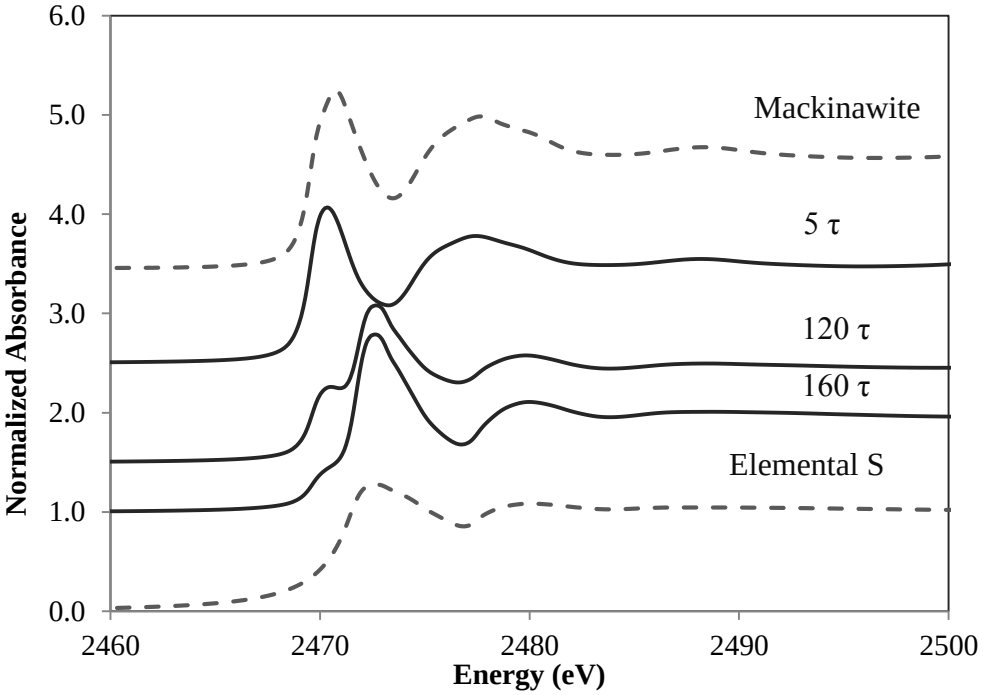

Figure 5.8 Sulfur *K*-edge XANES spectra of CSTR solid phase samples over the course of the FeS oxidation experiments.

5.4 Discussion

5.4.1 Oxidation Limited UO_2 Dissolution

Among the geochemical factors tested in this study, influent DO had the strongest influence on the dissolution rate of UO_2. Results from control experiments showed a 25-fold increase in the dissolution rate from 20×10^{-10} mol g^{-1} s^{-1} when the influent DO level rose from <0.2 mg L^{-1} to 7.8 mg L^{-1} (Figure 5.3b), a clear response to the increasing oxidant concentration. The significant increase of UO_2 dissolution rate, however, was not observed when 18.7 mM FeS was present. The corresponding rate only increased from 5.4×10^{-10} to 15.3×10^{-10} mol g^{-1} s^{-1}. The distinction between the two scenarios points to the high reactivity of FeS for scavenging oxygen in aqueous solution, which left little oxygen to react with UO_2. Indeed, the measured DO concentration (<0.5 mg L^{-1}) in the effluent was considerably lower than in the influent during the inhibition period. Considering the possible diffusion of a small amount of air along the effluent line, the actual DO concentration in the CSTR may have been even lower than the measured values. This high efficiency of oxygen scavenging by FeS was also reported previously in Chapter 4 when oxygen was supplied at a much faster rate (Bi et al., 2013). The results from the present study, however, indicate the incomplete removal of influent DO by FeS, given that UO_2 dissolution rate linearly increased with influent DO concentration.

The mechanism of oxidative dissolution of UO_2 by oxygen has been proposed to occur through a sequence of reaction steps at the UO_2 surface, including the oxidation of U(IV) surface by oxygen, the formation of activated surface complexes, and the subsequent detachment of U(VI) products (Torrero et al., 1997; Shoesmith, 2000). Under low DO and high carbonate and/or calcium concentrations, the formation of U(VI) complexes can result

in the fast detachment of surface U(VI) species (De Pablo et al., 1999; Stewart et al., 2010). Under such conditions, the surface oxidation of UO_2 may be the rate-limiting step (Shoesmith, 2000; Campbell et al., 2011). Alternatively, when the DO concentration is relatively high and surface oxygen is replenished relatively rapidly, the build-up of a UO_{2+x} surface layer is possible, making the detachment step rate-limiting (de Pablo et al., 1996; Torrero et al., 1997; Ulrich et al., 2009).

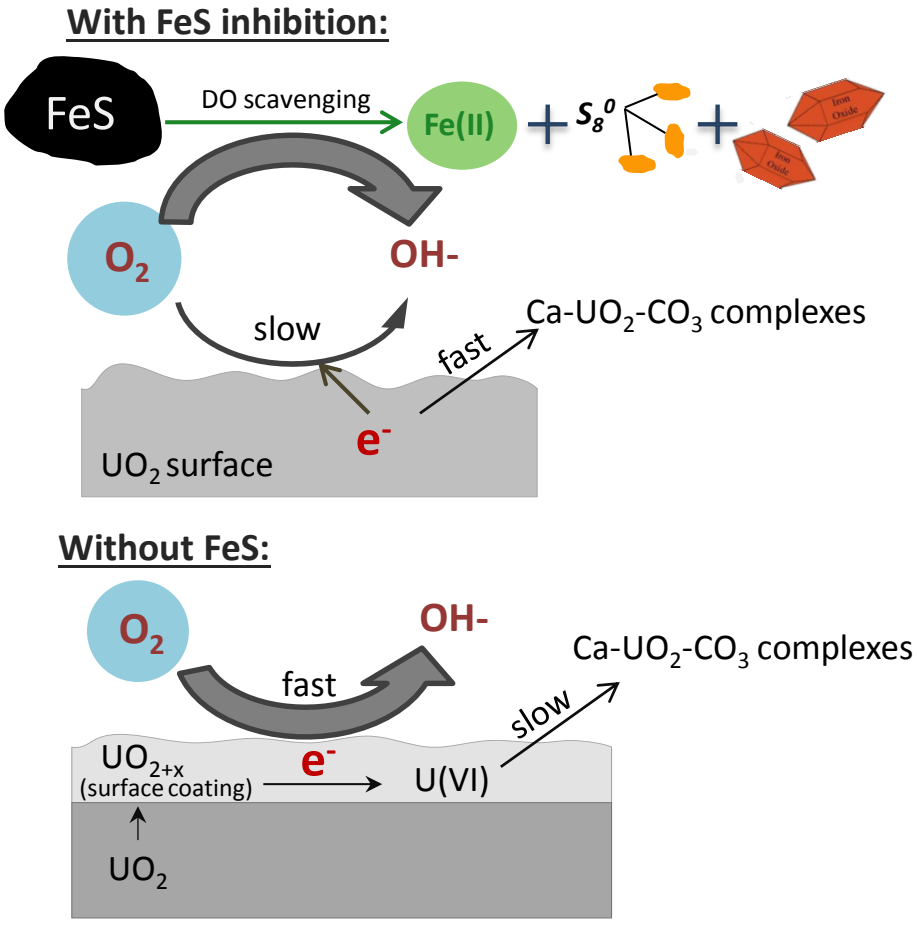

Figure 5.9 The rate-controlling steps of UO_2 oxidative dissolution by dissolved oxygen in the presence and absence of mackinawite.

The FeS concentration dictates the DO levels in the simulated groundwater solution, and therefore it influences the UO_2 oxidative dissolution mechanism and the corresponding rate-limiting process. At a sufficiently high FeS concentration (18.7 mM), XAS analyses showed no evidence of a U(VI) surface coating on reacted UO_2 samples. This finding is consistent with a rate-limiting UO_2 surface-oxidation step which determines the overall dissolution rate. Under these conditions, the detachment of surface-bound complexes (as dissolved $Ca\text{-}UO_2\text{-}CO_3^{2-}$ complexes) would occur faster than surface oxidation, preventing U(VI) accumulation (Figure 5.9). In contrast, partially oxidized UO_2 was revealed by XANES spectrum in the control reactor when exposed to relatively high influent DO in the absence of FeS. Under these conditions, the detachment of surface-bound U(VI) into solution may become rate limiting, although facilitated by carbonate and calcium ions. Similarly, Ulrich et al. (2009) proposed the detachment of U(VI)-carbonato complexes as rate-limiting in the presence of carbonate, since the oxidation of surface U(VI) would be relatively fast under mildly oxidizing conditions (DO = ~0.6 mg L^{-1}). By using a strong oxygen scavenger such as FeS, the rate-limiting step of UO_2 dissolution can be shifted from U(VI) detachment under high DO levels in absence of FeS, to surface-oxidation limited when DO is significantly removed.

The oxidation-limited dissolution of UO_2 also showed a pH-independent rate in the presence of FeS in this study. Similar results have been reported for UO_2 dissolution at higher oxygen concentrations at pH >6, where proton-promoted UO_2 dissolution is at the lowest rate (Torrero et al., 1997). In most groundwater conditions, pH is unlikely to influence UO_2 dissolution rates, unless it substantially changes carbonate speciation under oxidizing conditions. In the present study, the total dissolved inorganic carbonate concentration ranged

from 1–10 mM depending on solution pH and P_{CO2}. Bicarbonate is the predominant carbonate species from pH 6.1 to 8.1 with a concentration in great excess to dissolved U(VI). Therefore, the rate of surface U(VI) detachment is likely similar in the pH range studied, which is faster than surface oxidation in the presence of FeS.

5.4.2 pH-Dependent FeS Dissolution

Under the flow-through conditions of the present study, FeS is shown to be an excellent scavenger of DO, with FeS itself undergoing significant oxidation over time. At pH 7.1, Fe(III) hydroxide solids and elemental sulfur are the final oxidation products, consistent with the results in Chapter 4 and previous studies (Burton et al., 2009; Jeong et al., 2010a; Bi et al., 2013). Among aqueous species, only Fe(II) was detectable as a result of FeS dissolution. Assuming FeS is the predominant reductant for oxygen during the inhibited UO_2 dissolution period, the time required for complete FeS oxidation can be estimated based on the influent DO concentration, flow rate, and the oxidation products. The estimated oxidation time for FeS agrees reasonably well with the observed time for complete FeS oxidation by tracking soluble Fe(II) (Table 5.5).

The pH-dependent release of dissolved Fe(II) in oxic groundwater results in a loss of reducing capacity of FeS for DO, which consequently decreased the duration of the FeS inhibition of UO_2 oxidation. For example, a considerably shorter inhibition period of UO_2 dissolution was observed at pH 6.1 (~120 τ) compared to that at pH 8.1 (~190 τ), in which 81% and 0.2% of total Fe were released at the corresponding pH. Under acidic pH, FeS underwent significant dissolution followed by the slow precipitation of Fe(III) hydroxides. The aqueous Fe(II) species only slowly oxidized at pH < 6.5 (Morgan and Lahav, 2007), and

contributed little to the overall oxygen scavenging in the reactor. At basic pH, the structural Fe(II) of FeS oxidized directly to produce solid phase Fe(III) products. The complete solid-phase conversion of Fe(II) to Fe(III) with little Fe(II) dissolution allowed for nearly complete utilization of the FeS reducing capacity, and thus extended the inhibition period of UO_2 dissolution. An oxidized hydrophobic sulfur-rich layer with nanosize pores likely forms on the FeS surface during oxidation, which may facilitate oxygen diffusion or electron transfer to enhance the rate of oxygen removal by FeS (Chirita, 2009). A similar pH-dependent oxidation mechanism has been reported in a batch study of FeS oxidation (Jeong et al., 2010a). Given the longest inhibition of oxidative UO_2 dissolution by FeS occurred at a basic pH, these conditions would be preferred over acidic conditions for prolonging the protective nature of FeS in groundwater.

Table 5.5 Groundwater compositions in equilibration with $CO_2/O_2/N_2$ gas mixtures for pH 6, 7, and 8 experiments.

Experiment code	*pH*	*FeS* (mM)	*DO* (mg L^{-1})	Observed oxidation time for FeS (τ)	Calculated time for FeS oxidation (τ) [§]	Observed UO_2 inhibition time (τ)
1a	6.1	18.7	1.8	163	166.5	120
1b	6.1	18.7	1.8	158	165.8	115
2a	7.1	18.7	1.8	185	207	168
2b	7.1	18.7	1.8	190	208	158
3a	8.1	18.7	1.8	\ *	228.3	183
3b	8.1	18.7	1.8	\ *	228.5	195
4a	7.1	56.8	1.8	610	686	490
5a	7.1	4.8	1.8	63	59.5	48
5b	7.1	4.8	1.8	60	60	49
6a	7.1	1.2	1.8	12.4	13.7	9
7a	7.1	18.7	7.8	59	56.8	53
7b	7.1	18.7	7.8	55	56.6	50

[§] Calculation is based on the reaction:

$$FeS(s)+\frac{2+x}{4}O_2+\frac{x}{2}H_2O= xFeOOH(s)+ (1-x)\ Fe^{2+}+\frac{1}{8}S_8^0(s)$$

where x is a value between 0 and 1, measured as a fraction of FeS undergoing dissolution to produce dissolved Fe(II)

Assuming the effluent [Fe(II)] reflects the relative FeS concentration remaining in the CSTR, the disappearance of detectable Fe(II) should indicate the complete oxidation of FeS solids. Because the hydraulic residence time (τ) of Fe(II) in the reactor is relatively short (~25 min), the error in using this method for estimating FeS oxidation duration should be small.

[*] the oxidation time for FeS cannot be estimated by tracking the effluent Fe(II) concentration due to lack of detectable Fe(II) at pH 8.

5.4.3 Limitation of Oxygen Scavenging

In a flow-through system with a constant supply of oxidant, FeS eventually becomes completely oxidized. For a given pH and DO, the capacity of oxygen scavenging by FeS is directly determined by its concentration in the flow-through system. Higher FeS concentrations always leads to longer inhibition periods. However, the actual inhibition period for UO_2 dissolution is notably shorter than the time observed for complete FeS oxidation under all experimental conditions (Table 5.5). For example, the observed inhibition period is ~160 τ for 18.7 mM FeS under 1.8 mg L^{-1} DO and pH 7.1, while it takes ~190 τ to completely oxidize FeS. This disparity may indicate that when 10 – 20% of the total nano-FeS particles remain, the kinetics of oxygen consumption by FeS become too slow to keep DO low enough for inhibiting UO_2 dissolution.

With increasing FeS concentration, UO_2 dissolution rate begins to slow down asymptotically (Figure 5.3c) and reaches a minimum of 5.3×10^{-10} mol g^{-1} s^{-1} at the highest FeS concentration (56.8 mM). This rate is only slightly lower than 8.0×10^{-10} mol g^{-1} s^{-1} at 18.7 mM FeS, and is comparable to the reported rates under similar anoxic conditions using nanoparticulate biogenic and synthetic UO_2 (Ulrich et al., 2008; Wang et al., 2013). Therefore the inhibited UO_2 dissolution rate may not decrease much below 5.3×10^{-10} mol g^{-1} s^{-1}, even with higher FeS concentrations. It should be noted that the UO_2 dissolution rate obtained from the anoxic control experiment (20×10^{-10} mol g^{-1} s^{-1}) was higher than that in the presence of FeS. This result may be attributed to residual oxygen (<1000 ppm) in the anaerobic glove bag surrounding the reactor, which may have diffused into the CSTR and reacted with UO_2. When present, FeS would consume oxygen in the system until it is depleted. Therefore, the lower dissolution rate in the presence of FeS may simply be the

result of lowering the DO concentration in the CSTR, rather than a direct interaction of FeS with UO_2 to keep UO_2 surface reduced. Under such low DO conditions, surface U(IV) oxidation would be rate limiting.

At low FeS concentrations, DO is not sufficiently removed by FeS and surface oxygen concentrations are high. The result from the 1.2 mM FeS experiment shows a much higher UO_2 dissolution rate of 43×10^{-10} mol g^{-1} s^{-1} and a shorter inhibition period (~9 residence times). At the measured effluent DO concentration of ~0.9 mg L^{-1}, UO_2 oxidation takes place more rapidly, with the rate-limiting step likely the detachment of surface complexes rather than surface oxidation as noted previously. To ensure the lower rates associated with surface oxidation-limited UO_2 dissolution, low DO levels (<0.5 mg/L) must be maintained, which depends on having sufficient FeS present. The amount of FeS necessary to keep DO levels low depends on the oxygen supply rate, with higher FeS concentrations needed at higher DO concentrations and/or a faster flow rate.

5.4 Conclusions

This study demonstrates that a surface-oxidation step likely controls the overall UO_2 dissolution rate in the presence of synthetic nano-FeS when effective oxygen scavenging by FeS lowers the DO to rate-limiting levels. Because nanocrystalline FeS is readily formed under sulfate reducing conditions (Abdelouas et al., 1999b; Rickard and Morse, 2005), FeS may provide practical protection of UO_2 in the field when oxic conditions are not prevalent. A sufficiently high concentration of FeS is, however, required to ensure low DO concentration when oxygen intrusion events occur. The capacity of FeS for removing DO from groundwater is directly governed by the amount of FeS exposed to an oxic flow under

oxygen-limited conditions. Geochemical factors, such as pH and DO levels, also affect the extent of the inhibition period. Alkaline pH promotes surface-mediated FeS oxidation, which provides greater oxygen scavenging capacity and a longer period of protection. In the absence of natural pH buffering, a change of pH conditions from slightly basic to acidic can induce significant FeS dissolution and decrease the inhibition period of low U release. In anoxic subsurface environments, diffusion-limited oxygen supply from oxic zones, in addition to oxygen scavenging by FeS, may substantially inhibit uraninite dissolution and prolong its stability. The transformation of FeS to more stable iron sulfide phases, such as pyrite, however, may limit the oxygen removal efficiency in the field.

Recent investigations of U immobilization by bioremediation report a close association of reduced U(IV) with FeS in the field; however, the dominant initial U phase was monomeric U(IV) bound to biomass rather than UO_2 (Fletcher et al., 2010; Bargar et al., 2013). Given that biomass-complexed U(IV) may be more susceptible to oxygen oxidation than uraninite (Cerrato et al., 2013), it is unclear whether nano-FeS produced *in situ* would provide the same effectiveness in inhibiting monomeric U(IV) oxidative dissolution as for UO_2. Future research should investigate the potential of FeS as a competitive oxidant scavenger in the presence of biologically reduced U(IV) species.

After the inhibition period, the depletion of FeS may eventually expose reduced UO_2 solids to oxygen, causing the dissolution of UO_2 and transport of U(VI). The following study seeks to understand the impact of FeS oxidation products on UO_2 dissolution after oxygen breakthrough and the rate-limiting mechanism of UO_2 dissolution during the suboxic-oxic transition.

Chapter 6

Surface Passivation Limited UO_2 Oxidative Dissolution upon FeS Depletion

6.1 Introduction

In situ treatment of uranium (U)-contaminated soils and groundwater often rely on the effective reduction of soluble U(VI) species to sparingly soluble U(IV) solid phases through chemical and biological processes (Lovley et al., 1991; Behrends and Van Cappellen, 2005; Hua et al., 2006). After active bioremediation is halted, naturally-occurring mackinawite (FeS) may provide an additional reservoir of reducing capacity for U(VI) immobilization and retard uraninite reoxidation upon oxygen intrusion (Abdelouas et al., 1999a; Bargar et al., 2013; Bi and Hayes, 2013; Bi et al., 2013).

While effectively scavenging oxygen, FeS undergoes significant oxidation-induced transformation, generating various iron and sulfur products depending on geochemical conditions, including dissolved Fe(II), goethite, lepidocrocite, elemental sulfur, and sulfate (Burton et al., 2009; Chirita, 2009; Jeong et al., 2010a; Bi et al., 2013). These oxidation products of mixed oxidation states are also redox reactive species, which may further impact the reoxidation of reduced U(IV) solids upon persistent oxygen intrusion.

Dissolved Fe(II) species, produced as a result of FeS dissolution, may contribute to low levels of dissolved U by abiotic reduction of U(VI). Sorbed Fe(II) on synthetic Fe(III) oxides and natural sediments has been demonstrated to abiotically reduce U(VI) in a near-neutral pH range (Liger et al., 1999; Fox et al., 2013). Reduction of U(VI) by soluble Fe(II) was reported to be thermodynamically favorable by Du et al. (2011) when reactant and product concentrations are in the proper range. Before complete FeS oxidation, sorbed Fe(II) by Fe(III) hydroxides may facilitate the removal of dissolved U(VI) species and prevent UO_2 surface passivation.

In contrast, Fe(III) hydroxides, e.g., goethite and lepidocrocite, formed during mackinawite oxidation, may enhance the oxidative dissolution of UO_2 by facilitating electron transfer at particle contact points between UO_2 and Fe(III) particles. Sani et al. (2005; 2011b) and Ginder-Vogel et al. (2006) showed that iron hydroxides can oxidize U(IV) solids under reducing conditions, although the relationship between the type and amount of Fe(III) on the rate of U reoxidation has not been fully examined.

Batch and flow-through experiments in Chapters 4 and 5 show that the oxidative dissolution rate of UO_2 at pH 7 increased in response to elevated DO concentrations after the period of inhibited dissolution by FeS (Bi et al., 2013). The release rate of dissolved U(VI) after DO breakthrough was even faster than that observed in control experiments where FeS was absent. One hypothesis to explain the enhanced dissolution is oxidation of uraninite by Fe(III) oxidation products of FeS, which may either serve directly as an oxidant for U(IV) or facilitate electron transfer at particle contact points (Williams and Scherer, 2004; Kato et al., 2010). Another possibility is that FeS remaining during inhibited oxidative dissolution may

reduce passivation or disrupt layers of U(VI) that form on UO_2 surface, allowing for a rapid oxidative attack of U(IV) after oxygen breakthrough.

It is still unclear however, which mechanism causes the enhanced dissolution of UO_2 after FeS depletion in an oxic groundwater system, and the extent to which the dissolution rate of UO_2 may increase during this suboxic to oxic transition period. Given the common association of iron sulfides with reduced U(IV) phases in bioremediation sites (Bargar et al., 2013), the abiotic interactions of uraninite and mackinawite may play important role in controlling the long-term stability of U(IV) upon oxygen intrusion. Unless sulfate reducing conditions are promptly restored after oxygen intrusion, the stability of U(IV) in the redox transition zones may be affected. Upon consumption of the FeS, the oxygen scavenger, U remobilization in the subsurface will increase, but the extent will likely be controlled by the stability of the passivation layer that forms prior to the DO breakthrough. Therefore, the environmental risks caused by subsequent U remobilization should be carefully evaluated.

The objective of the present study was to examine the influence of FeS on UO_2 oxidative dissolution behavior after oxygen breakthrough during the suboxic-oxic transition and characterize the passivation layer that forms on UO_2 during dissolution. Using flow-through systems, the release rate of dissolved U(VI) was determined as a function of pH, DO and FeS concentrations. The surface passivation layer that may form as a function of these conditions was examined by XAS and XPS. Additionally, the FeS reaction products, i.e., Fe(III) hydroxides and aqueous Fe(II), were examined by XAS for their potential influence on UO_2 oxidative dissolution. The results of this study contribute to the understanding of the role of passivation layers on the long-term stability of reduced U(IV) during periods of persistent oxygen intrusion in groundwater environments.

6.2 Experimental Methods

6.2.1 UO_2 Oxidative Dissolution with FeS

The oxic flow-through experiments were conducted with 50 mL CSTRs (Millipore 8050) under varied pH, DO influent concentration, and FeS content. At the beginning of the experiment, a CSTR reactor was loaded with ~0.48 mM UO_2 suspension and FeS at various concentrations to provide the desired FeS:UO_2 ratio. All feed solutions were constantly purged with custom $CO_2/O_2/N_2$ gas mixtures and prepared with MilliQ water containing 0.4 mM KCl, 2.0 mM $CaCl_2$, and different $NaHCO_3$ concentrations to achieve a final pH of 6.1, 7.1, or 8.1. The DO of effluent solution was constantly monitored for tracking the stage of FeS oxidation. When DO breakthrough occurred, FeS had been substantially oxidized and transformed to Fe(III) oxides and elemental sulfur, depending on solution pH. The supply of oxic groundwater was then continued for an additional 100 residence times ($\tau \approx 25$ min) to allow for rapid oxidative dissolution of UO_2. The effluent samples were collected frequently after DO breakthrough until steady-state dissolution of UO_2 was re-established or more than > 50% of total UO_2 had dissolved.

Flow-through experiments were also conducted to examine the influence of low FeS concentration on UO_2 oxidative dissolution at pH 7. The CSTR reactors containing 4.8 mM FeS suspension were oxidized by artificial groundwater with an influent DO of 1.8 mg/L. At selected time points, UO_2 solids were then added to the oxidized FeS suspension, resulting in UO_2 interactions with different concentrations of remaining FeS. Effluent samples were collected after UO_2 was added and measured for DO, total dissolved Fe and U concentrations using ICP-MS.

6.2.2 Oxidation of UO_2 by Fe(III) Oxides.

To study the potential of Fe(III) hydroxides for oxidizing UO_2 under oxic conditions, flow-through experiments were conducted in the CSTR using a different matrix of Fe(III) solids. Mixed Fe(III) hydroxides were prepared by directly oxidizing FeS suspension at pH 7 with a $CO_2/O_2/N_2$ gas mixture in a 250 mL batch reactor. The FeS oxidation products were previously characterized to consist of goethite, lepidocrocite, and elemental sulfur (Bi et al., 2013). The Fe(III) hydroxides were added to the CSTR at a total Fe concentration of 16 mM with 0.5 mM UO_2 for a total volume of 50 mL. The influent solution was constantly sparged by the $CO_2/O_2/N_2$ gas mixture to maintain the influent solution at pH 7 and DO of 1.8 mg/L. The effluent solution was periodically sampled and analyzed for total dissolved Fe(II) and U concentrations. Similar flow-through experiments were also conducted using ~15 mM synthetic two-line ferrihydrite as a potential oxidant. Anoxic control experiments were performed inside an anaerobic chamber to provide a baseline UO_2 oxidation rate in the presence of Fe(III) solids under oxygen-free conditions.

6.2.3 UO_2 Reaction with Surface-Adsorbed Fe(II)

To test the role of Fe(II) in affecting the formation of UO_2 surface passivation layer, flow-through experiments were conducted by reacting UO_2 with soluble and sorbed Fe(II) by Fe(III) oxides. A UO_2 suspension (~0.5 mM) was added to the CSTR alone or in combination with 16 mM Fe(III) oxidation products (described in section 6.2.2), which then reacted with an oxic groundwater solution containing ~0.1 mM $FeCl_2$. The influent solution was prepared inside an anaerobic chamber and sparged with the $CO_2/O_2/N_2$ gas mixture to achieve a DO concentration of 1.8 mg/L and pH 6. The solution pH was chosen to prevent Fe

oxidation and precipitation during the course of flow-through experiments. Anoxic experiments were conducted at both pH 6 and 7 using Fe(II)-containing groundwater solution in the presence and absence of Fe(III) solids to provide a baseline of UO_2 dissolution in the absence of DO.

6.2.4 Carbonate Extraction of FeS-Reacted U

To quantify the U(VI) and labile U(IV) products generated during UO_2 oxidative dissolution in the presence of FeS, suspension samples were taken during the course of pH 7 oxidation experiments for carbonate extraction. To collect the solids and prevent oxidation during sampling, the solid suspension was briefly transferred to the anaerobic chamber and centrifuged. The solids were then collected and reacted with 10 mL 0.5 mM anoxic $NaHCO_3$ solution at pH = ~7.8 in 20 mL glass crimped vials. The U extraction was performed for 21 hr on an end-over-end rotator in the anaerobic chamber. The extraction procedure ensured that all weakly bound U(VI) species were removed from the solid phase. After 21 h, the suspension pH was measured, and then the suspension was filtered using 0.1 μm nylon syringe filter (Watson). Subsequently, the filtered solution was measured for total dissolved U concentration by ICP-MS. Carbonate extractions were also conducted for solids collected in pH 6 and 8 flow-through experiments after DO breakthrough to assess the impact of pH on UO_2 oxidation products.

6.2.5 Dissolution Rate Calculation

After DO breakthrough, the UO_2 dissolution rate was calculated from the dissolved U concentration in effluent solution. When the U(VI) concentration reached steady-state, the

oxidative dissolution rate of UO_2 (R_m) (mol g^{-1} s^{-1}) by oxygen was calculated using the following equation (Eq. 6.1):

$$R_m = \frac{[U]_{ss} \times Q}{V \times [UO_2]} \qquad (6.1)$$

where R_m (mol s^{-1} g^{-1}) is mass-normalized oxidative dissolution rate of UO_2, Q (L s^{-1}) the flow rate, V(L) the reactor volume, $[U]_{ss}$ (mol L^{-1}) the steady-state concentration of total dissolved uranium, and $[UO_2]$ (g L^{-1}) the mass concentration of uraninite in the reactor. Due to the unknown degree of aggregation and thus the inherent uncertainty in the surface area of UO_2, surface-area normalized rates (mol m^{-2} s^{-1}) were not estimated in this study. The steady-state effluent U concentrations were typically based on the average of at least 6 effluent samples. Error bars represent two standard deviations of the rate calculated at steady-state, reflecting the 95% confidence interval. The mass of UO_2 at steady-state dissolution was adjusted for solid loss in the rate calculations.

When experiments showed a peak of U concentration after DO breakthrough without reaching a steady-state, this indicated that UO_2 dissolution was occurring at a fast rate, resulting in significant UO_2 solid loss. In these cases, the UO_2 oxidative dissolution rate could not be derived from Equation 6.1. Instead, the dissolution rate was estimated by the amount of total U released into the effluent within a given time. In these experiments, the cumulative total U release was calculated based on the measured U concentration and flow rate, and plotted against the reaction time. After DO breakthrough, total released U increased linearly until a substantial UO_2 loss had occurred. The dissolution rates for UO_2 were obtained by subjecting the linear portion of the plots to regression analysis. For the rate analysis, typically more than eight points were utilized, resulting in R^2 values greater than 0.98 for all least-square fits. Regression analysis also yielded 95% confidence intervals for

error estimates. This method of rate estimation was also used for experiments of steady-state UO_2 dissolution and showed comparable values with that calculated by Equation 6.1.

6.2.6 Solids Characterization

Solid samples taken from flow-through experiments at pH 6, 7, and 8 were characterized by XAS and XPS to determine the redox state and stoichiometry of uranium in the bulk and near the surface of UO_2 particles, respectively. UO_2 particles were also examined by TEM to identify oxidation products and particle size.

XAS analyses of wet pastes of the solids from the CSTR were performed at the Stanford Synchrotron Radiation Lightsource (SSRL) as previously described in Chapter 3. Uranium L_{III}-edge absorption spectra were collected in fluorescence mode at Beamline 4-1 or 11-2 using a 13- or 100-element Ge detector at a low temperature (77 K). XAS data were later subjected to X-ray absorption near edge structure (XANES) and extended X-ray absorption fine structure (EXAFS) analyses using SixPACK and IFEFFIT code.

Suspension samples dried in the anaerobic chamber were mounted on double-sided Cu tape for XPS analysis. XPS spectra were collected on a Kratos Axis Ultra XPS using a monochromated Al-K_α X-ray source (1486 eV). Region scans were obtained for U(4f), Fe($2p_{3/2}$), O(1s) peaks and analyzed using the procedures described in Chapter 3.

TEM images were obtained using a JEOL 2010F analytical electron microscope (AEM) operated at 200 kV. TEM analysis included conventional bright-field (BF) imaging coupled with energy dispersive X-ray (EDX) with the spatial resolution of~1.7 Å, high resolution-transmission electron microscopy (HR-TEM), and selected area electron diffraction (SAED).

6.3 Results

6.3.1 UO_2 Dissolution after DO Breakthrough

In the presence of FeS, the oxidative dissolution of UO_2 was initially inhibited, resulting in low concentrations of dissolved U until DO breakthrough. Immediately after the inhibition period, dissolved U concentration increased rapidly to peak values in response to increasing DO concentrations at pH 7 (Figure 6.1a). Because steady-state UO_2 dissolution did not occur after DO breakthrough, the dissolution kinetics was estimated by plotting the cumulative U(VI) release as a function of time (Figure 6.1b). The slope of the linear region indicated that UO_2 dissolution was faster in systems with FeS initially present compared to that in the absence of FeS at pH 7, and the rate increased with increasing initial FeS concentration (Figure 6.2a). In comparison, UO_2 dissolution in the absence of FeS reached steady state at ~4.0 μM $[U]_{diss}$ under comparable conditions (Figure 5.2). The calculated rates of UO_2 dissolution at pH 7 in the presence and absence of FeS are summarized in Table 6.1.

Relative to the control without FeS, an enhancement in dissolution rate of UO_2 was only observed for pH 7 experiments. At pH 6 and 8, steady-state dissolution of UO_2 were slowly re-established after DO breakthrough without a U peak. The oxidative dissolution rate of UO_2 was found to be similar to the control at pH 6 but slower than the control at pH 8 after DO breakthrough (Figure 6.2b). The variation in rate implies complex and potentially changing mechanisms of UO_2 dissolution with pH during the suboxic-oxic transition.

At pH 7 and a FeS initial concentration of 18.7 mM, UO_2 showed a similar dissolution rate at influent DO concentrations of 1.8 mg/L and 7.8 mg/L (within a factor of two). While the dissolution rate at a DO concentration of 1.8 mg/L was faster than in the control experiments under comparable conditions, the rate was similar to the control at DO of

7.8 mg/L. During the faster oxidative dissolution of UO_2 after the inhibition period, the effluent DO concentration increased rapidly in response to the exhaustion of FeS. The measured effluent DO concentration after breakthrough increased faster at an influent DO of 7.8 mg/L than for the system containing a DO of 1.8 mg/L (Figure 6.3). In comparison, the UO_2 dissolution rate increased 25-fold from 0.2×10^{-8} mol g^{-1} s^{-1} in the absence of FeS when the influent DO level went from < 0.2 mg L^{-1} to 7.8 mg L^{-1}, indicating a clear response to the increasing oxidant concentration.

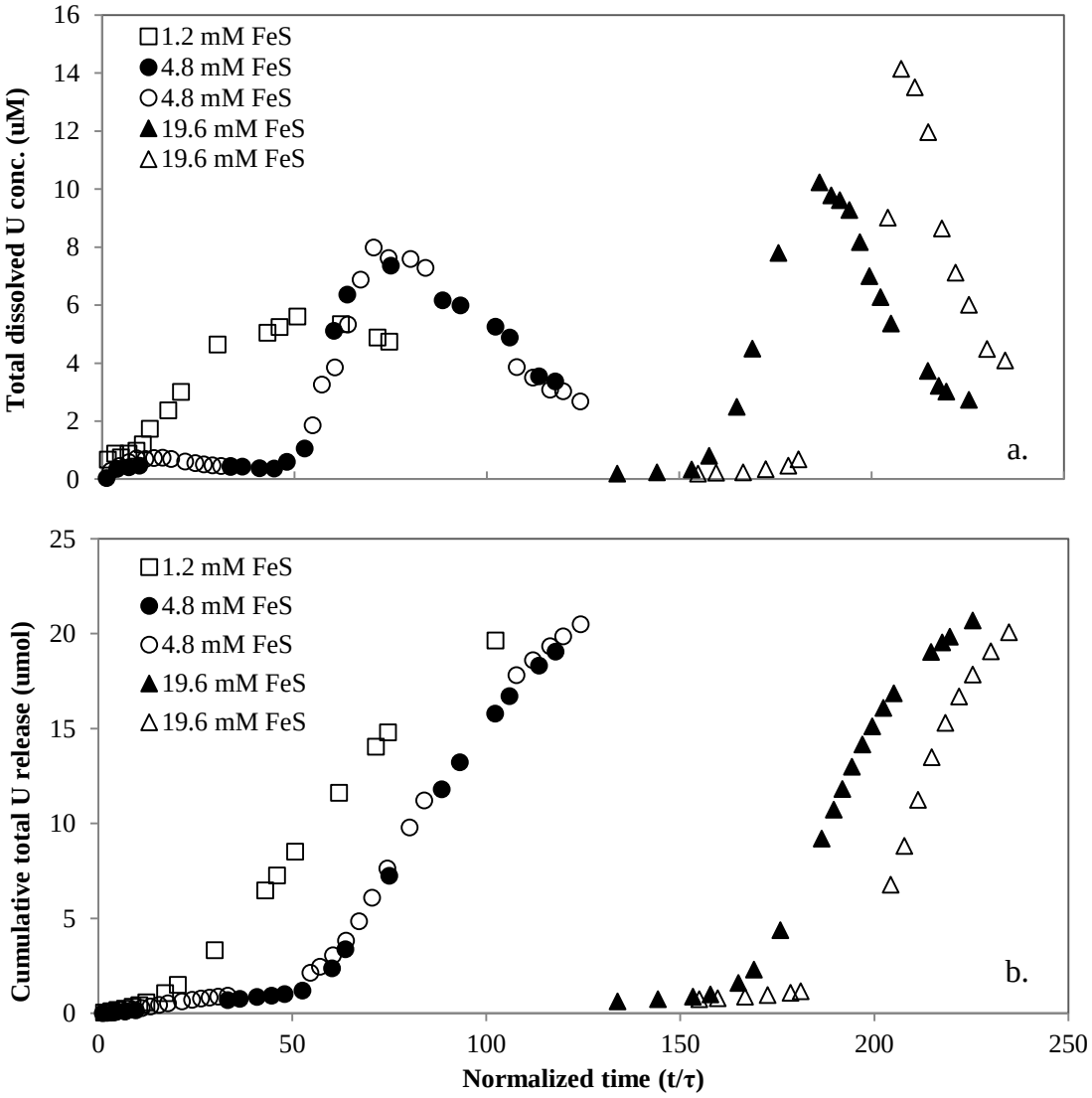

Figure 6.1 (a) UO_2 dissolution profiles in the flow-through experiments at various FeS concentrations. (b) The cumulative release of dissolved U in the flow-through experiments calculated based on the UO_2 dissolution profiles in (a). Replicates are represented by the filled vs open symbols. Influent groundwater solution composition: 8.0 mM $NaHCO_3$, 0.4 mM KCl, and 2.0 mM $CaCl_2$, 1.8 mg L^{-1} DO, and pH 7.

Table 6.1 Experimental UO_2 dissolution rates normalized to mass (R_m) obtained under various combinations of oxidizing conditions and water compositions[§].

Exp. ID	$[UO_2]$ (mM)	[FeS] (mM)	pH	DO (mg L^{-1})	DIC* (mM)	Flow rate (mL min^{-1})	$R_m \times 10^{-8}$ mol g^{-1} s^{-1}
Variation of pH							
1a	0.48	18.7	6	1.8	2.5	1.83	2.06
1b	0.48	18.7	6	1.8	2.5	1.98	2.18
2a	0.48	18.7	7	1.8	10	1.88	4.20
2b	0.48	18.7	7	1.8	10	1.96	5.40
3a	0.48	18.7	8	1.8	1	1.82	1.21
3b	0.48	18.7	8	1.8	1	1.91	1.25
Control	0.48	\	6	1.8	2.5	1.87	1.89
Control	0.48	\	6	1.8	2.5	1.89	1.95
Control	0.48	\	7	1.8	10	1.91	2.06
Control	0.48	\	7	1.8	10	1.82	1.99
Control	0.48	\	8	1.8	1	1.81	2.23
Control	0.48	\	8	1.8	1	1.95	2.28
Variation of FeS							
4a	0.48	4.8	7	1.8	10	1.87	2.92
4b	0.48	4.8	7	1.8	10	1.85	2.95
5a	0.48	1.2	7	1.8	10	1.85	2.39
Variation of DO							
6a	0.48	18.7	7	7.8	10	1.84	2.91
6b	0.48	18.7	7	7.8	10	2.15	5.58
Control	0.48	\	7	7.8	10	2.24	3.46
Control	0.48	\	7	7.8	10	2.19	3.60
Control	0.48	\	7	<0.1	10	1.85	0.2

[§] Groundwater compositions were previously provided in Table 5.1.

* Dissolved inorganic carbon calculated using Visual MINTEQ at equilibrium with $CO_2/O_2/N_2$ gas mixtures.

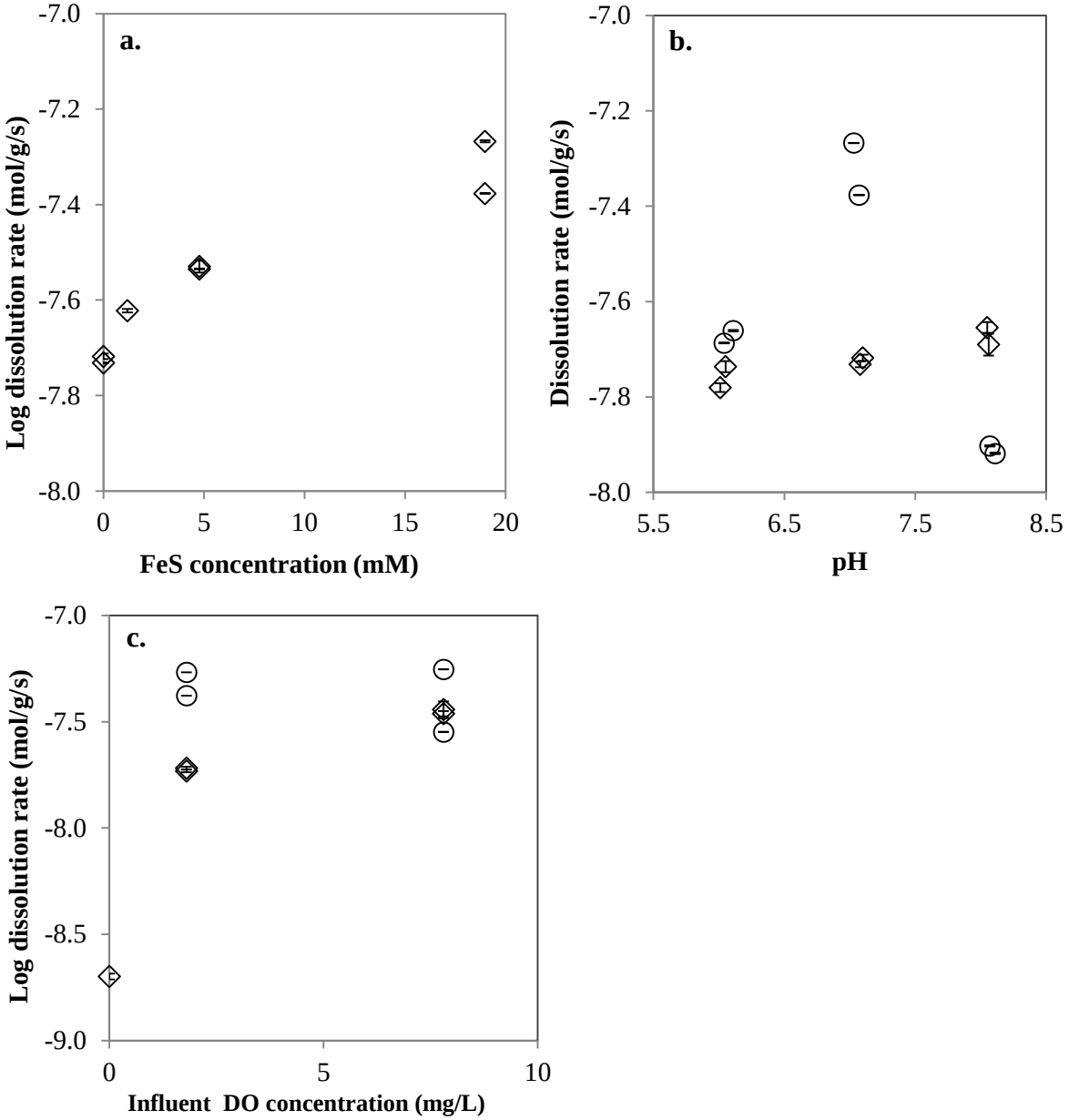

Figure 6.2 UO_2 dissolution rates (mol g^{-1} s^{-1}) estimated from cumulative dissolved U released in the presence (○) and absence (◊) of FeS as a function of (a) FeS concentration (g/L) at pH 7; (b) solution pH at 18.7 mM FeS and influent DO of 1.8 mg/L; and (c) influent DO concentration (mg L^{-1}) at 18.7 mM FeS and pH 7.

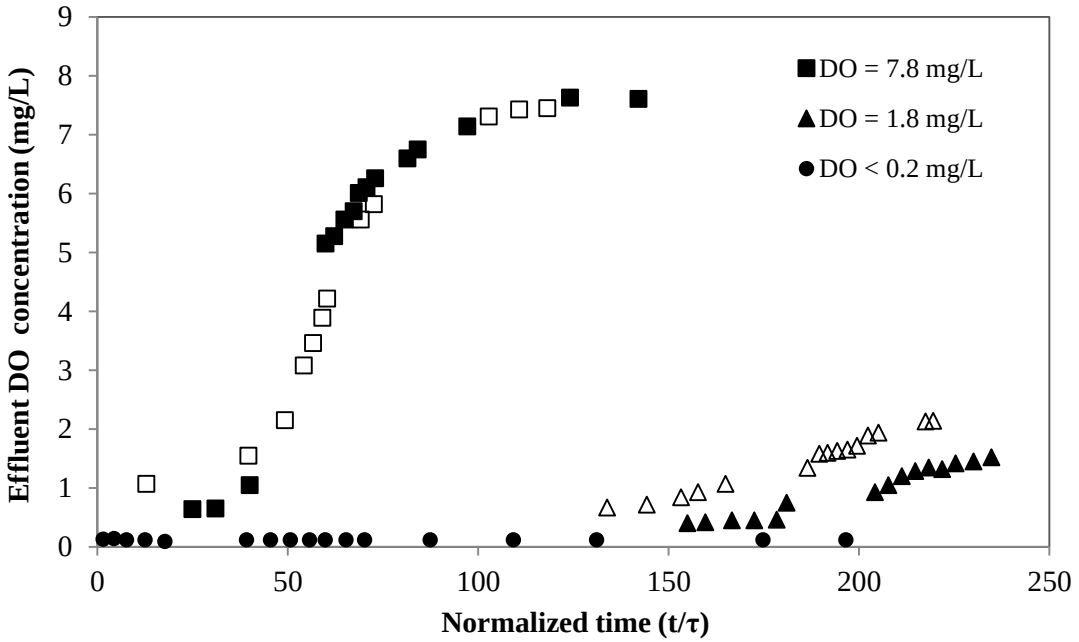

Figure 6.3 The DO concentration profiles as a function of time during the oxidative dissolution of UO_2 in the presence of 18.7 mM FeS in pH 7 groundwater. Replicates are represented by the filled vs open symbols.

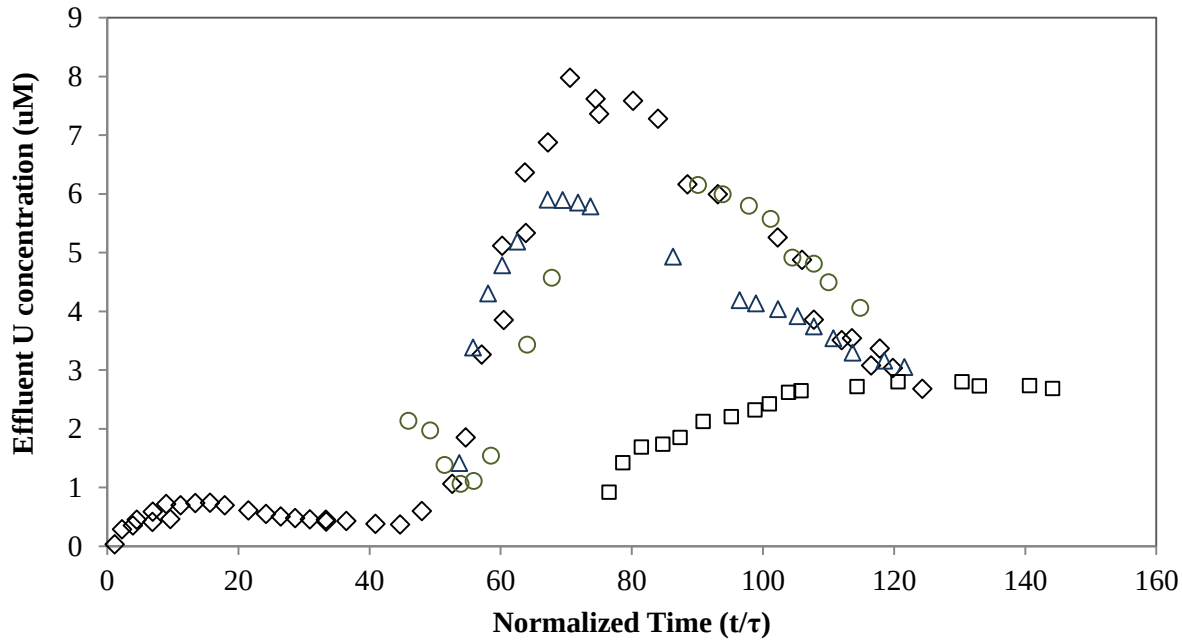

Figure 6.4 UO_2 dissolution profiles in the flow-through experiments when UO_2 solids were added at different stages of FeS oxidation: 0 τ (◊); 46 τ (○); 52 τ (Δ); and 75 τ (□). Experimental condition: initial FeS 4.8 mM, influent DO = 1.8 mg/L, pH = 7.1.

By adding UO_2 to depleting FeS, the impact of low concentration FeS on UO_2 oxidative dissolution was examined. When UO_2 was added at 46 τ, dissolved Fe(II) concentration decreased to 6 μM while effluent [DO] was 0.95 mg/L, indicating a diminished FeS content in the suspension. The dissolved U concentration first dipped to 1.1 μM and then quickly increased to a peak value of 6.5 μM, following a similar trend of previous experiments (Figure 6.4). In comparison, the dissolved U concentration quickly increased after the addition of UO_2 at 52 residence times, while the Fe(II) concentration further dropped to 3 μM and the DO rose to 1.0 mg/L. Although the detectable Fe(II) showed traces of FeS solid in the suspension, its low quantity was unable to effectively scavenge DO, allowing for a rapid increase of DO in the CSTR. However, when UO_2 was added after the complete FeS oxidation beyond 70 residence times, a completely different profile of UO_2 dissolution resulted. Dissolved U slowly increased to a steady-state concentration of 2.7 μM, similar to the systems containing Fe(III) hydroxides and UO_2 solids (see section 6.3.2). In general, the results of this study show that before DO breakthrough, UO_2 dissolution rate decreased with decreasing contact time with FeS (UO_2 addition at a later time), and suggest that a low concentration of FeS contributes to the enhanced dissolution rate of UO_2 when DO breakthrough occurs.

6.3.2 UO_2 Oxidation by Fe(III) Hydroxides

The FeS oxidation products during oxidation experiments (as shown in Chapter 4), include mainly goethite, lepidocrocite, and elemental sulfur. The solid mixture was utilized to assess whether they could enhance the oxidation of UO_2 under either oxic or anoxic conditions. At an influent DO of 1.8 mg/L in the presence of the FeS oxidation products,

dissolved U was immediately detected in the effluent solution and reached a steady-state dissolution rate after ~35 residence times. The rates calculated from $[U]_{ss}$ were comparable to those in control experiments in the absence Fe(III) hydroxides (Figure 6.5). Similarly, experiments conducted with synthetic two-line ferrihydrite at pH 7 showed a UO_2 dissolution rate of 1.9 $\times 10^{-8}$ mol g^{-1} s^{-1}, almost the same as the control. These results suggest limited impact of Fe(III) hydroxides on UO_2 oxidative dissolution under oxic conditions. Under oxygen-free conditions, UO_2 dissolved at a significantly lower rate of 1.42 $\times 10^{-9}$ mol g^{-1} s^{-1} in the presence of Fe(III) hydroxides. This rate was slightly lower than in the control (2.01 $\times 10^{-9}$ mol g^{-1} s^{-1}) in the absence of Fe(III) hydroxides.

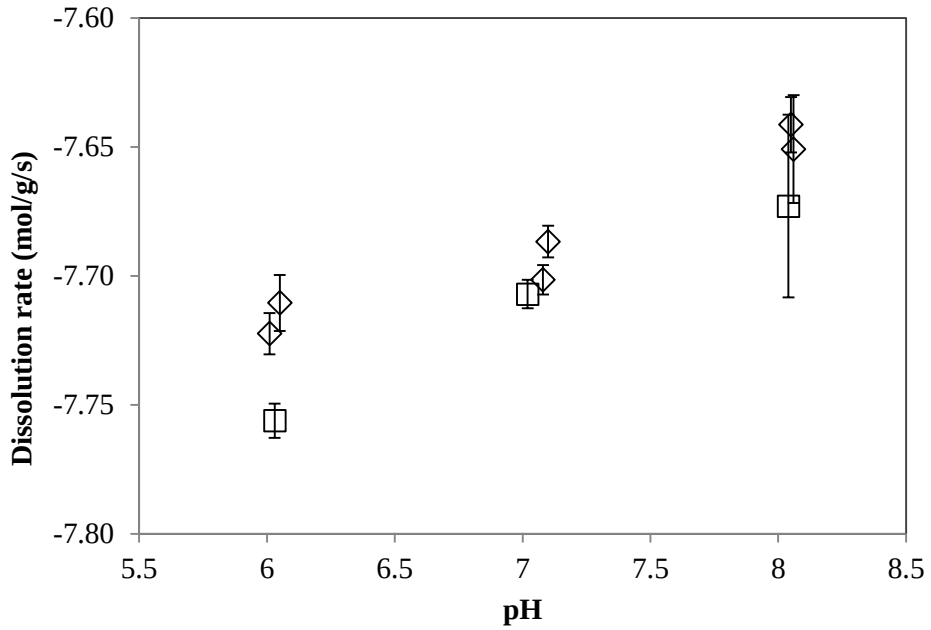

Figure 6.5 UO_2 dissolution rates (mol g^{-1} s^{-1}) estimated from steady-state dissolved U concentration in the presence (□) and absence (◊) of Fe(III) hydroxides as a function of solution pH.

6.3.3 UO_2 Interactions with Fe(II) Species

Fe(II) species, adsorbed on FeS oxidation products or dissolved in solution, may reduce the surface U(VI) species that form as a passivation layer on the UO_2 surface when oxygen is present. To test for this possibility, an Fe(II)-containing solution (~0.09 mM) was fed to the CSTR containing a suspension of Fe(III) hydroxide and UO_2 solids at pH 6 and DO of 1.8 mg/L (Table 6.2). However, UO_2 dissolution followed a similar pattern as in the control containing UO_2 alone, and reached a steady U(VI) concentration after ~25 residence times. Because dissolved Fe(II) equilibrated with surface-adsorbed Fe(II) at steady-state, the results indicated that the passivation layer on UO_2 was not reactive with surface-adsorbed Fe(II) on Fe(III) hydroxides under oxic conditions (Table 6.2). In the absence of Fe(III) hydroxides, dissolved Fe(II) also showed no influence on UO_2 dissolution at pH 6, suggesting that soluble Fe(II) does not likely react and disrupt a passivation layer of U(VI) on UO_2 under oxic conditions.

Under anoxic conditions, surface-adsorbed Fe(II) by Fe(III) hydroxides appeared to further limit UO_2 dissolution at pH 7. After 20 residence times, UO_2 dissolution resulted in a dissolved U concentration of only ~0.04 μM at steady-state. The dissolution rate was 2.2×10^{-10} mol g^{-1} s^{-1}, almost two orders of magnitude lower than in the absence of dissolved Fe(II) (Table 6.2). Dissolved Fe(II) may have scavenged trace oxygen under "anoxic" conditions, leading to less passivation and the lower U(VI) dissolution rate. Because Fe(II) quickly diminished at pH > 7 due to the reaction with dissolved oxygen, surface-adsorbed Fe(II) was not suspected to be important under oxic conditions at higher pH.

Table 6.2 Experimental UO_2 dissolution rates normalized to mass (R_m) obtained in the presence and absence of dissolved Fe(II) under artificial groundwater conditions.

$[UO_2]$ (mM)	[Fe(III)] (mM)	pH	Influent DO (mg L^{-1})	Influent Fe(II) (mM)	Flow rate (mL min^{-1})	$R_m \times 10^{-8}$ mol g^{-1} s^{-1}
0.48	16.1	6.1	1.8	0.09	1.78	1.58
0.48	16.1	6.1	1.8	0.03	1.75	1.62
0.48	0	6.1	1.8	0.09	1.80	1.79
0.48	16.1	7.1	< 0.2	0.09	1.96	0.022
0.48	16.1	7.1	< 0.2	0	1.82	0.14

6.3.4 XAS Spectroscopic Analyses of Oxidized UO_2

X-ray absorption spectroscopy was used to provide evidence for the possible formation of a passivation layer on the surface of UO_2 that would control the dissolution rate before and after DO breakthrough. Solid samples were collected from pH 6, 7, and 8 experiments in the presence of 1.8 mg L^{-1} influent DO and 18.7 mM FeS after DO breakthrough (~200 residence times). The samples were analyzed for U L_{III}-edge XANES and EXAFS to detect changes in U speciation that would indicate an increasing presence of U(VI) associated with the passivation of UO_2 particles as oxidation proceeded.

The XANES results of U solids showed that the absorption edge positions for all samples shifted from U(IV) standard to higher energy, indicating oxidized UO_2 particles after exposure to dissolved oxygen (Figure 6.6). While samples from the pH 6 and 7 experiments were slightly oxidized to almost an identical degree, greater oxidation occurred at pH = 8 as the edge position shifted substantially to those in the U(VI) reference spectra. A linear combination fitting (LCF) of the XANES revealed that ~60% of U in the bulk solid remained as U(IV) at pH 6 and 7 (Table 6.3). In contrast, the U(IV) component in the solid-bound U decreased to ~36% at pH 8 after reacting with oxygen. However, it should be noted that the LCF assumes the higher-valent U(VI) is present as UO_2^{2+} species, which may not correctly

represent the actual U(VI) component in oxidized UO_2 solids. The R-factor, a measure of mean square sum of the misfit at each data point, was ~0.005 for the pH 8 sample, significantly higher than that for the unoxidized UO_2 sample (~0.0008). Fast surface oxidation may produce UO_{2+x} phases, where the predominant U site's local structure would be more similar to that in $UO_{2.00}$ (Ulrich et al., 2009). Because no UO_{2+x} (e.g., U_4O_9) XAS reference spectra were not collected, such as phase could not be verified in the pH 8 sample by XAS analysis.

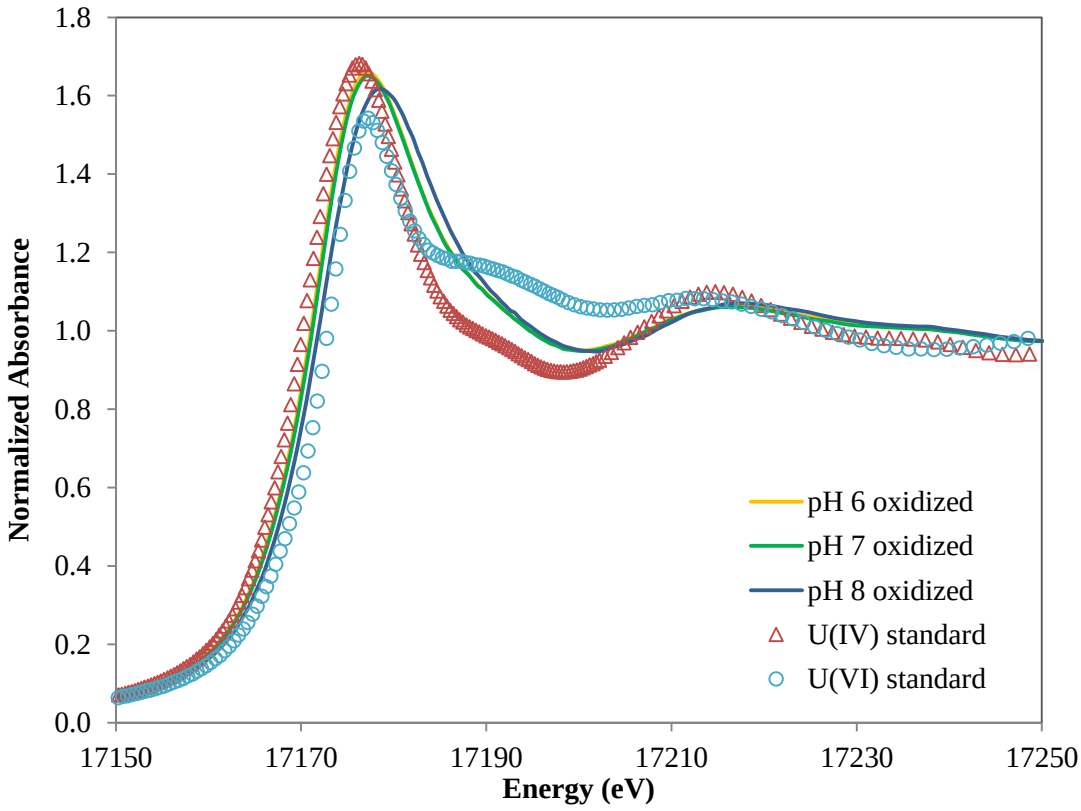

Figure 6.6 Normalized uranium L_{III}-edge XANES spectra of CSTR samples as a function of oxidation residence time in the presence of FeS compared to U(VI) and U(IV) standards (dotted lines).

Table 6.3 Uranium speciation in selected CSTR samples as calculated from XANES LCF results. The relative concentration of U components, i.e., U(IV) and U(VI) are presented as percentages. Relative errors of fitting are given in the parentheses.

Element	Species component	Synthetic uraninite	pH 6	pH 7	pH 8
Uranium	*U(IV) (%) uraninite*	72 (2)	63 (3)	60 (2)	36 (5)
	U(VI) (%) Uranyl	28 (2)	37 (3)	40 (2)	64 (5)
	R-factor	*0.0008*	*0.003*	*0.003*	*0.005*

EXAFS and the associated Fourier transforms (FT) of the oxidized uraninite at pH 6, 7, and 8 were compared to spectra for unoxidized UO_2 during inhibition period and for crystalline $UO_{2.00}$ (Figure 6.7). A qualitative comparison of the spectra shows that the amplitude of EXAFS spectra for all samples were significantly reduced from the crystalline $UO_{2.00}$, suggesting a reduced number of backscatters relative to the central atom, especially at high wave numbers. However, the difference of EXAFS spectra between samples is not obvious, implying that the overall UO_2 structure was qualitatively preserved during oxidation. Similar conclusions are obtained from the FT results where the ratio of the amplitude of the FT peak of the first U-U shell to the first U-O shell is greatly reduced for oxidized samples compared to crystalline $UO_{2.00}$. The decreased U-O shell amplitude confirmed the nanoparticulate size of the synthetic UO_2 used in this study. After DO breakthrough, the U-O shell remained after considerable dissolution, although the amplitude decreased compared to the unoxidized uraninite as a result of smaller particle size. The most notable changes in the FT occurred at the local and intermediate distances (e.g., 1 – 2.2 Å) of the U-O shell peak. For the pH 8 sample, the U-O FT peak appears to split into two subshells at ~1.8 and 2.1 Å, similar to the synthetic U_4O_9 previously reported by Schofield et al. (2008). The visually asymmetric U-O peak is believed to be characteristic of UO_{2+x} solids,

which usually consist of multiple U-O subshells (Conradson et al., 2004). In contrast, oxidized uraninite at pH 6 and 7 exhibited only subtle changes in the shape of U-O shell except for the reduced amplitude.

Combined, the XANES and EXAFS results indicate the oxidation of UO_2 leads to a UO_{2+x}–like phase at pH 8 with a local structural distortion in the U-O shell. Oxidized U(VI) was suspected to penetrate far enough into the particle to cause an apparent alteration in the overall oxidation state. In contrast, the oxidation of uraninite by dissolved oxygen at pH 6 and 7 experiments generated solid phases more similar to the initial synthetic UO_2 than to UO_{2+x}.

The EXAFS fitting of the structure of oxidized UO_2 included two U-O single scattering (SS) paths, one U-U SS path, and the multiple scattering (MS) paths from two neighboring oxygen atoms. The fitting results confirm that the solid U phase at pH 6 and 7 after oxidation was consistent with a nano-particulate uraninite (Table 6.4). The FTs of both samples showed a peak at ~1.9 Å, corresponding to a U-O1 interatomic distance (R) of ~2.37 Å. At pH 6, the first shell U-O1 coordination number (CN) of 6.4 (less than the 8 O of a crystalline $UO_{2.00}$) was similar to the unoxidized UO_2 during the inhibition period (CN: 5.9) (Chapter 5). However, the higher σ^2 for the peak fitting indicates an increased disorder in the UO_2 structure when incorporating excess oxygen atoms during oxidation. The CN of the second peak at ~3.6 Å (corresponding to a U-U distance of 3.87 Å) remained at ~5 atoms after oxidation. In comparison, the coordination numbers of both U-O1 and U-U shells in pH 7 samples are significantly reduced from an unoxidized UO_2 (Table 6.4). This result supports the expectation of smaller uraninite particles as a result of substantial oxidative dissolution at the point of sampling. For the pH 8 data, fits using the same model as for previous samples

resulted in errors of delta E_0. Similarly, adding a split oxygen shell for testing the presence of hyperstoichiometric U sites were attempted, but were not stable and collapsed into a single shell. Furthermore, adding the CN of U-O shell of uranyl cations at distances of < 1.9 Å did not improve the fits.

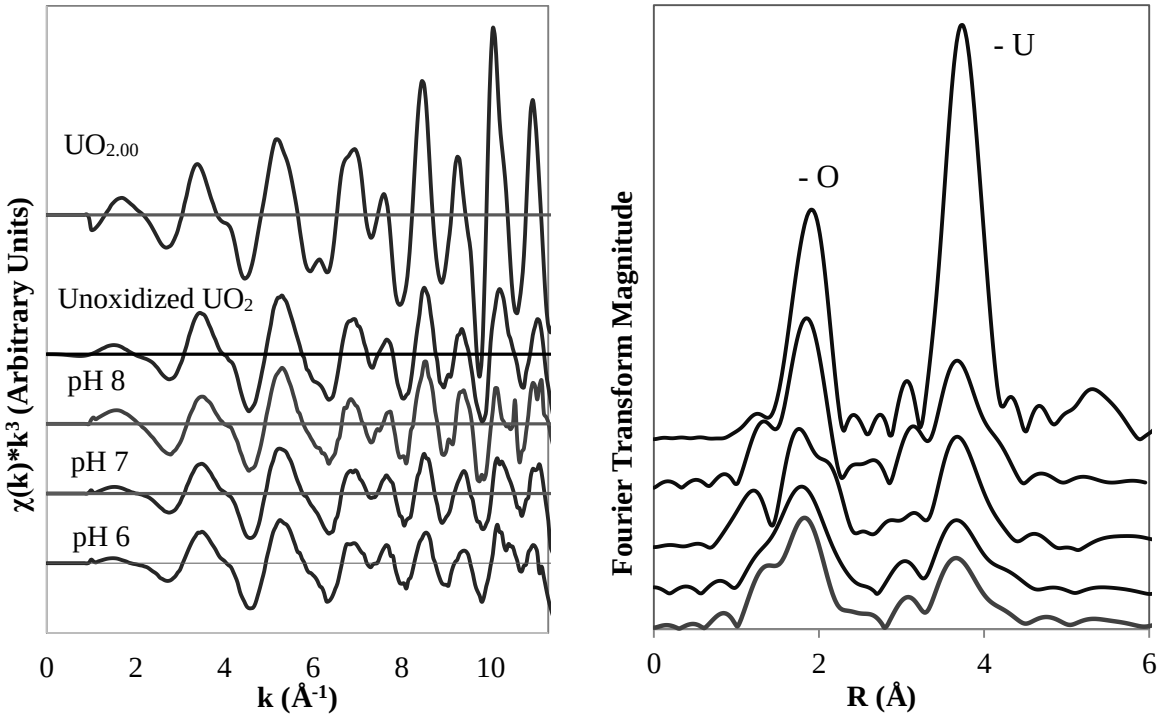

Figure 6.7 U L_{III}-edge spectra for samples collected at ~200 residence times from pH 6.1, 7.1, and 8.1 flow-through experiments. The results are compared with crystalline $UO_{2.00}$. and unoxidized UO_2 during inhibited period. (a) EXAFS spectra (k range for modeling = 2.0–11 $Å^{-1}$) and (b) corresponding Fourier transforms.

Table 6.4 Structural parameters extracted from U L_{III}-edge EXAFS data of samples collected from the CSTR. Paths denoted with O1, U1, and O2 stand for first oxygen shell, the first uranium shell, and a second oxygen shell, respectively. The path O=U=O is a multiple scattering path. Estimated errors are given in parentheses.

Sample / Path		**U-O1**	**U-U1**	**U-O2**	**O=U=O**
UO_2 standard	*CN*	8.0	12.0	24.0	8.0
	R (Å)*	2.37 (0.02)	3.87 (0.01)	4.53 (0.04)	4.74 (0.03)
	σ^2 (10^{-3} Å^2)	5 (1)	2 (1)	8 (2)	9 (2)
pH 6	*CN*	6.44 (0.5)	5.1 (1.9)	10.2 (4.3)	6.44
	R (Å)*	2.37 (0.01)	3.87 (0.01)	4.53 (0.1)	4.74 (0.02)
	σ^2 (10^{-3} Å^2)	12 (1)	6 (3)	20 (21)	25 (2)
pH 7	*CN*	4.84 (0.6)	2.71 (2.2)	5.42 (4.4)	4.84
	R (Å)*	2.37 (0.01)	3.87 (0.01)	4.53 (0.09)	4.74 (0.02)
	σ^2 (10^{-3} Å^2)	9 (2)	2 (3)	10 (20)	17 (4)

CN: coordination number; *R*: interatomic distance; σ^2: mean-square disorder.
*R values are the actual bonding distances, which are phase-shifted from the FT peak positions.

6.3.5 XPS Spectroscopic Analyses of Oxidized UO_2

While XANES analyses showed the average change of oxidation state of solid-bound U in the bulk sample, XPS allows a quantitative determination of U(IV) and U(VI) species present on the surface of oxidized uraninite. The XPS results of the original unreacted synthetic UO_2 material indicated a small but measurable U(VI) component (~20%) on the surface (Chapter 3). Some portion of the oxidized U might be due to sorbed U(VI) that occurred during synthesis. This result is consistent with XANES analysis, which also showed detectable U(VI) in the synthetic uraninite solid (detection limit for U(VI) by XPS is ~5%).

For the study of the potential change in the passivation layer during the exposure of UO_2 to oxygen, solid samples were collected from pH 6, 7, and 8 suspensions in the presence

of 4.8 mM FeS before and after DO breakthrough and analyzed for the surface U oxidation state (Figure 6.8). During the inhibition period of UO_2 dissolution in the presence of FeS at pH 7, the surface of UO_2 exhibited about 95% of U(IV) and 5% U(VI) (Table 6.5). The solid-bound U was reduced at 41τ during inhibited UO_2 dissolution, consistent with the EXAFS results for pH 7 discussed in Chapter 5. Even after DO breakthrough at 56τ, surface U remained predominantly reduced as indicated by the XPS spectrum, with ~94% of the total U as U(IV). These results indicated that the oxidized U(VI) species that form on the uraninite surface are effectively removed at pH 7 even after DO breakthrough.

At pH 6, the XPS-detectable U(VI) fraction increased substantially to 29% at 31 τ while DO levels were still low in the CSTR (~0.8 mg/L). After DO breakthrough occurred, the U(VI) component rapidly increased further to 83% within ~35 residence times. This result was in contrast to the pH 7 experiments where the UO_2 surface remained largely free of a passivation layer throughout the period of inhibited UO_2 dissolution. Apparently at pH 6, the solution phase was less effective at removing U(VI) from the surface than at pH 7, and the residual FeS was incapable of preventing UO_2 from surface oxidation. The proportion of surface U(VI) continued to increase until complete transformation to U(VI) at 82 τ (Figure C.1 of Appendix C). However, this trend of U oxidation was not observed by XANES results, which only showed a partially oxidized U solid after considerable UO_2 dissolution (Figure 6.6). The corresponding EXAFS also did not support the presence of the short axial U=O bond (i.e., ~1.8 Å) typical of uranyl species. This disparity can be attributed to the enhanced surface sensitivity of XPS to the near-surface layers rather than the averaged coordination of the bulk solid by XAS.

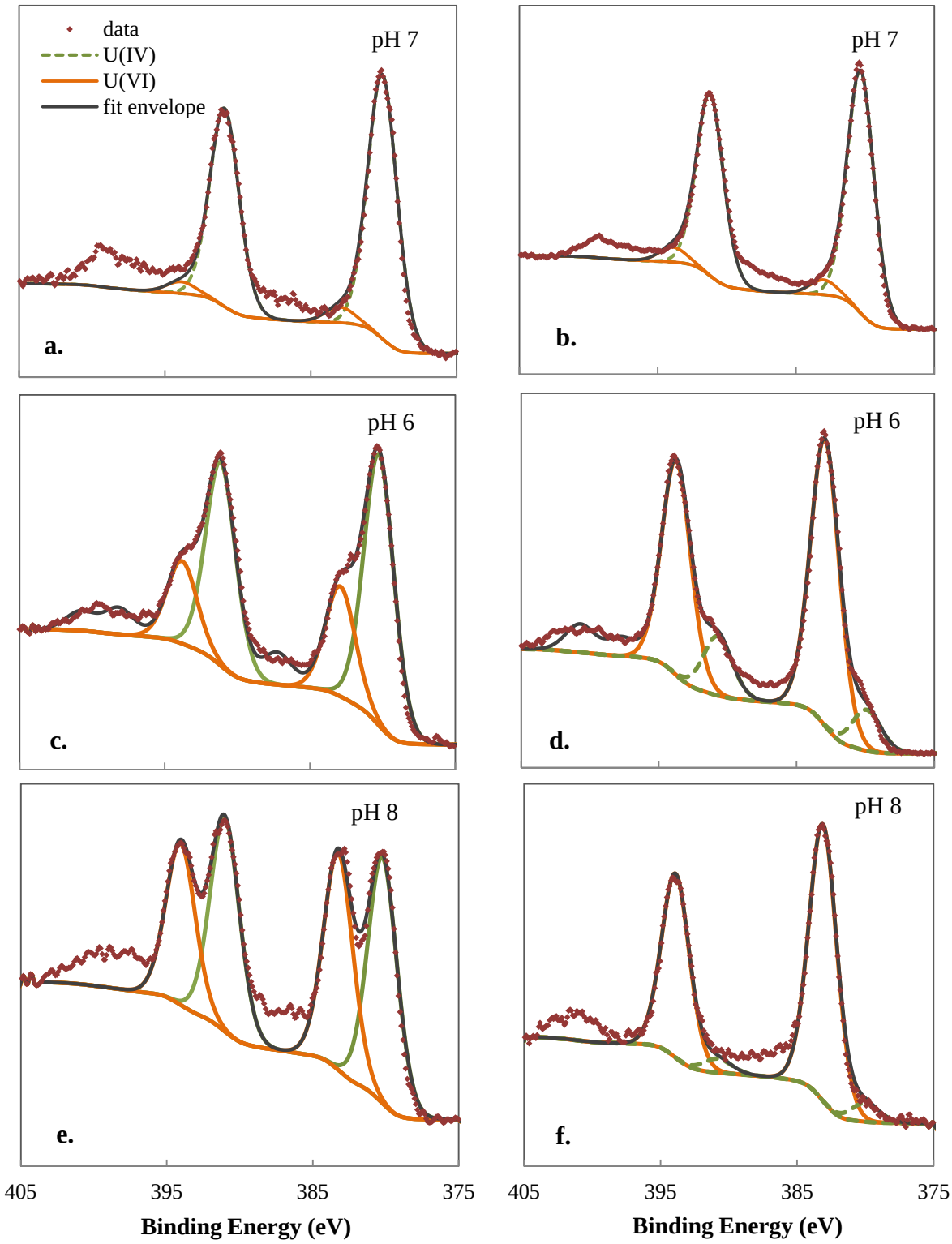

Figure 6.8 Deconvolution of representative U 4f XPS spectra of CSTR samples collected from pH = 6, 7, and 8 experiments in the presence of 4.8 mM FeS solids. (a) 41 τ at pH 7; (b) 56 τ at pH = 7;(c) 31 τ at pH 6; (d) 56 τ at pH 6; (e) 49 τ at pH 8; (f) 60 τ at pH 8. All experiments were carried out under DO of 1.8 mg/L artificial groundwater conditions.

Table 6.5 Mole percentage of U(IV) and U(VI) as determined by XPS on CSTR samples collected from flow-through experiments under varied pH conditions.

Sample	Treatment condition	U(IV) (%)	U(VI) (%)
41 τ, pH = 7	Before DO breakthrough	95	5
56 τ, pH = 7	After DO breakthrough, during enhanced UO_2 dissolution	94	6
31 τ, pH = 6	Before DO breakthrough	71	29
56 τ, pH = 6	After DO breakthrough, almost complete FeS oxidation	17	83
49 τ, pH = 8	Before DO breakthrough	53	47
59 τ, pH = 8	After DO breakthrough, almost complete FeS oxidation	6	94

While FeS provided the longest period of inhibited UO_2 dissolution at pH 8 (~54 τ), XPS analysis of sample at 49 τ indicated the production of a surface with a high U(VI) (47%) component even before DO breakthrough. Shortly after DO breakthrough, this proportion quickly increased to 94%, with an almost complete oxidation of UO_2 surface. This result demonstrated that the continuous flushing and the presence of carbonate and calcium in solution were not able to remove U(VI) species generated on the surfaces at pH 8. Although FeS was able to scavenge most of the DO in the suspension, some oxygen still reacted with UO_2 to oxidize the surface. The detachment of U(VI) from UO_2 surface was slower than at pH 6 and 7, evidenced by the development of a thick U(VI) passivation layer during oxidation. The highly oxidized UO_2 surface at pH = 8 is compatible with that obtained by XANES and EXAFS results. During oxidative dissolution in the CSTR at pH = 8, oxidized uraninite particles may eventually consist of a UO_3-like outer layer and a UO_{2+x} particle core.

6.3.6 Thermodynamic Calculation of Uranium Speciation

Visual MINTEQ was used to predict equilibrium U speciation at varied pH before DO breakthrough in the flow-through systems. Figure 6.9 shows that the neutral $Ca_2UO_2(CO_3)_3(aq)$ complex was the dominant species from pH range of 6.0 to 8.2, while minor species of $UO_2CO_3(aq)$ and $CaUO_2(CO_3)_3^{2-}$ existed at pH 6 and 8, respectively. Among the three pH values studied, the total dissolved carbonate concentration was the highest at pH 7 (~12 mM) as a result of 5% CO_2 gas equilibrating with the carbonate solution. In comparison, the total carbonate concentration decreased to 2.7 mM at pH 6, with the dominant species as $H_2CO_3^*$. In the experimental design, the total carbonate was fixed (rather than equilibrated with CO_2 gas) and lowered to 1 mM to prevent calcite precipitation at pH 8, where HCO_3^- was the dominant species. The thermodynamic modeling indicated the solution was still slightly oversaturated with respect to calcite at pH 8, which could further lower the total carbonate concentration in solution. However, total carbonate and calcium concentrations at all three pH values were in great excess of the dissolved U(VI) concentration before and after DO breakthrough occurred.

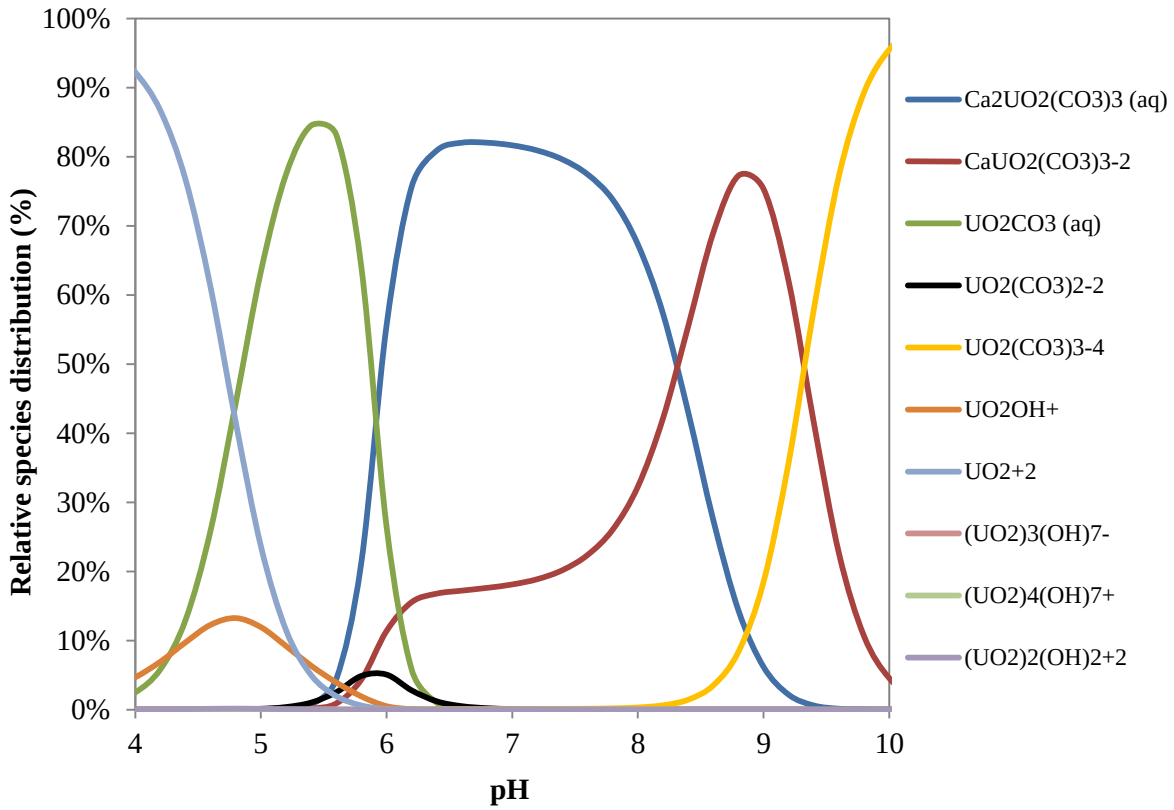

Figure 6.9 Dissolved U(VI) species distribution as a function of pH calculated by Visual MINTEQ. Simulation conditions: 1 μM UO_2^{2+}, 8.0 mM $NaHCO_3$, 0.4 mM KCl, and 2.0 mM $CaCl_2$. The solution is equilibrated with 2% P_{O2}, 5% P_{CO2} gas mixture.

6.4 Discussion

6.4.1 Accelerated Dissolution Rate of UO_2 at Neutral pH

After DO breakthrough occurred, the rapid dissolution of UO_2 was consistently observed in flow-through experiments at pH 7 in the presence of FeS at varied concentrations (Figure 6.1). However, the enhanced oxidative dissolution rate of UO_2 relative to that in the control experiments (UO_2 alone) did not occur in the pH 6 and 8 experiments. Most notably, UO_2 dissolved at slower rate than in the control at pH 8 when FeS-controlled DO no longer persisted. While the impact of solution pH on FeS oxidation has been documented (Jeong et al., 2010a; Bi and Hayes, 2013), this disparate behavior of UO_2 dissolution within this small pH range was not reported previously. In order to determine the environmental significance

of FeS-controlled UO_2 dissolution, it is necessary to identify the rate-limiting mechanisms of UO_2 oxidative dissolution.

Three possible mechanisms for promoting UO_2 dissolution rate at pH 7 in the presence of FeS after DO breakthrough may be hypothesized. The first mechanism depends on UO_2 oxidation by Fe(III) hydroxides, the oxidation products of FeS by oxygen, while the second is attributed to the labile or adsorbed U species, which are generated during the period of inhibited UO_2 dissolution and low DO. The labile or adsorbed U species were subsequently released into the effluent solution in response to increased DO concentrations after breakthrough. The third mechanism involves the disruption of passivation layer by FeS during oxidative dissolution. The absence of passivation layer at pH 7 may result in the fast oxidative dissolution of UO_2 and the release of Ca-U(VI)-CO_3 complexes.

Although the first mechanism has been previously studied and suggested as a potential pathway for UO_2 oxidation under sulfate-reducing conditions (Ginder-Vogel et al., 2006), the calculated oxidation rate by ferrihydrite was three orders of magnitude lower than that by dissolved oxygen (Ginder-Vogel et al., 2010). The flow-through experiments conducted in this study using mixed Fe(III) hydroxides and ferrihydrite confirmed the negligible impact of Fe(III) solids on the UO_2 oxidative dissolution rate under oxic conditions (Figure 6.5). In the presence of Fe(III) hydroxides, UO_2 dissolved at a slightly lower rate than in the absence of Fe(III). In addition, because Fe(III) hydroxides were continuously generated as oxidation products of FeS by dissolved oxygen, their impact on UO_2 dissolution was expected to be progressive rather than abruptly occurring only after DO breakthrough.

The second mechanism was examined by the extraction of adsorbed U(VI), which only showed less than 1% extractable U after a 21 hr reaction period with a 0.5 M $NaHCO_3$ solution. If labile U dissolved after DO breakthrough accounted for the previously adsorbed U(VI), 25% - 36% of total U should have been adsorbed by FeS and its oxidation products during the inhibition period, depending on FeS and DO concentrations. In Chapter 5, XANES and EXAFS analyses indicated the lack of UO_2 solid oxidation during the inhibited dissolution, which showed predominantly nano-particulate uraninite throughout the inhibited dissolution. Combining U extraction and solid characterization results, the enhanced UO_2 dissolution at pH 7 was unlikely due to the desorption of soluble U(VI) after DO breakthrough in flow-through experiments.

The rejection of the first two mechanisms leaves the disrupted UO_2 passivation layer as a probable candidate for causing fast UO_2 dissolution. The XPS results of this study showed a clean, predominantly U(IV) surface during and shortly after the inhibited UO_2 dissolution at pH 7 in the presence of FeS (Figure 6.8a, b). In contrast, prior studies have reported the formation of a near-surface UO_{2+x} coating around UO_2 core during oxidation, which possibly controls UO_2 oxidative dissolution rate by dissolved oxygen (Casas et al., 1998; Ulrich et al., 2009). Although the synthetic UO_2 used in this study initially contained ~20% U(VI) on the near-surface, the U(VI) surface coating was removed under CSTR flow conditions (Figure 6.8a), probably due to UO_2 dissolution and reduction of U(VI) by FeS particles. During the inhibition period, the UO_2 dissolution rate was believed to be controlled by surface oxidation, whereas the detachment of U(VI) complexes was relatively fast (Bi and Hayes, 2013). The absence of visible U(VI) accumulation as determined by XAS and XPS also support the mechanism that the rapid detachment of $Ca_2UO_2(CO_3)_3(aq)$ at pH 7 prevents

the formation of U(VI) passivation layer. This mechanism may also apply to the fast UO_2 dissolution in batch reactor experiments presented in Chapter 3 and in Bi et al. (2013).

Because UO_2 surface was prevented from U(VI) accumulation and passivation, the step of U(VI) complex detachment has to be fast enough to allow the U(VI) products to diffuse into bulk solution. When DO concentration remains low due to FeS scavenging, this surface-detachment limited oxidation can be reasonably achieved (Bruno et al., 1991). However, the results from the current study indicate that the fast U(VI) detachment can also be accomplished at a stage of DO increase, which seems to contradict the previous studies that a U(VI) passivation layer forms under mildly oxidizing conditions (~0.5 mg/L) (Ulrich et al., 2009). This disparity can be attributed to the coexistence of FeS with UO_2 that controls the DO concentration in the CSTR and the presence of dissolved calcium and carbonate in the influent solution. Although the decreased concentration of FeS caused DO breakthrough, the residual FeS (estimated 0.3 – 0.5 mM) allowed the DO levels to slowly increase until the FeS was completely depleted. Meanwhile, the formation of stable Ca-U(VI)-CO_3 complexes facilitated the desorption of U(VI) species from UO_2 surfaces (Stewart et al., 2010). In contrast, DO levels were quickly established at ~1.8 mg/L in the control experiments without FeS. The detachment of Ca-U(VI)-CO_3 complexes could no longer offset the fast surface oxidation of UO_2, resulting in the accumulation of U(VI) and a slower dissolution rate.

With a "clean" UO_2 surface, dissolved oxygen may quickly attach to the UO_2 surface and transfer electrons to U(IV). Due to the rapid detachment of surface complexes, the rate of UO_2 dissolution would be controlled by surface oxidation and therefore the DO concentration. With an increasing supply of DO after breakthrough assisted by a rapid surface detachment, the apparent dissolution rate would consequently be enhanced unless the

UO_2 surface became passivated. It should be noted that the observed fast UO_2 dissolution was only transient. The dissolved U concentration typically peaked within 32 τ after DO breakthrough with an influent DO of 1.8 mg/L (Figure 6.1), whereas it peaked within 20 residence times with an influent DO of 7.8 mg/L. Although the gradient of DO concentration was greater, the UO_2 dissolution rate was estimated to be comparable to that at an influent DO = 1.8 mg/L.

The transient phase of fast UO_2 dissolution and a clean UO_2 surface suggests the intricate interplay between surface oxidation versus U(VI) detachment in limiting the overall dissolution rate during the suboxic to oxic transition. As long as DO concentration remains low to ensure a slower surface oxidation than U(VI) detachment, the overall dissolution rate can be enhanced by the increasing DO concentration. When DO concentration becomes high enough to passivate UO_2 surface, the U(VI) layer may eventually limit the UO_2 dissolution rate because oxygen has to diffuse through the layer before reacting with UO_2. Therefore, this shift of the rate-limiting mechanism is essentially governed by the available DO, which can be controlled by FeS as an oxygen scavenger, influent DO concentration, flow rate, and calcium and carbonate concentration.

6.4.2 Unchanged Dissolution Rate of UO_2 at Acidic pH

The fast dissolution of UO_2 after DO breakthrough was not observed at pH 6 experiments using an influent solution with 1.8 mg/L DO (Figure 6.2). Instead, steady-state dissolution of UO_2 was established soon after DO breakthrough, resulting in comparable level of dissolved U concentrations as in the control experiments. As indicated by XPS results, surface passivation took place while DO levels were still low, showing ~30% U(VI)

present at the near surface at 31 τ (Table 6.5). At this time point, dissolved Fe(II) concentrations remained higher at 0.04 mM, a sign of incomplete oxidation of FeS. The passivated surface suggests that either the detachment of surface U(VI) complexes was too low to effectively remove the U(VI) products at pH 6 or FeS was incapable of reducing the UO_2 surface.

The impact of solution pH on FeS oxidation was previously discussed in Chapter 5. The results described in details there indicated that a slightly acidic pH can result in substantial FeS dissolution at low DO concentrations. The release of dissolved Fe(II) species lowers the reducing capacity of FeS for scavenging oxygen and, consequently, reduces the period of inhibited UO_2 dissolution. Although DO was present at a low concentration even during the inhibition period, reaction with UO_2 still took place. The less favorable detachment of U(VI) surface complexes at pH 6 compared to that at pH 7 (as noted earlier) may be attributed to the lower total carbonate concentration at pH 6 (2.7 mM vs. 12 mM). While the free Ca^{2+} ion concentration remained at 2 mM, the dominant carbonate species changed to $H_2CO_3^*$ at pH 6, possibly reducing the tendency to form $Ca_2UO_2(CO_3)_3(aq)$ complex (Wazne et al., 2003).

In addition, soluble Fe(II) was found to be a weak reductant for oxygen and U(VI) at pH 6 in the present study, although some researchers reported U(VI) reduction by aqueous Fe(II) under reducing conditions (Liger et al., 1999; Du et al., 2011). In the current study, adsorbed Fe(II) by Fe(III) hydroxides at pH 6 was investigated as a potential reductant for the U(VI) passivation layer, but the surface Fe(II) failed to promote UO_2 dissolution under oxic groundwater conditions. As such, the loss of Fe(II) as soluble species at pH 6 may reduce the ability of FeS to diminish the formation of a U passivation layer when oxygen

intrusion occurs. Overall, the less favorable detachment of U(VI) surface complexes, the lower reducing capacity of FeS at pH 6, and the subsequent formation of a U(VI) passivation layer may explain the lack of a significant enhancement of the UO_2 dissolution rate at pH 6 when DO breakthrough occurs.

6.4.3 Decreased Dissolution Rate of UO_2 at Basic pH

Contrary to the enhanced rate of UO_2 dissolution at pH 7, UO_2 dissolved at a noticeably slower rate at pH 8 when FeS approached depletion at DO breakthrough in the flow-through experiments. The XAS and XPS results suggested the formation of UO_{2+x} phase as the final product of UO_2 oxidation by dissolved oxygen in the pH 8 solution. The detectable surface oxidation of UO_2 started during the inhibition period, generating a U_4O_9-like surface before the apparent DO breakthrough. As oxidation proceeded, the complete oxidation of surface further generated a UO_3-like outermost layer as evidenced by XPS analysis, similar to the results in Ulrich et al. (2009). The completely oxidized U(VI) surface layer was not apparent at pH 6 or 7, and was likely the cause of the slower dissolution rate of UO_2 at pH 8.

The more easily oxidized UO_2 surface at pH 8 may be explained by 1) the slower detachment of U(VI) complexes than at pH 7, and 2) the obstructed ability of FeS to scavenge oxygen at pH 8. Thermodynamic modeling of the solution system indicated that the total carbonate concentration was the lowest at pH 8 (1 mM), one order of magnitude lower than at pH 7. In addition, calcite and liebigite ($Ca_2UO_2(CO_3)_3$(s)) solid phases may precipitate due to oversaturation. Although the formation of a uranyl mineral was not confirmed by EXAFS analysis, calcite was identified in the XRD pattern and TEM images of the final oxidation products (Appendix D). The precipitation of calcite likely further lowered

HCO_3^- concentration, limiting the formation of $Ca\text{-}UO_2\text{-}CO_3$ complexes. It should be mentioned that the mineral calcite was not clearly found in the pH 8 control experiments in the absence of FeS. As a possible explanation to this discrepancy, the oxidation products of FeS, i.e., Fe(III) hydroxides and elemental sulfur, possess large surface areas for the adsorption of Ca^{2+} and HCO_3^- ions and thus provide crystallization sites for calcite formation. The promotion of calcite precipitation may further lower dissolved Ca^{2+} and HCO_3^- concentrations by adsorption, therefore limiting the detachment of U(VI) species from UO_2 surfaces.

At basic pH values, FeS was shown to undergo a predominantly direct solid-phase transformation to produce Fe(III) hydroxides and elemental sulfur phases (Chapter 5). FeS dissolution was negligible throughout the course of oxidation, releasing less than 1% of total Fe as soluble Fe(II) into the effluent. Jeong et al. (2010a) demonstrated that the development of a Fe(III) hydroxides coating on FeS surfaces during oxidation at basic pH. The surface Fe speciation likely changed via the sequence of $\equiv Fe^{II}\text{-}S \rightarrow \equiv Fe^{III}\text{-}S \rightarrow \equiv Fe^{III}\text{-}O$, which increasingly hindered the contact of oxygen with FeS. The considerable oxidation of Fe(II) was also observed in XPS data collected from pH = 8 experiments, which showed a greater shift of binding energy toward higher values than at pH = 6 and 7 samples (Figure C.1 of Appendix C). The Fe(III) surface coating possibly limited oxygen scavenging by FeS, allowing for more oxygen reacting with UO_2 surfaces.

6.5 Conclusions

This study investigates UO_2 dissolution behavior in the presence of FeS and explains the rate-limiting mechanism when FeS becomes depleted during suboxic-oxic transitions.

The previous chapters demonstrated that FeS inhibited UO_2 dissolution through oxygen scavenging and keeping DO low, when FeS is present in molar excess compared to U under varied geochemical conditions. The results of this chapter illustrate the formation of passivation layers on UO_2 surfaces and stable Ca-UO_2-CO_3 complexes in affecting the overall UO_2 oxidative dissolution rate.

While the oxidative dissolution rate of UO_2 is directly limited by the passivation layer on UO_2 surfaces, FeS greatly influenced the passivation processes when coexisting with UO_2 by governing the available DO concentration. In this study, a faster dissolution of UO_2 consistently occurred at pH 7 after DO breakthrough in the flow-through experiments. While DO concentrations were no longer negligible, residual FeS allowed a slow increase of DO to maintain surface-oxidation limited UO_2 dissolution. The dominant Ca-UO_2-CO_3 complexes were thought to be the determining factor in preserving a largely reduced U(IV) surface with a negligible accumulation of U(VI) species. The favorable detachment of U(VI) complexes while leaving the UO_2 core exposed led to the faster transient dissolution at pH 7 compared to pH 6 and 8 until an overwhelming DO concentration passivated its surface after FeS depletion.

In contrast, FeS oxidation at pH 6 resulted in a similar dissolution behavior of UO_2 compared to that in the control in 1.8 mg/L DO groundwater solution. The slightly acidic pH resulted in a substantial dissolution of FeS to soluble Fe(II) species, which proved ineffective in keeping a U(VI) passivation layer from forming, perhaps partly due to less effective DO scavenging. When FeS concentration diminished in the CSTR, the UO_2 surfaces became oxidized and formed a mixed U(IV)/U(VI) outermost layer, similar to those in control

experiments in absence of FeS. The rate of UO_2 dissolution eventually was limited by the detachment of lower-concentration U(VI) complexes.

The rate of UO_2 dissolution at pH 8 during FeS depletion was slightly slower than that observed in the corresponding control. A considerably oxidized UO_2 surface was identified before the event of DO breakthrough as determined by XAS and XPS analyses. The passivation layer then quickly evolved into a completely oxidized U(VI) coating, likely a liebigite phase, contributing to the slow dissolution of UO_2 when effluent DO levels gradually approach the influent concentration of 1.8 mg/L. Because FeS surface was coated by Fe(III) hydroxides resulted from the surface-mediated oxidation, DO scavenging could be less efficient than at lower pH. In addition, uranyl complex formation and surface detachment were likely limited by the lower total carbonate concentration and calcite precipitation in the pH 8 groundwater solution. The promoted oxidation of UO_2 particles ultimately generated a UO_{2+x} bulk phase, which remained relatively stable under the flow-through conditions.

The combined results suggest that the presence of mackinawite in a biostimulation zone can significantly influence the long-term stability of reduced U by controlling DO levels. Oxidant intrusion into anoxic groundwater may eventually consume the reducing capacity of reduced phases, such as FeS, and lead to UO_2 reoxidation. The oxidative dissolution of UO_2 may be temporarily promoted in the presence of low concentrations of FeS, if the U(VI) passivation layer is prevented from forming and DO concentration is nontrivial. The subsequent fast release of dissolved U can be constrained, however, if a faster suboxic-oxic transition allows a rapid passivation of UO_2 surface to generate a less-reactive coating. Because *in situ* geochemical and biological conditions are complex in the

subsurface, a manipulation of passivation layer formation may be impractical. Nevertheless, the correlation between U(VI) passivation layer and rate of UO_2 oxidative dissolution obtained in this study provides a valuable insight for evaluating the stability of reduced U in the subsurface during suboxic-oxic transitions. This study has shown that passivation layers may slow down U mobilization in the subsurface, especially in low carbonate Ca-containing groundwater where uranyl solid phases can precipitate. As long as the reducing capacity of sulfide phases, such as FeS, produced during bioreduction are in excess of the occasional oxidant intrusion concentrations, or are regenerated in subsequent bioreduction periods, the longer-term stability of UO_2 can be realized.

Chapter 7

Conclusions and Recommendations

7.1 Summary of Experimental Work

This dissertation aims at understanding the role of iron sulfide minerals in the long-term stability of reduced uranium under oxic groundwater conditions. By investigating the thermodynamic and kinetic constraints that control UO_2 oxidative dissolution, the present work has identified important mechanisms of FeS-UO_2 interactions at solution-mineral interfaces and demonstrated an inhibited dissolution of UO_2 by FeS in artificial groundwater solutions when prevailing oxygen intrusion occurred. The overarching goal of this research is to mitigate U contamination, protect potable water supplies, and improve health and human welfare in the areas susceptible to U release.

7.1.1 Inhibited UO_2 Oxidative Dissolution by FeS

In pH 7 batch experiments, mackinawite effectively scavenged dissolved oxygen and inhibited UO_2 dissolution until DO breakthrough. The oxidation of structural Fe(II) and S(-II) in FeS were found to control DO levels, leading to the formation of iron hydroxides (i.e., nanogoethite and lepidocrocite) and elemental sulfur, as determined by XRD, XAS, and Mössbauer spectroscopy. Once FeS approached depletion, DO levels rapidly increased and UO_2 oxidative dissolution occurred at a fast rate of $1.2 \pm 0.4 \times 10^{-8}$ mol g^{-1} s^{-1}, higher than

in the control experiment in the absence of FeS ($5.4 \pm 0.3 \times 10^{-9}$ mol g^{-1} s^{-1}). XAS analyses on the final oxidation products identified U(VI)-carbonate surface complexes adsorbed by iron hydroxides, which was the final U(VI) retention mechanism under oxic conditions.

Flow-through reactor studies examined the kinetics of UO_2 oxidative dissolution in the presence of FeS as a function of pH, DO concentration, and FeS content. The dissolution rates in the presence of FeS were found over one order of magnitude lower than those in the absence of FeS under otherwise comparable oxic conditions. Because FeS preferentially reacted with oxygen and possibly soluble U(VI) species, UO_2 particles remained unoxidized during an "inhibition period" at pH 7. The removal of DO by FeS was significant but incomplete during the inhibition period, resulting in surface-oxidation limited dissolution and greater UO_2 dissolution rate with increasing influent DO concentration and decreasing FeS content. Although the rate was independent of solution pH in the range of 6.1–8.1, the length of the inhibition period was shortened by substantial FeS dissolution at the acidic pH. The reducing capacity of FeS for inhibiting UO_2 dissolution was maximized at basic pH where surface-mediated FeS oxidation dominated.

7.1.2 Surface Passivation Limited UO_2 Dissolution

When FeS approached depletion in oxic solution, UO_2 dissolution exhibited strong pH-dependent behavior. At pH 7, fast dissolution of UO_2 consistently occurred after DO breakthrough in the flow-through experiments. Solid-phase characterizations by XAS, XPS, and TEM techniques revealed a clean, unoxidized U(IV) surface and stoichiometric UO_2 bulk core in the presence of FeS even with an increasing DO concentration. The preservation of U(IV) surface was attributed to the fast detachment of surface uranyl complexes and

effective removal of U(VI) facilitated by high carbonate and calcium concentrations. FeS served as an important oxygen scavenger to control the available DO concentration, resulting in a surface-oxidation limited UO_2 dissolution mechanism. The lack of passivation layer contributed to the enhanced overall oxidative dissolution rate of UO_2 for a short period until UO_2 surface became passivated by the overwhelming DO concentration.

Unlike pH 7, oxidative dissolution of UO_2 at pH 6 and 8 established a steady-state effluent U concentration after DO breakthrough, both showing an absence of promoted UO_2 dissolution. The less favorable detachment of U(VI) surface complexes, the lower reducing capacity of FeS, and the subsequent formation of a U(VI) passivation layer may explain the lack of significant enhancement of UO_2 dissolution rate at pH 6 when DO breakthrough occurs. In contrast, the lowest total carbonate concentration and calcite precipitation at pH 8 further limited the formation of ternary Ca-U(VI)-CO_3 complexes and allowed the rapid passivation of UO_2 surfaces. The surface-mediated oxidation of FeS at pH 8 may also hindered the oxygen scavenging by producing a Fe(III) hydroxide coating on FeS particles.

The passivation-layer limited UO_2 dissolution rate observed in this study indicates the dynamic interplay between surface oxidation versus U(VI) detachment in controlling U release during the suboxic to oxic transition. When passivation layers develop on UO_2 surface under oxic conditions, the overall UO_2 dissolution rate may be lowered unless dissolved carbonate and calcium species promote a fast U(VI) detachment by forming highly stable ternary uranyl complexes.

7.1.3 Inactive FeS Oxidation Products for UO_2 Oxidation

Depending on solution pH, abiotic FeS oxidation by dissolved oxygen generated various iron and sulfur species, including dissolved Fe(II), Fe(III) hydroxides solids, and elemental sulfur. While Fe(III) hydroxides were proposed as possible oxidants for reduced U(VI), experiments using either mixed Fe(III) solids or synthetic ferrihydrite demonstrated the negligible impact of Fe(III) solids on oxidative dissolution of UO_2 under oxic conditions. The dissolution rate of UO_2 were almost the same in the presence and absence of Fe(III) solids as measured in flow-through experiments.

While adsorbed Fe(II) by Fe(III) hydroxides were hypothesized as a potent reductant for U(VI), flow-through experiments conducted at pH 6 using Fe(II)-containing solution showed little impact of surface Fe(II) on UO_2 oxidative dissolution. This result supported the observation that UO_2 surface was readily passivated at pH 6, where FeS underwent substantial dissolution during oxidation by oxygen. Higher pH may contribute to greater adsorption of Fe(II) by Fe(III) hydroxides, and also much faster oxidation of soluble Fe(II) and precipitation of Fe(III) solids. Because Fe(II) was readily oxidized at pH> 7 by dissolved oxygen, surface-adsorbed Fe(II) was not suspected to reduce U(VI) under oxic conditions at basic pH.

In the abiotic systems, nano-sized elemental sulfur (S_8^0) was the primary sulfur oxidation product of FeS, although trace thiosulfate ($S_2O_3^{2-}$) and sulfate (SO_4^{2-}) were also identified in aqueous solution. This result is in contrast to FeS oxidation in a biologically active system where remarkable sulfate production and solution acidification take place. The lack of further sulfur oxidation contributed to a relatively stable pH during FeS oxidation reaction. Because elemental sulfur particles were strongly hydrophobic, they tended to

escape aqueous phase and accumulate on water-air interface upon FeS depletion. Therefore, the interactions of elemental sulfur with UO_2 particles were minimized without noticeable impact on UO_2 oxidative dissolution.

7.2 Environmental Implications

7.2.1 Mobility of Uranium at Contaminated Sites

The primary hypothesis of the project, that nanocrystalline mackinawite strongly influences the oxidative dissolution of uraninite by controlling dissolved oxygen levels, has been verified. While much attention has been devoted to the immobilization of low-level soluble U(VI) in groundwater at former mill tailings and Department of Energy Complex sites, the current dissertation presents a timely study in understanding the role of sulfide minerals for maintaining the long-term stability of reduced uranium solids when encountering oxic groundwater intrusion.

Given that bacteria capable of reducing U, Fe, and SO_4^{2-} are ubiquitous in natural environments, FeS and reduced U(IV) solids can be simultaneously produced under sulfate-reducing conditions where Fe(III) minerals and sulfate are frequently encountered. When naturally produced in anoxic sediments, FeS will serve as an oxygen scavenger to maintain low DO levels in the subsurface. Because of the preferential reaction of FeS with oxygen, uraninite remobilization may be inhibited by lowering the DO concentration, as long as the anoxic condition is restored before the complete FeS depletion. Under conditions favoring a large production of mackinawite, a long inhibition period of UO_2 dissolution may be guaranteed even with a high DO concentration (> 7 mg/L). The strategy of FeS generation may be employed and engineered by stimulating the activities of SRB and injecting

necessary sulfate and soluble iron sources (e.g., Fe(II) or ferrihydrite) into subsurface. Within the entire life of the site management, however, constant monitoring of dissolved U and DO concentrations would be necessary to optimize the timing for reproduce FeS in order to keep U immobilized. The periodic maintenance of anoxic condition and FeS generation in contaminated sites may be superior to injecting chemically produced agents, such as zerovalent iron (ZVI), in a permeable reactive barrier (PRB) due to the advantage in energy and chemical conservation and cost reduction.

Despite the success of FeS in inhibiting UO_2 oxidation in the abiotic systems, great challenges exist for scaling experimental results into the field environment in an effective and sustainable manner. Extremely varied geochemical and hydrogeological conditions at U remediation sites likely pose significant challenges on U immobilization. For example, the spatial distribution of FeS and reduced U solids within a subsurface matrix may limit the protective role of FeS. If the enzymatically reduced U is physically apart from FeS precipitates in the porous media, uraninite has a greater chance to be in contact with oxygen and becomes dissolved. The nanoscale UO_2 produced by microorganisms may be mobile in porous sediments and thus more susceptible to oxidation than bulk uraninite. In addition, other co-contaminants, soils matrices, and complexing ligands (e.g., carbonate and DOM) may also influence U mobility while FeS scavenges oxygen and keeps sediments anoxic.

Perhaps the most confounding behavior of uranium at contaminated sites is associated with native microbial populations, which cause the reduction of uranium and sulfate under sulfate reducing conditions. When a dominant anoxic subsurface yields to oxic conditions, sulfur oxidizing bacteria can promote the sulfide oxidation, producing sulfate and protons and noticeably shifting solution pH (Burton et al., 2009). The acidic water may severely

impair FeS reducing capacity and undermine UO_2 stability. Therefore, the possibility of changing geochemical conditions due to microbial activities should be carefully considered when using sulfide minerals as the protector for reduced U. In parallel with uraninite precipitates, non-uraninite biomass-bound U(IV) has been observed in acetate-amended sediments (Fletcher et al., 2010; Bargar et al., 2013). While mackinawite has the potential to reduce the monomeric U(IV) complex, current knowledge is deficient for predicting the mobility of monomeric U(IV) upon interaction with FeS.

7.2.2 Long-term Behavior of Oxidized U Solids

Without the timely restoration of anoxic conditions, uraninite solids will eventually be oxidized by oxygen in the subsurface. When oxidizing condition prevails, the passivation layers on UO_2 surface can play a critical role in controlling the transport and transformation of U(VI) species in groundwater. Thus, the long-term behavior of uranium at a contaminated site will likely be dependent on the dissolution equilibrium and kinetics of UO_2 and secondary U(VI) phases. Ideally, the knowledge of dissolution rate laws and equilibrium solubility will enable the construction of reactive transport model capable of predicting the long-term distribution of uranium among the dissolved and various solid phases.

The accurate prediction of UO_2 stability, as shown in this dissertation, may be complicated by the presence of sulfide minerals that directly govern DO concentrations. A transient phase of fast UO_2 dissolution may occur when UO_2 surfaces remain reduced and DO increases, as long as the U(VI) detachment step is faster than UO_2 surface oxidation. The rapid U release may cause considerable U spread in groundwater and soils, exceeding the rate estimated from the current model of UO_2 oxidative dissolution at circumneutral pH. In

the field, other reactive mineral phases capable of scavenging DO may also facilitate in preserving the UO_2 surface from passivation. A number of complexing ligands, including carbonate and DOM, may enhance the overall dissolution rate of UO_2 in the subsurface. Because the hydraulic residence time of groundwater varies from years to decades, the slow flow may allow a long period of low DO concentration and sluggish diffusion of soluble U(VI) species to downstream before UO_2 surfaces become passivated by the elevated oxygen concentration. More importantly, because soil minerals in the subsurface cannot move freely, the impact of FeS on UO_2 oxidation and dissolution processes would be spatially and temporally localized. The dissolved U(VI) species from the upstream may slowly travel with the flow of groundwater unless they are retained by the mineral phases or reduced by microorganisms in the downstream environment.

Unlike previous studies performed under reducing conditions (Sani et al., 2005; Ginder-Vogel et al., 2010), Fe(III) hydroxides and elemental sulfur do not appear to pose an additional risk of UO_2 mobilization under oxic conditions, although they may serve as additional adsorbents of soluble U(VI). It should be noted that the transformation of FeS to Fe(III) solids are unlikely to play a key role in U retention, given that Fe(III) hydroxide minerals are usually already the most common mineral phases in the subsurface. The complexing ligands in groundwater, including calcium and carbonate, may limit U(VI) adsorption through their interactions with uranyl species to form stable complexes, especially under oxic conditions. When exceeding the solubility of uranyl minerals, however, the precipitation of secondary U(VI) solid phases, such as liebigite, may occur to control the dissolution rate of UO_2. When oxidizing condition is unavoidable, procedures that promote UO_2 surface passivation may be practiced to limit the UO_2 dissolution rate.

7.3 Recommendations for Future Work

7.3.1 Extension to Different Materials and Solution Conditions

Because of the complexity of soil mineralogy and U speciation in the subsurface, new information and trends would be revealed by extending the approaches described in this dissertation to different types of iron sulfide minerals, reduced U(IV) species, and solution compositions:

1. Other metastable iron sulfide minerals, including pyrrhotite and greigite, can be investigated for their reactivity with uraninite and dissolved oxygen. The transformation of these sulfide minerals into more stable mineral phases under oxic and anoxic conditions can also have important implications for geochemical cycling of sulfur and uranium in the environment.
2. Monomeric U(IV) complexes produced via microbial U(VI) reduction can be examined for their stability and mobility after interacting with mackinawite. The potentially important U(IV) species in the field may exhibit different mechanisms and kinetics of oxidation and dissolution during anoxic-oxic transitions as compared to uraninite.
3. Groundwater containing complexing ligands, such as dissolved organic matter and siderophore, can be evaluated for their role in influencing FeS and UO_2 solubility and transformation under anoxic and oxic conditions. In particular, the influence of Ca-UO_2-CO_3 complexes on U stability and U(VI) detachment can be studied by systematically varying Ca^{2+} and CO_3^{2-} concentrations under constant pH values.

7.3.2 Extension to the Field Environment

Because the current research is mainly based on laboratory-scale experiments, applications of the results to environmental systems may be limited. By working with natural sediments besides synthetic minerals, aspects of environmental complexity could be addressed. Instead of using component additivity approaches to predict U stability in heterogeneous systems, direct measurements of the mobility of U in the field samples could serve to further constrain reactive transport models.

A bench-scale column experiment using Rifle or Hanford sediments may be a good starting point for evaluating the geochemical heterogeneity of a porous media. The U mobility can be studied in unsaturated soils subjected to repeated wetting and drying cycles in the field and analog laboratory systems. Although FeS may continue to serve as an oxidant scavenger, frequent redox cycles may cause redistribution of uranium and precipitation of U(VI) secondary phases. Over redox reactions, the aqueous and solid phase characterization techniques applied in this dissertation research can be utilized.

Given that iron sulfides and uraninite are most effectively produced by iron- and sulfate-reducing bacteria in natural environments, a comprehensive understanding of U stability will not be complete without the consideration of microbial activities. Biogenic iron sulfide and uraninite solids generated by different strains of SRB can be investigated for their reactivity with oxygen and complexing ligands, which provide a comparison with the abiotic counterparts. Stimulation of SRB activity in sediment columns can be conducted to determine the maximum production of FeS for U(VI) reduction. The goal would be to understand the relative contribution of biotic and abiotic processes that control U transformation and mobility in the field.

Appendix A

Thermodynamic Database

The aquatic chemistry of uranium is very complex and the available thermodynamic database is still subject to considerable uncertainty. The uncertainty of the thermodynamic database has been considered an important limiting factor in equilibrium modeling and reactive transport modeling. For the purpose of comparing the results between studies, a consistent database of thermodynamic constants is essential. In this appendix, the thermodynamic constants for dissolved and solid uranium species which commonly present in the groundwater are summarized.

Most stability constants of dissolved uranium species in the present work are from the NEA database (Guillaumont et al., 2003) with the exception of the constant for ternary Ca-UO_2-CO_3 complexes (Dong and Brooks, 2006). All constants were compared with the native database of the chemical equilibrium software application Visual MINTEQ (version 3.1). Necessary update was made on the software database to include the most recently published data. Additional reactions (e.g., acid-base) used in equilibrium calculations used the default constants in the software database.

Table A. 1 Thermodynamic constants of aqueous uranium species used in Visual MINTEQ simulation.

Reaction	**Log β* (I = 0)**	**$\Delta_r H^0_m$ (kJ.mol^{-1})**
$UO_2^{2+} + H_2O = UO_2OH^+ + H^+$	-5.25	
$UO_2^{2+} + 2H_2O = UO_2(OH)_2(aq) + 2H^+$	-12.15	
$UO_2^{2+} + 3H_2O = UO_2(OH)_3^- + 3H^+$	-20.25	
$UO_2^{2+} + 4H_2O = UO_2(OH)_4^{2-} + 4H^+$	-32.4	
$2UO_2^{2+} + H_2O = (UO_2)_2OH^{3+} + H^+$	-2.70	
$2UO_2^{2+} + 2H_2O = (UO_2)_2(OH)_2^{2+} + 2H^+$	-5.62	
$3UO_2^{2+} + 4H_2O = (UO_2)_3(OH)_4^{2+} + 4H^+$	-11.90	
$3UO_2^{2+} + 5H_2O = (UO_2)_3(OH)_5^+ + 5H^+$	-15.55	
$3UO_2^{2+} + 7H_2O = (UO_2)_3(OH)_7^- + 7H^+$	-32.2	
$4UO_2^{2+} + 7H_2O = (UO_2)_4(OH)_7^+ + 7H^+$	-21.9	
$UO_2^{2+} + CO_3^{2-} = UO_2CO_3(aq)$	9.94	5.0 ± 2.0
$UO_2^{2+} + 2CO_3^{2-} = UO_2(CO_3)_2^{2-}$	16.61	18.5 ± 4.0
$UO_2^{2+} + 3CO_3^{2-} = UO_2(CO_3)_3^{4-}$	21.84	-39.2 ± 4.1
$UO_2^+ + 3CO_3^{2-} = UO_2(CO_3)_3^{5-}$	6.95 ± 0.36	
$3UO_2^{2+} + 6CO_3^{2-} = (UO_2)_3(CO_3)_6^{6-}$	54 ± 1	-62.7 ± 2.4
$U(CO_3)_5^{6-} = CO_3^{2-} + U(CO_3)_4^{4-}$	1.12	
$U^{4+} + 5CO_3^{2-} = U(CO_3)_5^{6-}$	34.0	-20.0
$2UO_2^{2+} + CO_2(g) + 4H_2O = (UO_2)_2CO_3(OH)_3^- + 5H^+$	-19.01	
$3UO_2^{2+} + CO_2(g) + 4H_2O = (UO_2)_3O(OH)_2(HCO3)^+ + 5H^+$	-17.5 ± 0.5	
$11UO_2^{2+} + 6CO_2(g) + 18H_2O = (UO_2)_{11}(CO_3)_6(OH)_{12}^{2-} + 24H^+$	-72.5 ± 2.0	
$2UO_2^{2+} + CO_3^{2-} + 3H_2O = (UO_2)_2CO_3(OH)_3^- + 3H^+$	-0.855	
$Ca^{2+} + UO_2^{2+} + 3CO_3^{2-} = CaUO_2(CO_3)_3^{2-}$	27.4†	
$2Ca^{2+} + UO_2^{2+} + 3CO_3^{2-} = Ca_2UO_2(CO_3)_3(aq)$	30.70†	
$UO_2^{2+} + Cl^- = UO_2Cl^+$	0.17 ± 0.02	8.0 ± 2.0
$UO_2^{2+} + 2Cl^- = UO_2Cl_2(aq)$	-1.10 ± 0.4	15.0 ± 6.0
$H_2O(l) + U^{4+} = H^+ + UOH^{3+}$	-0.54	
$4OH^- + U^{4+} = U(OH)_4(aq)$	46.0	
$U^{4+} + 2CO_3^{2-} + 2OH^- = U(OH)_2(CO_3)_2^{2-}$	42.4	
$SO_3^{2-} + UO_2^{2+} = UO_2SO_3$ (aq)	6.6 ± 0.6	
$S_2O_3^{2-} + UO_2^{2+} = UO_2S_2O_3$ (aq)	2.8 ± 0.3	
$SO_4^{2-} + UO_2^{2+} = UO_2SO_4$ (aq)	3.15 ± 0.02	19.5 ± 1.6
$SO_4^{2-} + U^{4+} = USO_4^{2+}$ (aq)	6.58 ± 0.19	8.0
$2SO_4^{2-} + U^{4+} = U(SO_4)_2$ (aq)	10.51 ± 0.2	32.7
$2SO_4^{2-} + UO_2^{2+} = UO_2(SO_4)_2^{2-}$(aq)	4.14 ± 0.07	35.1 ± 1.0
$3SO_4^{2-} + UO_2^{2+} = UO_2(SO_4)_3^{4-}$(aq)	3.02 ± 0.38	

Table A.2 Possible solid phases and their solubilities considered in Visual MINTEQ simulations.

Solid Phase	**Dissolution Reaction**	**Log K (*I* = 0)**
Aragonite	$CaCO_3$ (s) = Ca^{2+} + CO_3^{2-}	-8.063
becquerelite	$Ca(UO_2)_6O_4(OH)_6$•$8H_2O$+ $14H^+$ = Ca^{2+} + $6UO_2^{2+}$+$18H_2O$	2.302
Calcite	$CaCO_3$ (s) = Ca^{2+} + CO_3^{2-}	-8.063
$Fe(OH)_2$ (am)	$Fe(OH)_2$ (am) + $2H^+$ = Fe^{2+} + $2H_2O$	8.869
$Fe(OH)_2$ (c)	$Fe(OH)_2$ (c) + $2H^+$ = Fe^{2+} + $2H_2O$	8.869
Halite	NaCl (s) = Na^+ + Cl^-	-4.491
KCl(s)	KCl (s) = K^+ + Cl^-	-5.79
liebigite	$Ca_2UO_2(CO_3)_3$•$11H_2O$ = $2Ca^{2+}$ + $3CO_3^{2-}$ +UO_2^{2+}+$11H_2O$	-37.09
Lime	CaO (s) + $2H^+$ = Ca^{2+} + H_2O	11.387
Natron	Na_2CO_3•$10H_2O$ = $2Na^+$ + CO_3^{2-} + $10H_2O$	-9.481
Portlandite	$Ca(OH)_2$ (s) $2H^+$ = Ca^{2+} + $2H_2O$	11.387
Rutherfordine	$UO_2(CO_3)$ (s) + $2H^+$ = UO_2^{2+} + CO_3^{2-}	-20.964
Schoepite	UO_3•$2H_2O$ + $2H^+$ = UO_2^{2+} + $3H_2O$	-1.514
Siderite	$FeCO_3$(s) = Fe^{2+} + CO_3^{2-}	-10.581
Thermonatrite	Na_2CO_3•H_2O = $2Na^+$ + CO_3^{2-} + H_2O	-9.481
$UO_2(OH)_2$ (beta)	$UO_2(OH)_2$ (beta) + $2H^+$ = UO_2^{2+} + $2H_2O$	-1.514
UO_3(s)	UO_3(s) + $2H^+$ = UO_2^{2+} + H_2O	-1.514
$Fe_3(OH)_8$(s)	$Fe_3(OH)_8$(s) + $8H^+$ = Fe^{2+} + $2Fe^{3+}$ + $8H_2O$	2.530
Ferrihydrite	$Fe(OH)_3$ (am) + $3H^+$ = Fe^{3+} + $3H_2O$	-3.169
Ferrihydrite (aged)	$Fe(OH)_3$ (aged) + $3H^+$ = Fe^{2+} + $3H_2O$	-3.169
Goethite	FeOOH + $3H^+$ = Fe^{3+} + $2H_2O$	-3.169
Hematite	Fe_2O_3 + $6H^+$ = $2Fe^{3+}$ + $3H_2O$	-6.339
Lepidocrocite	FeOOH + $3H^+$ = Fe^{3+} + $2H_2O$	-3.169

Table A.3 Half-reactions of U(IV)/U(VI) and Fe(II)/Fe(III) redox couples and the corresponding standard electrode potentials. U(VI) and Fe(II) species are based on the predominant dissolved species predicted by Visual MINTEQ.

Reaction	**E ℃(v)**
$Ca_2UO_2(CO_3)_3(aq)+3\ H^+ + 2e^- = UO_2(s)+3\ HCO_3^- + 2\ Ca^{2+}$	0.278 §
$CaUO_2(CO_3)_3^{2-}+3\ H^+ + 2e^- = UO_2(s)+3\ HCO_3^- + Ca^{2+}$	0.427 §
$0.5\ UO_2(CO_3)_3^{4-}(aq) + 1.5\ H^+ + e^- = 0.5\ UO_2(s)+1.5\ HCO_3^-$	0.687
$Fe(OH)_3(s)(fresh) +3H^+ + e^- = Fe^{2+}(aq) + 3H_2O$	1.064
$FeOOH(s) + 3H^+ + e^- = Fe^{2+}(aq) + 2H_2O$	0.799

Reference: §(Gavrilescu et al., 2009).

Table A.4 Calculated Gibb's free energy of redox reactions at standard state conditions ($\Delta G_r°$) and at experimental conditions at pH 6, 7 and 8 in flow-through experiments (ΔG_r^*).

Reactions*	**$\Delta G_r°$ (kJ mol^{-1})§**	**ΔG_r^* (kJ mol^{-1})¶**		
	pH 6- 8	**pH 6**	**pH 7**	**pH 8**
$Fe(OH)_3(s) + 0.5UO_2 + 1.5H^+ + 1.5HCO_3^- + Ca^{2+} \leftrightarrow 0.5Ca_2UO_2(CO_3)_3(aq) + Fe^{2+} + 3H_2O$	-59.39	-7.25	-14.03	-4.17
$Fe(OH)_3(s) + 0.5UO_2 + 1.5H^+ + 1.5HCO_3^- + 0.5Ca^{2+} \leftrightarrow 0.5CaUO_2(CO_3)_3^{2-} + Fe^{2+} + 3H_2O$	-49.35	-6.91	-13.69	-3.82
$Fe(OH)_3(s) + 0.5UO_2 + 2.5H^+ + 0.5HCO_3^- \leftrightarrow 0.5UO_2CO_3(aq) + Fe^{2+} + 3H_2O$	-59.21	-6.92	-13.71	-3.84
α-$FeOOH + 0.5UO_2 + 1.5H^+ + 1.5HCO_3^- + Ca^{2+} \leftrightarrow 0.5Ca_2UO_2(CO_3)_3(aq) + Fe^{2+} + 2H_2O$	-41.81	10.33	3.55	13.42
α-$FeOOH + 0.5UO_2 + 1.5H^+ + 1.5HCO_3^- + 0.5Ca^{2+} \leftrightarrow 0.5CaUO_2(CO_3)_3^{2-} + Fe^{2+} + 2H_2O$	-31.77	10.67	3.89	13.76
γ-$FeOOH + 0.5UO_2 + 1.5H^+ + 1.5HCO_3^- + Ca^{2+} \leftrightarrow 0.5Ca_2UO_2(CO_3)_3(aq) + Fe^{2+} + 2H_2O$	-50.61	1.53	-5.25	4.62
γ-$FeOOH + 0.5UO_2 + 1.5H^+ + 1.5HCO_3^- + 0.5Ca^{2+} \leftrightarrow 0.5CaUO_2(CO_3)_3^{2-} + Fe^{2+} + 2H_2O$	-40.57	1.87	-4.91	4.96

* Only three Fe(III) hydroxides, i.e., ferrihydrite, goethite and lepidocrocite, are considered for the redox reactions with uraninite. The selection of Fe(III) solids was based on the experimental results in Chapter 4 and 5.The dominant dissolved uranyl species were predicted to be $Ca_2UO_2(CO_3)_3(aq)$, $CaUO_2(CO_3)_3^{2-}$, and $UO_2CO_3(aq)$ at pH 6, $Ca_2UO_2(CO_3)_3(aq)$, $CaUO_2(CO_3)_3^{2-}$ for pH 7 and 8.

§ At standard state conditions, the Gibbs free energy of the reactions is the same at any pH. Gibbs free energies of formation for all uranium species were obtained from Guillaumont et al. (2003) except for the Ca-UO_2-CO_3 species (Dong and Brooks, 2006). Gibbs free energy of formation for iron hydroxides were obtained from (Majzlan et al., 2003) and (Majzlan et al., 2004). The Gibbs free energy of formation for all other dissolved species were obtained from (Morel and Hering, 1993).

¶The experimental condition at pH 6 is 0.5×10^{-6} M U(VI) species, 0.1×10^{-3} M Fe^{2+}, 1×10^{-3} M HCO_3^-, and 2×10^{-3} M Ca^{2+} ; pH 7 experimental conditions 0.5×10^{-6} M U(VI) species, 5×10^{-6} M Fe^{2+}, 1×10^{-2} M HCO_3^-, and 2×10^{-3} M Ca^{2+}; pH 8 experimental conditions 0.5×10^{-6} M U(VI) species, 1×10^{-7} M Fe^{2+}, 5×10^{-4} M HCO_3^-, and 1.5×10^{-3} M Ca^{2+}.

Appendix B

FeS Batch Control Experiment Results

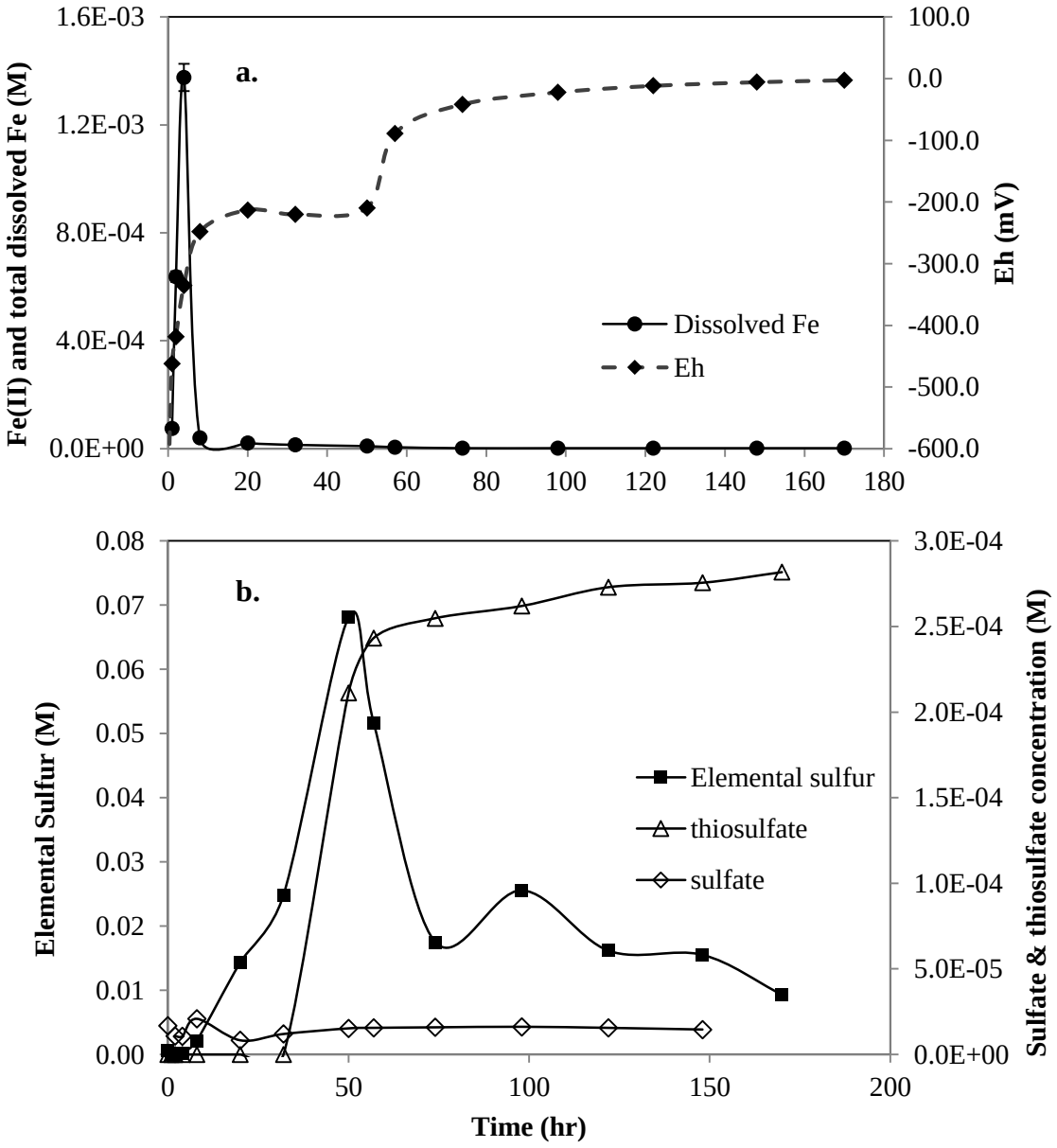

Figure B.1 The kinetic profiles of (a) total dissolved Fe and Eh; (b) sulfur species, i.e., elemental sulfur, thiosulfate, and sulfate during control experiment in the presence of only FeS. Experimental conditions: 5.0 g/L FeS; 4.0 mM $NaHCO_3$, 0.4 mM KCl, and 2.0 mM $CaCl_2$, the solution is equilibrated with 2% P_{O2}, 5% P_{CO2} gas mixture.

Appendix C

XPS Spectra of FeS and UO_2 Oxidation Products

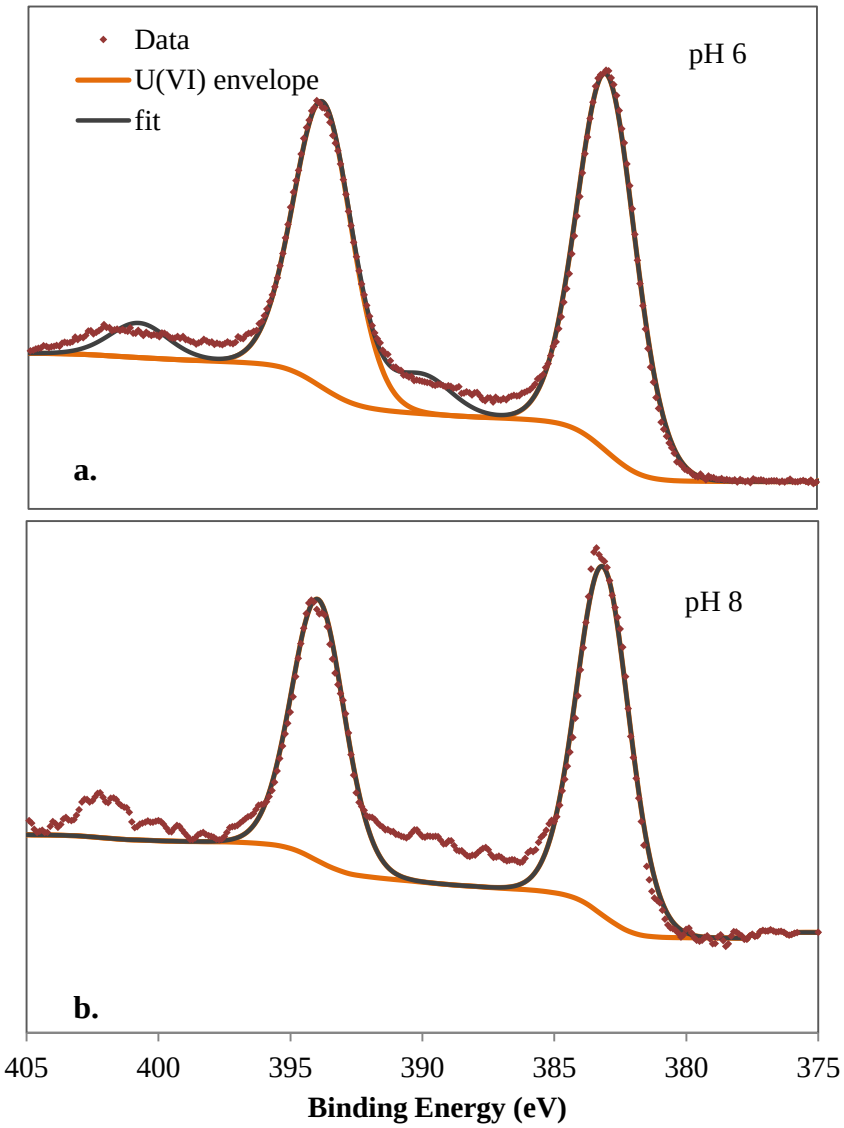

Figure C.1 Deconvolution of representative U 4f XPS spectra of CSTR samples after complete FeS oxidation (a) 82 τ at pH = 6.1; (b) 106 τ at pH = 8.1. The surface U has been completely oxidized to U(VI) oxidation state by the time of reaction. Both were collected in the same sequence of samples shown in Figure 6.8 of Chapter 6, where experiments were carried out under 4.8 mM FeS and DO = 1.8 mg/L groundwater conditions.

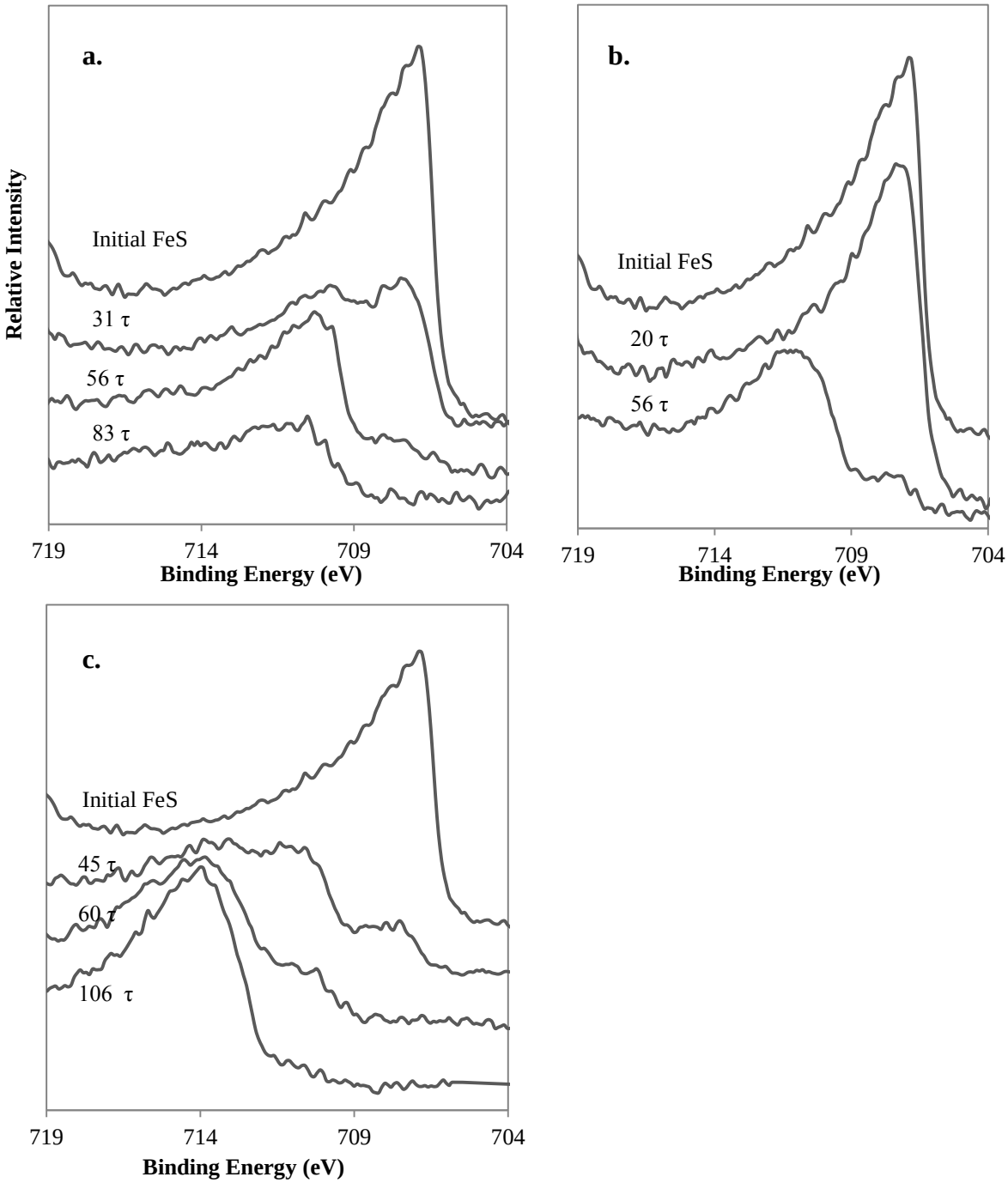

Figure C.2 Narrow scans of Fe $2p_{3/2}$ XPS spectra for the initial FeS and oxidized FeS samples collected as a function of time at pH 6 (a), 7 (b), and 8 (c) flow-through experiments. The U 4f XPS spectra of corresponding samples were reported in Figure 6.8 in Chapter 6. The spectra were only calibrated without fitting.

The initial FeS shows a Fe $2p_{3/2}$ spectra dominated by ~706.8 eV peak, which was identified as the Fe(II)-S component (Mullet et al., 2002; Jeong et al., 2010a). The broad tailing feature at the binding energy of 708–714 eV has been attributed to the surface Fe^{3+} species, possibly due to the trace Fe(III)-S multiplets in FeS.

When FeS is oxidized by DO, the binding energy of the Fe $2p_{3/2}$ peak shifts to higher energies at all pH values in this study (Figure B.1). At pH 6 and 7, the decreased Fe(II)-S peak at ~706.8 eV is accompanied by an increasing peak in the range of 709–711 eV, which can be attributed to the growing Fe(III)-S component (Jeong et al., 2010a). Because significant loss of Fe occurred at pH 6 due to FeS dissolution, the peak intensity of 83 τ sample at 710.6 eV was reduced as compared to the earlier samples. The oxidized surface Fe also exhibit broadened XPS spectra, indicating a combination of mixed Fe(III) species. The tailing at binding energy greater than 711 eV was previously attributed to the Fe(III)-O species on oxidized FeS (Jeong et al., 2010a).

At pH 8, the Fe species at mackinawite surface shows a significantly different feature after oxidation compared with the pH 6 and 7 experiments (Figure B.1c). While an intermediate sample exhibits a similar Fe(III)-S phase at ~710.5 eV after 45 τ reaction, the Fe $2p_{3/2}$ spectra eventually shifted to a higher binding energy of ~714 eV after 60 τ in the flow-through experiment. The Fe(III)-O component gradually became a dominant surface species at pH 8, possibly due to the formation of Fe(III) hydroxide coating on FeS surface. The dominance of Fe(III)-O surface species after FeS oxidation was not observed at lower pH values where Fe(III)-S species was more prominent. The disparate surface Fe species observed by XPS Fe $2p_{3/2}$ spectra suggest the different FeS oxidation pathways occurring at the three pH values, which may affect the oxygen scavenging efficiency in groundwater.

Appendix D

Additional Solid Phase Characterization

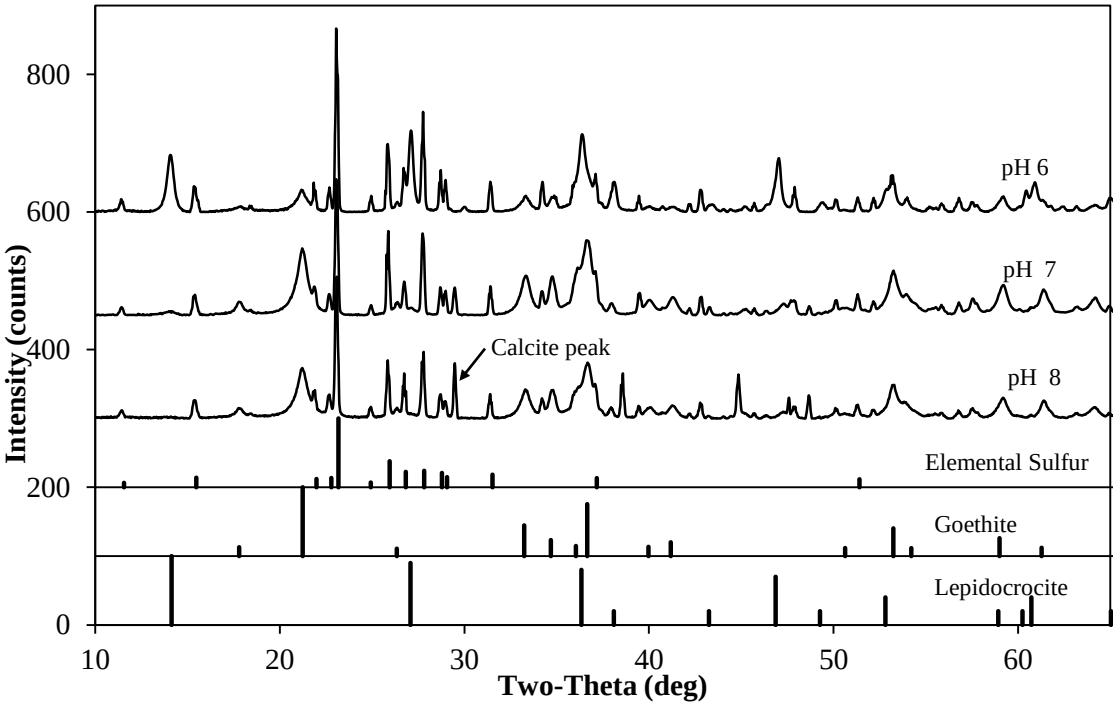

Figure D.1 XRD patterns of final solid samples collected from CSTR at pH 6, 7, and 8 after FeS has been completely oxidized by 7.8 mg/L DO in simulated groundwater. Calcite precipitates were identified at pH 8 by a characteristic (*104*) peak at ~29.5° 2θ.

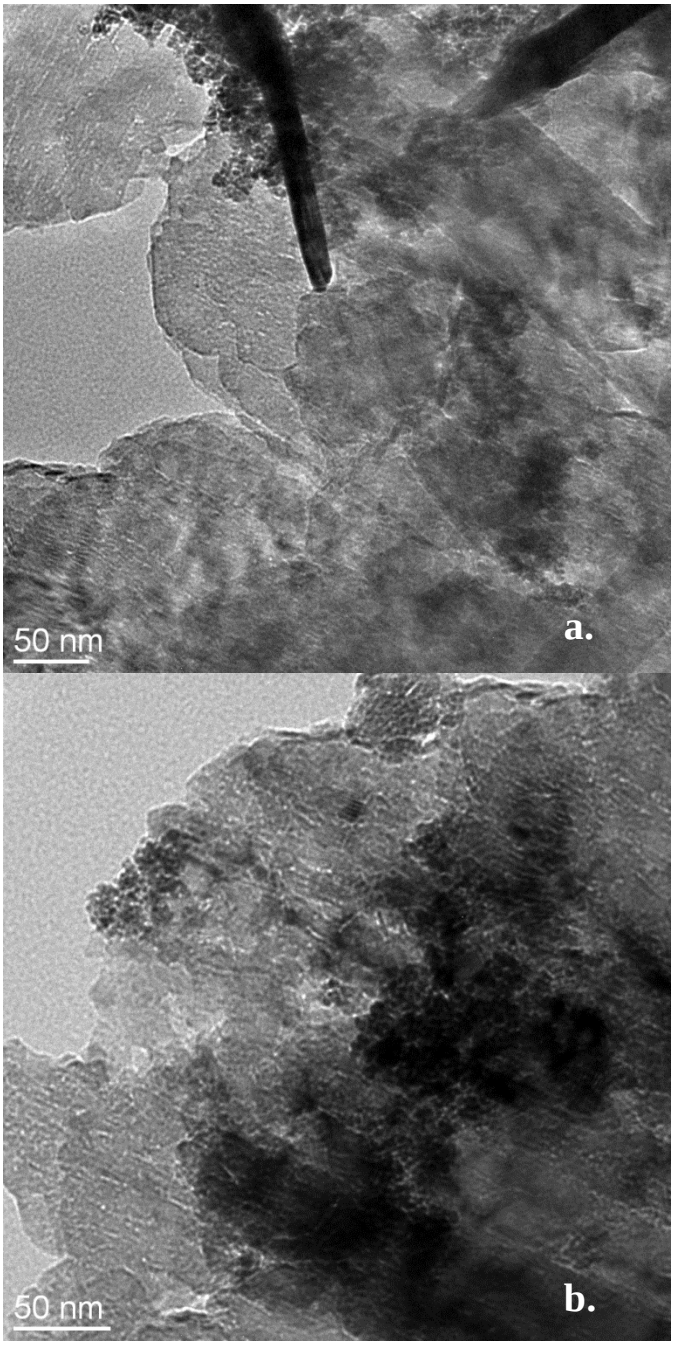

Figure D.2 TEM images of CSTR samples collected at 106 τ of pH 8 CSTR experiment after complete FeS oxidation. (a) BF image at 40 K magnification; (b) BF image at 80 K magnification of the same material. Both images shows platelet materials comprised of calcite precipitates. The samples were dried inside an anaerobic chamber prior to TEM analysis.

References

Abdelouas, A., 2006. Uranium mill tailings: Geochemistry, mineralogy, and environmental impact. *Elements* **2**, 335-341.

Abdelouas, A., Lutze, W., Gong, W., Nuttall, E. H., Strietelmeier, B. A., and Travis, B. J., 2000. Biological reduction of uranium in groundwater and subsurface soil. *Sci. Total Environ.* **250**, 21-35.

Abdelouas, A., Lutze, W., and Nuttall, E., 1998. Chemical durability of uraninite precipitated on Navajo sandstone. *Comptes Rendus De L Academie Des Sciences Serie Ii Fascicule a-Sciences De La Terre Et Des Planetes* **327**, 101-106.

Abdelouas, A., Lutze, W., and Nuttall, H. E., 1999a. Oxidative dissolution of uraninite precipitated on Navajo sandstone. *J. Contam. Hydrol.* **36**, 353-375.

Abdelouas, A., Lutze, W., and Nuttall, H. E., 1999b. Uranium contamination in the subsurface: characterization and remediation. *Rev. Mineral. Geochem.* **38**, 433-473.

Aller, R. C. and Rude, P. D., 1988. Complete oxidation of solid-phase sulfides by manganese and bacteria in anoxic marine-sediments. *Geochim. Cosmochim. Acta* **52**, 751-765.

Bargar, J. R., Bernier-Latmani, R., Giammar, D. E., and Tebo, B. M., 2008. Biogenic uraninite nanoparticles and their importance for uranium remediation. *Elements* **4**, 407-412.

Bargar, J. R., Reitmeyer, R., and Davis, J. A., 1999. Spectroscopic confirmation of uranium(VI)-carbonato adsorption complexes on hematite. *Environ. Sci. Technol.* **33**, 2481-2484.

Bargar, J. R., Reitmeyer, R., Lenhart, J. J., and Davis, J. A., 2000. Characterization of U(VI)-carbonato ternary complexes on hematite: EXAFS and electrophoretic mobility measurements. *Geochim. Cosmochim. Acta* **64**, 2737-2749.

Bargar, J. R., Williams, K. H., Campbell, K. M., Long, P. E., Stubbs, J. E., Suvorova, E. I., Lezama-Pacheco, J. S., Alessi, D. S., Stylo, M., Webb, S. M., Davis, J. A., Giammar, D. E., Blue, L. Y., and Bernier-Latmani, R., 2013. Uranium redox transition pathways in acetate-amended sediments. *Proc. Natl. Acad. Sci. U. S. A.* **110**, 4506-4511.

Barnett, M. O., Jardine, P. M., Brooks, S. C., and Selim, H. M., 2000. Adsorption and transport of uranium(VI) in subsurface media. *Soil Science Society of America Journal* **64**, 908-917.

Behrends, T. and Van Cappellen, P., 2005. Competition between enzymatic and abiotic reduction of uranium(VI) under iron reducing conditions. *Chem. Geol.* **220**, 315-327.

Belzile, N., Chen, Y. W., Cai, M. F., and Li, Y. R., 2004. A review on pyrrhotite oxidation. *Journal of Geochemical Exploration* **84**, 65-76.

Benning, L. G., Wilkin, R. T., and Barnes, H. L., 2000. Reaction pathways in the Fe-S system below 100 degrees C. *Chem. Geol.* **167**, 25-51.

Berner, R. A., 1964. Iron sulfides formed from aqueous solution at low temperatures and atmospheric pressure. *The Journal of Geology* **72**, 293-306.

Berner, R. A., 1967. thermodynamic stability of sedimentary iron sulfides. *American Journal of Science* **265**, 773-785.

Berner, R. A., 1970. Sedimentary pyrite formation. *American Journal of Science* **268**, 1-23.

Berner, R. A., 1981. A new geochemical classification of sedimentary environments. *Journal of Sedimentary Research* **51**, 359-365.

Bernier-Latmani, R., Veeramani, H., Vecchia, E. D., Junier, P., Lezama-Pacheco, J. S., Suvorova, E. I., Sharp, J. O., Wigginton, N. S., and Bargar, J. R., 2010. Non-uraninite Products of Microbial U(VI) Reduction. *Environ. Sci. Technol.* **44**, 9456-9462.

Beyenal, H., Sani, R. K., Peyton, B. M., Dohnalkova, A. C., Amonette, J. E., and Lewandowski, Z., 2004. Uranium immobilization by sulfate-reducing biofilms. *Environ. Sci. Technol.* **38**, 2067-2074.

Bi, Y. and Hayes, K. F., 2013. Nano-FeS inhibits UO_2 reoxidation under varied oxic conditions. *Environ. Sci. Technol.* **48**, 632-640.

Bi, Y., Hyun, S. P., Kukkadapu, R. K., and Hayes, K. F., 2013. Oxidative dissolution of UO_2 in a simulated groundwater containing synthetic nanocrystalline mackinawite. *Geochim. Cosmochim. Acta* **102**, 175-190.

Boland, D. D., Collins, R. N., Payne, T. E., and Waite, T. D., 2011. Effect of Amorphous Fe(III) Oxide Transformation on the Fe(II)-Mediated Reduction of U(VI). *Environ. Sci. Technol.* **45**, 1327-1333.

Boursiquot, S., Mullet, M., Abdelmoula, M., Genin, J. M., and Ehrhardt, J. J., 2001. The dry oxidation of tetragonal FeS1-x mackinawite. *Phys. Chem. Miner.* **28**, 600-611.

Boyanov, M. I., Fletcher, K. E., Kwon, M. J., Rui, X., O'Loughlin, E. J., Löffler, F. E., and Kemner, K. M., 2011. Solution and microbial controls on the formation of reduced U(IV) species. *Environ. Sci. Technol.* **45**, 8336-8344.

Boyanov, M. I., O'Loughlin, E. J., Roden, E. E., Fein, J. B., and Kemner, K. M., 2007. Adsorption of Fe(II) and U(VI) to carboxyl-functionalized microspheres: The

influence of speciation on uranyl reduction studied by titration and XAFS. *Geochim. Cosmochim. Acta* **71**, 1898-1912.

Bruno, J., Casas, I., and Puigdomènech, I., 1991. The kinetics of dissolution of UO_2 under reducing conditions and the influence of an oxidized surface layer (UO2+x): Application of a continuous flow-through reactor. *Geochim. Cosmochim. Acta* **55**, 647-658.

Buckley, A. N. and Woods, R., 1985. An x-ray photoelectron spectroscopic study of the oxidation of galena. *Applications of Surface Science* **17**, 401-414.

Burton, E. D., Bush, R. T., and Sullivan, L. A., 2006. Acid-volatile sulfide oxidation in coastal flood plain drains: Iron−sulfur cycling and effects on water quality. *Environ. Sci. Technol.* **40**, 1217-1222.

Burton, E. D., Bush, R. T., Sullivan, L. A., Hocking, R. K., Mitchell, D. R. G., Johnston, S. G., Fitzpatrick, R. W., Raven, M., McClure, S., and Jang, L. Y., 2009. Iron-monosulfide oxidation in natural sediments: resolving microbially mediated S transformations using XANES, electron microscopy, and selective extractions. *Environ. Sci. Technol.* **43**, 3128-3134.

Butler, E. C. and Hayes, K. F., 1998. Effects of solution composition and pH on the reductive dechlorination of hexachloroethane by iron sulfide. *Environ. Sci. Technol.* **32**, 1276-1284.

Butler, E. C. and Hayes, K. F., 2001. Factors influencing rates and products in the transformation of trichloroethylene by iron sulfide and iron metal. *Environ. Sci. Technol.* **35**, 3884-3891.

Campbell, K. M., Veeramani, H., Ulrich, K.-U., Blue, L. Y., Giammar, D. E., Bernier-Latmani, R., Stubbs, J. E., Suvorova, E., Yabusaki, S., Lezama-Pacheco, J. S., Mehta, A., Long, P. E., and Bargar, J. R., 2011. Oxidative dissolution of biogenic uraninite in groundwater at Old Rifle, CO. *Environ. Sci. Technol.* **45**, 8748-8754.

Canfield, D. E., 1989. Reactive iron in marine sediments. *Geochim. Cosmochim. Acta* **53**, 619-632.

Canfield, D. E. and Berner, R. A., 1987. Dissolution and pyritization of magnetite in anoxie marine sediments. *Geochim. Cosmochim. Acta* **51**, 645-659.

Canfield, D. E., Thamdrup, B., and Fleischer, S., 1998. Isotope fractionation and sulfur metabolism by pure and enrichment cultures of elemental sulfur-disproportionating bacteria. *Limnology and Oceanography* **43**, 253-264.

Casas, I., de Pablo, J., Gimenez, J., Torrero, M. E., Bruno, J., Cera, E., Finch, R. J., and Ewing, R. C., 1998. The role of pe, pH, and carbonate on the solubility of UO2 and uraninite under nominally reducing conditions. *Geochim. Cosmochim. Acta* **62**, 2223-2231.

Casas, I., Gimenez, J., Marti, V., Torrero, M. E., and Depablo, J., 1994. Kinetic-studies of unirradiated UO_2 dissolution under oxidizing conditions in batch and flow experiments. *Radiochim. Acta* **66-7**, 23-27.

Cerrato, J. M., Ashner, M. N., Alessi, D. S., Lezama-Pacheco, J. S., Bernier-Latmani, R., Bargar, J. R., and Giammar, D. E., 2013. Relative reactivity of biogenic and chemogenic uraninite and biogenic noncrystalline U(IV). *Environ. Sci. Technol.* **47**, 9756-9763.

Chirita, P., 2009. Iron monosulfide (FeS) oxidation by dissolved oxygen: characteristics of the product layer. *Surf. Interface Anal.* **41**, 405-411.

Chirita, P., Descostes, M., and Schlegel, M. L., 2008. Oxidation of FeS by oxygen-bearing acidic solutions. *J. Colloid Interface Sci.* **321**, 84-95.

Coles, C. A., Rao, S. R., and Yong, R. N., 2000. Lead and cadmium interactions with mackinawite: Retention mechanisms and the role of pH. *Environ. Sci. Technol.* **34**, 996-1000.

Conradson, S. D., Manara, D., Wastin, F., Clark, D. L., Lander, G. H., Morales, L. A., Rebizant, J., and Rondinella, V. V., 2004. Local structure and charge distribution in the UO2-U4O9 system. *Inorg. Chem.* **43**, 6922-6935.

Cornell, R. M. and Schwertmann, U., 2003. The iron oxides: structure, properties, reactions, occurrences, and uses. Wiley-VCH, Weinheim.

de Pablo, J., Casas, I., Gimenez, J., Clarens, F., Duro, L., and Bruno, J., 2004. The oxidative dissolution mechanism of uranium dioxide. The effect of pH and oxygen partial pressure. *Scientific Basis for Nuclear Waste Management Xxvii* **807**, 83-88.

de Pablo, J., Casas, I., Gim énez, J., Mart í, V., and Torrero, M. E., 1996. Solid surface evolution model to predict uranium release from unirradiated UO_2 and nuclear spent fuel dissolution under oxidizing conditions. *J. Nucl. Mater.* **232**, 138-145.

De Pablo, J., Casas, I., Gimenez, J., Molera, M., Rovira, M., Duro, L., and Bruno, J., 1999. The oxidative dissolution mechanism of uranium dioxide. I. The effect of temperature in hydrogen carbonate medium. *Geochim. Cosmochim. Acta* **63**, 3097-3103.

DOE, 1997. Linking Legacies: Connecting the Cold War Nuclear Weapons Processes to Their Environmental Consequences. Department of Energy, Washington, D.C.

DOE, 1998. Accelerating Cleanup: Paths to Closure, Washington, D.C.

Dong, W. M. and Brooks, S. C., 2006. Determination of the formation constants of ternary complexes of uranyl and carbonate with alkaline earth metals (Mg^{2+}, Ca^{2+}, Sr^{2+}, and Ba^{2+}) using anion exchange method. *Environ. Sci. Technol.* **40**, 4689-4695.

Du, X., Boonchayaanant, B., Wu, W. M., Fendorf, S., Bargar, J., and Criddle, C. S., 2011. Reduction of Uranium(VI) by Soluble Iron(II) Conforms with Thermodynamic Predictions. *Environ. Sci. Technol.* **45**, 4718-4725.

Elsner, M., Schwarzenbach, R. P., and Haderlein, S. B., 2004. Reactivity of Fe(II)-bearing minerals toward reductive transformation of organic contaminants. *Environ. Sci. Technol.* **38**, 799-807.

EPA, U. S., 2000. Final rule for (non-radon) radionuclides in drinking water. In: Agency, U. S. E. P. (Ed.). Office of Water.

Finch, R. and Murakami, T., 1999. Systematics and Paragenesis of Uranium Minerals. *Reviews in Mineralogy <D>* **38**, 91-179.

Finch, R. J. and Ewing, R. C., 1992. The corrosion of uraninite under oxidizing conditions. *J. Nucl. Mater.* **190**, 133-156.

Finneran, K. T., Housewright, M. E., and Lovley, D. R., 2002. Multiple influences of nitrate on uranium solubility during bioremediation of uranium-contaminated subsurface sediments. *Environ. Microbiol.* **4**, 510-516.

Fletcher, K. E., Boyanov, M. I., Thomas, S. H., Wu, Q. Z., Kemner, K. M., and Loffler, F. E., 2010. U(VI) reduction to mononuclear U(IV) by desulfitobacterium species. *Environ. Sci. Technol.* **44**, 4705-4709.

Fox, P. M., Davis, J. A., Kukkadapu, R., Singer, D. M., Bargar, J., and Williams, K. H., 2013. Abiotic U(VI) reduction by sorbed Fe(II) on natural sediments. *Geochim. Cosmochim. Acta* **117**, 266-282.

Fredrickson, J. K., Zachara, J. M., Kennedy, D. W., Duff, M. C., Gorby, Y. A., Li, S. M. W., and Krupka, K. M., 2000. Reduction of U(VI) in goethite (alpha-FeOOH) suspensions by a dissimilatory metal-reducing bacterium. *Geochim. Cosmochim. Acta* **64**, 3085-3098.

Fredrickson, J. K., Zachara, J. M., Kennedy, D. W., Liu, C. X., Duff, M. C., Hunter, D. B., and Dohnalkova, A., 2002. Influence of Mn oxides on the reduction of uranium(VI) by the metal-reducing bacterium Shewanella putrefaciens. *Geochim. Cosmochim. Acta* **66**, 3247-3262.

Gallegos, T. J., Fuller, C. C., Webb, S. M., and Betterton, W., 2013. Uranium(VI) interactions with mackinawite in the presence and absence of bicarbonate and oxygen. *Environ. Sci. Technol.* **47**, 7357-7364.

Ganesh, R., Robinson, K. G., Reed, G. D., and Sayler, G. S., 1997. Reduction of hexavalent uranium from organic complexes by sulfate- and iron-reducing bacteria. *Appl. Environ. Microbiol.* **63**, 4385-91.

Gascoyne, M., 1992. Geochemistry of the actinides and their daughters. In: Ivanovich;, M. and Harmon, R. S. Eds.), *Uraniumseries Disequilibrium: ApplicationstoEarth, Marine, and Environmental Science*. Clarendon Press.

Gavrilescu, M., Pavel, L. V., and Cretescu, I., 2009. Characterization and remediation of soils contaminated with uranium. *J. Hazard. Mater.* **163**, 475-510.

Ginder-Vogel, M., Criddle, C. S., and Fendorf, S., 2006. Thermodynamic constraints on the oxidation of biogenic UO_2 by Fe(III) (hydr) oxides. *Environ. Sci. Technol.* **40**, 3544-3550.

Ginder-Vogel, M. and Fendorf, S., 2007. Chapter 11 Biogeochemical Uranium Redox Transformations: Potential Oxidants of Uraninite. In: Mark, O. B. and Douglas, B. K. Eds.), *Developments in Earth and Environmental Sciences*. Elsevier.

Ginder-Vogel, M., Stewart, B., and Fendorf, S., 2010. Kinetic and mechanistic constraints on the oxidation of biogenic uraninite by ferrihydrite. *Environ. Sci. Technol.* **44**, 163-169.

Goldhaber, M. B. and Kaplan, I. R., 1974. The sulfur cycle. In: Goldberg Jr., E. (Ed.), *The Sea*. Wiley & Sons, New York.

Grambow, B., 1989. Spent fuel dissolution and oxidation: an evaluation of literature data*SKB Technical Report*. Hanh-Meitner-Institut, Berlin.

Gu, B., Wu, W.-M., Ginder-Vogel, M. A., Yan, H., Fields, M. W., Zhou, J., Fendorf, S., Criddle, C. S., and Jardine, P. M., 2005. Bioreduction of uranium in a contaminated soil column. *Environ. Sci. Technol.* **39**, 4841-4847.

Guillaumont, R., Mompean, F. J., and OECD Nuclear Energy Agency., 2003. Update on the chemical thermodynamics of uranium, neptunium, plutonium, americium and technetium. Elsevier; Nuclear Energy Agency, Organisation for Economic Co-Operation and Development, Amsterdam; Boston; Paris.

Han, Y. S., Gallegos, T. J., Demond, A. H., and Hayes, K. F., 2011. FeS-coated sand for removal of arsenic(III) under anaerobic conditions in permeable reactive barriers. *Water Res.* **45**, 593-604.

Herbert, R. B., Benner, S. G., Pratt, A. R., and Blowes, D. W., 1998. Surface chemistry and morphology of poorly crystalline iron sulfides precipitated in media containing sulfate-reducing bacteria. *Chem. Geol.* **144**, 87-97.

Holmes, D. E., Finneran, K. T., O'Neil, R. A., and Lovley, D. R., 2002. Enrichment of members of the family geobacteraceae associated with stimulation of dissimilatory metal reduction in uranium-contaminated aquifer sediments. *Appl. Environ. Microbiol.* **68**, 2300-2306.

Hsi, C. D. and Langmuir, D., 1985. Adsorption of uranyl onto ferric oxyhydroxides: Application of the surface complexation site-binding model. *Geochim. Cosmochim. Acta* **49**, 1931-1941.

Hua, B. and Deng, B. L., 2008. Reductive immobilization of uranium(VI) by amorphous iron sulfide. *Environ. Sci. Technol.* **42**, 8703-8708.

Hua, B., Xu, H. F., Terry, J., and Deng, B. L., 2006. Kinetics of uranium(VI) reduction by hydrogen sulfide in anoxic aqueous systems. *Environ. Sci. Technol.* **40**, 4666-4671.

Hyun, S. P., Davis, J. A., Sun, K., and Hayes, K. F., 2012. Uranium(VI) reduction by iron(II) monosulfide mackinawite. *Environ. Sci. Technol.* **46**, 3369-3376.

Hyun, S. P., Fox, P. M., Davis, J. A., Campbell, K. M., Hayes, K. F., and Long, P. E., 2009. Surface Complexation Modeling of U(VI) Adsorption by Aquifer Sediments from a Former Mill Tailings Site at Rifle, Colorado. *Environ. Sci. Technol.* **43**, 9368-9373.

Hyun, S. P. and Hayes, K. F., 2009. Feasibility of Using In Situ FeS Precipitation for TCE Degradation. *Journal of Environmental Engineering-Asce* **135**, 1009-1014.

Issatchenko, B. L., 1912. Über die Ablagerung von schwefligem Eisen in den Bakterien. *Bulletin du Jardin Imperiale de Saint-Petersbourg*, 140-153.

Istok, J. D., Senko, J. M., Krumholz, L. R., Watson, D., Bogle, M. A., Peacock, A., Chang, Y. J., and White, D. C., 2004. In situ bioreduction of technetium and uranium in a nitrate-contaminated aquifer. *Environ. Sci. Technol.* **38**, 468-475.

Jeong, H. Y., Han, Y. S., Park, S. W., and Hayes, K. F., 2010a. Aerobic oxidation of mackinawite (FeS) and its environmental implication for arsenic mobilization. *Geochim. Cosmochim. Acta* **74**, 3182-3198.

Jeong, H. Y., Lee, J. H., and Hayes, K. F., 2008. Characterization of synthetic nanocrystalline mackinawite: Crystal structure, particle size, and specific surface area. *Geochim. Cosmochim. Acta* **72**, 493-505.

Jeong, H. Y., Sun, K., and Hayes, K. F., 2010b. Microscopic and spectroscopic characterization of Hg(II) immobilization by mackinawite (FeS). *Environ. Sci. Technol.* **44**, 7476-7483.

Kato, S., Nakamura, R., Kai, F., Watanabe, K., and Hashimoto, K., 2010. Respiratory interactions of soil bacteria with (semi)conductive iron-oxide minerals. *Environ. Microbiol.* **12**, 3114-3123.

Kelly, S. D., Kemner, K. M., Carley, J., Criddle, C., Jardine, P. M., Marsh, T. L., Phillips, D., Watson, D., and Wu, W. M., 2008. Speciation of uranium in sediments before and after in situ biostimulation. *Environ. Sci. Technol.* **42**, 1558-1564.

Komlos, J., Peacock, A., Kukkadapu, R. K., and Jaffe, P. R., 2008. Long-term dynamics of uranium reduction/reoxidation under low sulfate conditions. *Geochim. Cosmochim. Acta* **72**, 3603-3615.

Kukkadapu, R. K., Zachara, J. M., Fredrickson, J. K., McKinley, J. P., Kennedy, D. W., Smith, S. C., and Dong, H., 2006. Reductive biotransformation of Fe in shale–limestone saprolite containing Fe(III) oxides and Fe(II)/Fe(III) phyllosilicates. *Geochim. Cosmochim. Acta* **70**, 3662-3676.

Langmuir, D., 1978. Uranium solution-mineral equilibria at low-temperatures with applications to sedimentary ore-deposits. *Geochim. Cosmochim. Acta* **42**, 547-569.

Lennie, A. R., Redfern, S. A. T., Schofield, P. F., and Vaughan, D. J., 1995. Synthesis and Rietveld crystal structure refinement of mackinawite, tetragonal FeS. *Mineralogical Magazine* **59**, 677-683.

Lennie, A. R. and Vaughan, D. J., 1996. Spectroscopic studies of iron sulfide formation and phase relations at low temperatures. In: Dyar, M. D., McCammon, C., and Schaefer, M. W. Eds.)*Mineral Spectroscopy: A tribute to R. G. Burns*. The Geochemical Society, St. Louis, Mo.

Liger, E., Charlet, L., and Van Cappellen, P., 1999. Surface catalysis of uranium(VI) reduction by iron(II). *Geochim. Cosmochim. Acta* **63**, 2939-2955.

Lovley, D. R. and Phillips, E. J. P., 1992. Reduction Of Uranium By Desulfovibrio-Desulfuricans. *Appl. Environ. Microbiol.* **58**, 850-856.

Lovley, D. R., Phillips, E. J. P., Gorby, Y. A., and Landa, E. R., 1991. Microbial reduction of uranium. *Nature* **350**, 413-416.

Lovley, D. R., Roden, E. E., Phillips, E. J. P., and Woodward, J. C., 1993. Enzymatic iron and uranium reduction by sulfate-reducing bacteria. *Mar. Geol.* **113**, 41-53.

Majzlan, J., Grevel, K. D., and Navrotsky, A., 2003. Thermodynamics of Fe oxides: Part II. Enthalpies of formation and relative stability of goethite (alpha-FeOOH), lepidocrocite (gamma-FeOOH), and maghemite (gamma-Fe2O3). *Am. Mineral.* **88**, 855-859.

Majzlan, J., Navrotsky, A., and Schwertmann, U., 2004. Thermodynamics of iron oxides: Part III. Enthalpies of formation and stability of ferrihydrite (∼Fe(OH)3), schwertmannite (∼FeO(OH)3/4(SO4)1/8), and ε-Fe2O3. *Geochim. Cosmochim. Acta* **68**, 1049-1059.

McGuire, M. M. and Hamers, R. J., 2000. Extraction and quantitative analysis of elemental sulfur from sulfide mineral surfaces by high-performance liquid chromatography. *Environ. Sci. Technol.* **34**, 4651-4655.

Mikhlin, Y., 2007. Disordered surface layers of metal sulfides and their reactivity. *Glass Phys. Chem* **33**, 402-410.

Mikhlin, Y., Varnek, V., Asanov, I., Tomashevich, Y., Okotrub, A., Livshits, A., Selyutin, G., and Pashkov, G., 2000. Reactivity of pyrrhotite (Fe9S10) surfaces: Spectroscopic studies. *PCCP* **2**, 4393-4398.

Moon, H. S., Komlos, J., and Jaffe, P. R., 2007. Uranium reoxidation in previously bioreduced sediment by dissolved oxygen and nitrate. *Environ. Sci. Technol.* **41**, 4587-4592.

Moon, H. S., Komlos, J., and Jaffé, P. R., 2009. Biogenic U(IV) oxidation by dissolved oxygen and nitrate in sediment after prolonged U(VI)/Fe(III)/SO_4^{2-} reduction. *J. Contam. Hydrol.* **105**, 18-27.

Moon, H. S., McGuinness, L., Kukkadapu, R. K., Peacock, A. D., Komlos, J., Kerkhof, L. J., Long, P. E., and Jaffé, P. R., 2010. Microbial reduction of uranium under iron- and sulfate-reducing conditions: Effect of amended goethite on microbial community composition and dynamics. *Water Res.* **44**, 4015-4028.

Morel, F. o. and Hering, J. G., 1993. *Principles and applications of aquatic chemistry*. Wiley, New York.

Morgan, B. and Lahav, O., 2007. The effect of pH on the kinetics of spontaneous Fe(II) oxidation by O_2 in aqueous solution - basic principles and a simple heuristic description. *Chemosphere* **68**, 2080-2084.

Morice, J. A., Rees, L. V. C., and Rickard, D. T., 1969. Mossbauer studies of iron sulphides. *Journal of Inorganic & Nuclear Chemistry* **31**, 3797-&.

Moyes, L. N., Parkman, R. H., Charnock, J. M., Vaughan, D. J., Livens, F. R., Hughes, C. R., and Braithwaite, A., 2000. Uranium uptake from aqueous solution by interaction with goethite, lepidocrocite, muscovite, and mackinawite: An X-ray absorption spectroscopy study. *Environ. Sci. Technol.* **34**, 1062-1068.

Mullet, M., Boursiquot, S., Abdelmoula, M., Genin, J. M., and Ehrhardt, J. J., 2002. Surface chemistry and structural properties of mackinawite prepared by reaction of sulfide ions with metallic iron. *Geochim. Cosmochim. Acta* **66**, 829-836.

Murad, E. and Cashion, J., 2004. *Mössbauer spectroscopy of environmental materials and their industrial utilization*. Kluwer Academic Publishers, Dordrecht.

N'Guessan, A. L., Vrionis, H. A., Resch, C. T., Long, P. E., and Lovley, D. R., 2008. Sustained removal of uranium from contaminated groundwater following stimulation of dissimilatory metal reduction. *Environ. Sci. Technol.* **42**, 2999-3004.

National Research, C., 1999. *Groundwater & soil cleanup: improving management of persistent contaminants*. National Academy Press, Washington, D.C.

Newville, M., 2001. IFEFFIT: interactive XAFS analysis and FEFF fitting. *J. Synchrotron Radiat.* **8**, 322-324.

Nico, P. S., Stewart, B. D., and Fendorf, S., 2009. Incorporation of oxidized uranium into Fe (hydr)oxides during Fe(II) catalyzed remineralization. *Environ. Sci. Technol.* **43**, 7391-7396.

OEHHA, 2001. Public health goal for uranium in drinking water. In: Agency, C. E. P. (Ed.). Office of Environmental Health Hazard Assessment.

Ohfuji, H. and Rickard, D., 2006. High resolution transmission electron microscopic study of synthetic nanocrystalline mackinawite. *Earth. Planet. Sci. Lett.* **241**, 227-233.

Pedersen, H. D., Postma, D., Jakobsen, R., and Larsen, O., 2005. Fast transformation of iron oxyhydroxides by the catalytic action of aqueous Fe(II). *Geochim. Cosmochim. Acta* **69**, 3967-3977.

Peterson, R. E., Rockhold, M. L., Serne, R. J., Thorne, P. D., and Williams, M. D., 2008. Uranium Contamination in the Subsurface Beneath the 300 Area, Hanford Site, Washington. Pacific Northwest National Laboratory.

Phillips, E. J. P., Landa, E. R., and Lovley, D. R., 1995. Remediation of uranium contaminated soils with bicarbonate extraction and microbial U(VI) reduction. *Journal of Industrial Microbiology & Biotechnology* **14**, 203-207.

Pickering, I. J., George, G. N., Yu, E. Y., Brune, D. C., Tuschak, C., Overmann, J., Beatty, J. T., and Prince, R. C., 2001. Analysis of sulfur biochemistry of sulfur bacteria using X-ray absorption spectroscopy. *Biochemistry* **40**, 8138-8145.

Pierce, E. M., Icenhower, J. P., Serne, R. J., and Catalano, J. G., 2005. Experimental determination of UO2(cr) dissolution kinetics: Effects of solution saturation state and pH. *J. Nucl. Mater.* **345**, 206-218.

Prietzel, J. r., Botzaki, A., Tyufekchieva, N., Brettholle, M., Thieme, J. r., and Klysubun, W., 2011. Sulfur speciation in soil by S K-edge XANES spectroscopy: comparison of spectral deconvolution and linear combination fitting. *Environ. Sci. Technol.* **45**, 2878-2886.

Qafoku, N. P., Kukkadapu, R. K., McKinley, J. P., Arey, B. W., Kelly, S. D., Wang, C. M., Resch, C. T., and Long, P. E., 2009. Uranium in framboidal pyrite from anaturally bioreduced alluvial sediment. *Environ. Sci. Technol.* **43**, 8528-8534.

Rancourt, D. G. and Ping, J. Y., 1991. Voigt-based methods for arbitrary-shape static hyperfine parameter distributions in Mossbauer-spectroscopy. *Nuclear Instruments & Methods in Physics Research Section B-Beam Interactions with Materials and Atoms* **58**, 85-97.

Rehr, J. J., Albers, R. C., and Zabinsky, S. I., 1992. High-order multiple-scattering calculations of X-ray-absorption fine structure. *Phys. Rev. Lett.* **69**, 3397-3400.

Rickard, D., 1995. Kinetics of Fes precipitation: Part 1. Competing reaction mechanisms. *Geochim. Cosmochim. Acta* **59**, 4367-4379.

Rickard, D. and Morse, J. W., 2005. Acid volatile sulfide (AVS). *Mar. Chem.* **97**, 141-197.

Rickard, D. T., 1969a. *The chemistry of iron sulphide formation at low temperatures*. University of Stockholm.

Rickard, D. T., 1969b. *The microbiological formation of iron sulphides*. Stockholm contributions in geology, Stockholm.

Riley, R. G., Zachara, J. M., and Wobber, F. J., 1992. Chemical Contaminants on DOE Lands and Selection of Contaminant Mixtures for Subsurface Science Research. U.S. Department of Energy: Washington D.C.

Sani, R. K., Peyton, B. M., Dohnalkova, A., and Amonette, J. E., 2005. Reoxidation of reduced uranium with iron(III) (hydr)oxides under sulfate-reducing conditions. *Environ. Sci. Technol.* **39**, 2059-2066.

Santos, B. G., Noël, J. J., and Shoesmith, D. W., 2006. The influence of calcium ions on the development of acidity in corrosion product deposits on SIMFUEL, UO2. *J. Nucl. Mater.* **350**, 320-331.

Schippers, A. and Jorgensen, B. B., 2002. Biogeochemistry of pyrite and iron sulfide oxidation in marine sediments. *Geochim. Cosmochim. Acta* **66**, 85-92.

Schippers, A. and Sand, W., 1999. Bacterial leaching of metal sulfides proceeds by two indirect mechanisms via thiosulfate or via polysulfides and sulfur. *Appl. Environ. Microbiol.* **65**, 319-321.

Schofield, E. J., Veeramani, H., Sharp, J. O., Suvorova, E., Bernier-Latmani, R., Mehta, A., Stahlman, J., Webb, S. M., Clark, D. L., Conradson, S. D., Ilton, E. S., and Bargar, J. R., 2008. Structure of Biogenic Uraninite Produced by Shewanella oneidensis Strain MR-1. *Environ. Sci. Technol.* **42**, 7898-7904.

Schwertmann, U. and Cornell, R. M., 2000. Iron oxides in the laboratory: preparation and characterization. Wiley-VCH, Weinheim ; New York.

Senko, J. M., Istok, J. D., Suflita, J. M., and Krumholz, L. R., 2002. In-situ evidence for uranium immobilization and remobilization. *Environ. Sci. Technol.* **36**, 1491-1496.

Senko, J. M., Mohamed, Y., Dewers, T. A., and Krumholz, L. R., 2005a. Role for Fe(III) minerals in nitrate-dependent microbial U(IV) oxidation. *Environ. Sci. Technol.* **39**, 2529-2536.

Senko, J. M., Suflita, J. M., and Krumholz, L. R., 2005b. Geochemical controls on microbial nitrate-dependent U(IV) oxidation. *Geomicrobiol. J.* **22**, 371-378.

Sharp, J. O., Lezama-Pacheco, J. S., Schofield, E. J., Junier, P., Ulrich, K.-U., Chinni, S., Veeramani, H., Margot-Roquier, C., Webb, S. M., Tebo, B. M., Giammar, D. E., Bargar, J. R., and Bernier-Latmani, R., 2011. Uranium speciation and stability after reductive immobilization in aquifer sediments. *Geochim. Cosmochim. Acta* **75**, 6497-6510.

Sherman, D. M., Peacock, C. L., and Hubbard, C. G., 2008. Surface complexation of U(VI) on goethite (alpha-FeOOH). *Geochim. Cosmochim. Acta* **72**, 298-310.

Shoesmith, D. W., 2000. Fuel corrosion processes under waste disposal conditions. *J. Nucl. Mater.* **282**, 1-31.

Singer, D. M., Farges, F., and Brown, G. E., 2009. Biogenic nanoparticulate UO_2: Synthesis, characterization, and factors affecting surface reactivity. *Geochim. Cosmochim. Acta* **73**, 3593-3611.

Spadini, L., Bott, M., Wehrli, B., and Manceau, A., 2003. Analysis of the Major Fe Bearing Mineral Phases in Recent Lake Sediments by EXAFS Spectroscopy. *Aquatic Geochemistry* **9**, 1-17.

Spycher, N. F., Issarangkun, M., Stewart, B. D., Sengor, S. S., Belding, E., Ginn, T. R., Peyton, B. M., and Sani, R. K., 2011a. Biogenic uraninite precipitation and its reoxidation by iron(III) (hydr)oxides: A reaction modeling approach. *Geochimica Et Cosmochimica Acta* **75**, 4426-4440.

Spycher, N. F., Issarangkun, M., Stewart, B. D., Sevinç Şengör, S., Belding, E., Ginn, T. R., Peyton, B. M., and Sani, R. K., 2011b. Biogenic uraninite precipitation and its reoxidation by iron(III) (hydr)oxides: A reaction modeling approach. *Geochim. Cosmochim. Acta* **75**, 4426-4440.

Stewart, B. D., Mayes, M. A., and Fendorf, S., 2010. Impact of uranyl-calcium-carbonato complexes on uranium(VI) adsorption to synthetic and natural sediments. *Environ. Sci. Technol.* **44**, 928-934.

Stewart, B. D., Nico, P. S., and Fendorf, S., 2009. Stability of uranium incorporated into Fe (hydr)oxides under fluctuating redox conditions. *Environ. Sci. Technol.* **43**, 4922-4927.

Stookey, L. L., 1970. Ferrozine - a new spectrophotometric reagent for iron. *Anal. Chem.* **42**, 779-781.

Stumm, W., 1987. *Aquatic surface chemistry: chemical processes at the particle-water interface*. Wiley, New York.

Suzuki, Y., Kelly, S. D., Kemner, K. M., and Banfield, J. F., 2002. Radionuclide contamination - Nanometre-size products of uranium bioreduction. *Nature* **419**, 134-134.

Suzuki, Y., Kelly, S. D., Kemner, K. M., and Banfield, J. F., 2005. Direct microbial reduction and subsequent preservation of uranium in natural near-surface sediment. *Appl. Environ. Microbiol.* **71**, 1790-1797.

Torrero, M. E., Baraj, E., DePablo, J., Gimenez, J., and Casas, I., 1997. Kinetics of corrosion and dissolution of uranium dioxide as a function of pH. *Int. J. Chem. Kinet.* **29**, 261-267.

Ulrich, K. U., Ilton, E. S., Veeramani, H., Sharp, J. O., Bernier-Latmani, R., Schofield, E. J., Bargar, J. R., and Giammar, D. E., 2009. Comparative dissolution kinetics of biogenic and chemogenic uraninite under oxidizing conditions in the presence of carbonate. *Geochim. Cosmochim. Acta* **73**, 6065-6083.

Ulrich, K. U., Rossberg, A., Foerstendorf, H., Zanker, H., and Scheinost, A. C., 2006. Molecular characterization of uranium(VI) sorption complexes on iron(III)-rich acid mine water colloids. *Geochim. Cosmochim. Acta* **70**, 5469-5487.

Ulrich, K. U., Singh, A., Schofield, E. J., Bargar, J. R., Veeramani, H., Sharp, J. O., Bernier-Latmani, R., and Giammar, D. E., 2008. Dissolution of biogenic and synthetic UO_2 under varied reducing conditions. *Environ. Sci. Technol.* **42**, 5600-5606.

Vaughan, D. J. and Ridout, M. S., 1971. Mossbauer studies of some sulphide minerals. *Journal of Inorganic & Nuclear Chemistry* **33**, 741-&.

Veeramani, H., Alessi, D. S., Suvorova, E. I., Lezama-Pacheco, J. S., Stubbs, J. E., Sharp, J. O., Dippon, U., Kappler, A., Bargar, J. R., and Bernier-Latmani, R., 2011. Products of abiotic U(VI) reduction by biogenic magnetite and vivianite. *Geochim. Cosmochim. Acta* **75**, 2512-2528.

Veeramani, H., Schofield, E. J., Sharp, J. O., Suvorova, E. I., Ulrich, K.-U., Mehta, A., Giammar, D. E., Bargar, J. R., and Bernier-Latmani, R., 2009. Effect of Mn(II) on the structure and reactivity of biogenic uraninite. *Environ. Sci. Technol.* **43**, 6541-6547.

Viollier, E., Inglett, P. W., Hunter, K., Roychoudhury, A. N., and Van Cappellen, P., 2000. The ferrozine method revisited: Fe(II)/Fe(III) determination in natural waters. *Appl. Geochem.* **15**, 785-790.

Wan, J. M., Tokunaga, T. K., Brodie, E., Wang, Z. M., Zheng, Z. P., Herman, D., Hazen, T. C., Firestone, M. K., and Sutton, S. R., 2005. Reoxidation of bioreduced uranium under reducing conditions. *Environ. Sci. Technol.* **39**, 6162-6169.

Wang, Z., Lee, S.-W., Kapoor, P., Tebo, B. M., and Giammar, D. E., 2013. Uraninite oxidation and dissolution induced by manganese oxide: A redox reaction between two insoluble minerals. *Geochim. Cosmochim. Acta* **100**, 24-40.

Wazne, M., Korfiatis, G. P., and Meng, X. G., 2003. Carbonate effects on hexavalent uranium adsorption by iron oxyhydroxide. *Environ. Sci. Technol.* **37**, 3619-3624.

Webb, S. M., 2005. SIXpack: a graphical user interface for XAS analysis using IFEFFIT. *Phys. Scr.* **T115**, 1011-1014.

Wersin, P., Hochella, M. F., Persson, P., Redden, G., Leckie, J. O., and Harris, D. W., 1994. Interaction between aqueous uranium(VI) and sulfide minerals - spectroscopic evidence for sorption and reduction. *Geochim. Cosmochim. Acta* **58**, 2829-2843.

WHO, 1998. Guidelines for drinking-water quality. Addendum to volume 1. Recommendations. World Health Organisation, Geneva, Switzerland.

Widler, A. and Seward, T., 2002. The adsorption of gold (I) hydrosulphide complexes by iron sulphide surfaces. *Geochim. Cosmochim. Acta* **66**, 383-402.

Wilkin, R. T. and Barnes, H. L., 1996. Pyrite formation by reactions of iron monosulfides with dissolved inorganic and organic sulfur species. *Geochim. Cosmochim. Acta* **60**, 4167-4179.

Williams, A. G. B. and Scherer, M. M., 2004. Spectroscopic evidence for Fe(II)-Fe(III) electron transfer at the iron oxide-water interface. *Environ. Sci. Technol.* **38**, 4782-4790.

Wilmot, P. D., Cadee, K., Katinic, J. J., and Kavanagh, B. V., 1988. Kinetics of sulfide oxidation by dissolved oxygen. *J. - Water Pollut. Control Fed.* **60**, 1264-1270.

Wolthers, M., Charlet, L., Van der Linde, P. R., Rickard, D., and Van der Weijden, C. H., 2005. Surface chemistry of disordered mackinawite (FeS). *Geochim. Cosmochim. Acta* **69**, 3469-3481.

Wolthers, M., Van der Gaast, S. J., and Rickard, D., 2003. The structure of disordered mackinawite. *Am. Mineral.* **88**, 2007-2015.

Wu, W.-M., Carley, J., Fienen, M., Mehlhorn, T., Lowe, K., Nyman, J., Luo, J., Gentile, M. E., Rajan, R., Wagner, D., Hickey, R. F., Gu, B., Watson, D., Cirpka, O. A., Kitanidis, P. K., Jardine, P. M., and Criddle, C. S., 2006a. Pilot-Scale in Situ Bioremediation of Uranium in a Highly Contaminated Aquifer. 1. Conditioning of a Treatment Zone. *Environ. Sci. Technol.* **40**, 3978-3985.

Wu, W.-M., Carley, J., Gentry, T., Ginder-Vogel, M. A., Fienen, M., Mehlhorn, T., Yan, H., Caroll, S., Pace, M. N., Nyman, J., Luo, J., Gentile, M. E., Fields, M. W., Hickey, R. F., Gu, B., Watson, D., Cirpka, O. A., Zhou, J., Fendorf, S., Kitanidis, P. K., Jardine, P. M., and Criddle, C. S., 2006b. Pilot-scale in situ bioremedation of uranium in a highly contaminated aquifer. 2. reduction of U(VI) and geochemical control of U(VI) bioavailability. *Environ. Sci. Technol.* **40**, 3986-3995.

Wu, W. M., Carley, J., Luo, J., Ginder-Vogel, M. A., Cardenas, E., Leigh, M. B., Hwang, C. C., Kelly, S. D., Ruan, C. M., Wu, L. Y., Van Nostrand, J., Gentry, T., Lowe, K., Mehlhorn, T., Carroll, S., Luo, W. S., Fields, M. W., Gu, B. H., Watson, D., Kemner, K. M., Marsh, T., Tiedje, J., Zhou, J. Z., Fendorf, S., Kitanidis, P. K., Jardine, P. M., and Criddle, C. S., 2007. In situ bioreduction of uranium (VI) to submicromolar levels and reoxidation by dissolved oxygen. *Environ. Sci. Technol.* **41**, 5716-5723.

Yee, N., Shaw, S., Benning, L. G., and Nguyen, T. H., 2006. The rate of ferrihydrite transformation to goethite via the Fe(II) pathway. *Am. Mineral.* **91**, 92-96.

Zhou, P. and Gu, B. H., 2005. Extraction of oxidized and reduced forms of uranium from contaminated soils: Effects of carbonate concentration and pH. *Environ. Sci. Technol.* **39**, 4435-4440.